Fizika Nizkikh Temperatur, 2008, v. 34, No. 2, p. 107–147

X-ray magnetic circular dichroism in *d* and *f* ferromagnetic materials: recent theoretical progress. Part II

(Review Article)

V.N. Antonov and A.P. Shpak

Institute of Metal Physics, 36 Vernadskii Str., 03142 Kiev, Ukraine
E-mail: antonov@imp.kiev.ua

A.N. Yaresko

Max-Planck-Institut for the Physics of Complex Systems, D-01187 Dresden, Germany

Received April 10, 2007

The current status of theoretical understanding of the x-ray magnetic circular dichroism (XMCD) of $4f$ and $5f$ compounds is reviewed. Energy band theory based upon the local spin-density approximation (LSDA) describes the XMCD spectra of transition metal compounds with high accuracy. However, the LSDA does not suffice for lanthanide compounds which have a correlated $4f$ shell. A satisfactory description of the XMCD spectra could be obtained by using a generalization of the LSDA, in which explicitly f electron Coulomb correlation are taken into account (LSDA + U approach). As examples of this group we consider GdN compound. We also consider uranium $5f$ compounds. In those compounds where the $5f$ electrons are rather delocalized, the LSDA describes the XMCD spectra reasonably well. As example of this group we consider UFe_2. Particular differences occur for the uranium compounds where the $5f$ electrons are neither delocalized nor localized, but more or less semilocalized. Typical examples are UXAl (X = Co, Rh, and Pt), and UX (X = S, Se, Te). The semilocalized $5f$'s are, however, not inert, but their interaction with conduction electrons plays an important role. We also consider the electronic structure and XMCD spectra of heavy-fermion compounds UPt_3, URu_2Si_2, UPd_2Al_3, UNi_2Al_3, and UBe_{13} where the degree of the $5f$ localization is increased in comparison with other uranium compounds. The electronic structure and XMCD spectra of UGe_2 which possesses simultaneously ferromagnetism and superconductivity also presented. Recently achieved improvements for describing $5f$ compounds are discussed.

PACS: 75.50.Cc Other ferromagnetic metals and alloys;
71.20.Lp Intermetallic compounds;
71.15.Rf Relativistic effects.

Keywords: electronic structure, density of electronic states, x-ray absorption spectra, x-ray magnetic circular dichroism, spin-orbit coupling, orbital magnetic moments.

Contents

1. Rare-earth compounds

The astonishing variety of magnetic behaviors in rare-earth-3d transition metal (R-TM) intermetallics reflects the complexity of the exchange mechanism involving direct and indirect interaction mediated by the band states. These mechanisms are still not completely understood. X-ray magnetic circular dichroism (XMCD), being element and orbital selective, offers the opportunity to probe the TM 4p and 3d band states by scanning through their K and $L_{2,3}$ edges, respectively. Information on the rare-earth ground state is usually obtained by performing XMCD measurements at the rare-earth $M_{4,5}$ edges since these edges involve the $3d \rightarrow 4f$ transitions, i.e., they probe the electronic states of the $4f$ shell. On the other hand, $L_{2,3}$ edges of rare-earth ion provide the information on the R 5d band states through the $2p \rightarrow 5d$ transitions. Such studies of XCMD have shown to be very useful and give new insite on both the magnetic properties of the R-TM compounds and the interpretation of the XMCD spectra.

Recently systematic studies have been performed on several series of R-TM intermetallic crystals, amorphous materials and insulating ferromagnetic oxides in order to extract the relevant physical effects which govern the XCMD of K, $L_{2,3}$ and $M_{4,5}$ edges. Giorgetti et al. [1] present the XMCD studies at the $L_{2,3}$ edges of Ce and K edge of transition metals in $CeFe_2$, $Ce(Fe_{0.8}Co_{0.2})_2$, $CeCo_5$, Ce_2Co_{17}, $CeRu_2Ge_2$, Ce_3Al_{11}, CePd, $CoFe_2H_{3.8}$ compounds. Suga and Imada [2] studied a dense Kondo material, Sm_4As_3. They performed the $M_{4,5}$ and $N_{4,5}$ XMCD at the Sm edges. The authors also measure XMCD spectra in the permanent magnet $Nd_2Fe_{14}B$ at the $M_{4,5}$ and $L_{2,3}$ edges of Nd and Fe, respectively. The shape of the spectra agree with atomic calculations.

XMCD at Er $M_{4,5}$ [3] was used to follow the H,T magnetic phase diagram of an amorphous $Er_{12}Fe_{73}$ alloy. In these samples, macroscopic measurements of the magnetic moment show a strong evolution of the compensation temperature with the applied magnetic field. The variation of XMCD at Er $M_{4,5}$ is consistent with a magnetic structure of both the Er and Fe atoms. It shows the existence of temperature-induced, as well as field-induced, flip of the Er sublattice with respect to the direction of the magnetic field, evidenced by the change of sign of the dichroism. The authors of Ref. 4 present a XMCD study of a CeCuSi compound and a Ce/Fe multilayer performed at the Ce $M_{4,5}$ absorption edge. In the Ce/Fe multilayered structure (MLS), Ce atoms are in the highly hybridized α phase, characterized by a strong mixing between the $4f$ electrons with the valence band, and carry an ordered moment. XMCD experiments show the part of this moment is due to $4f$ electrons. The difference in the shape of the XMCD signals of a typical γ-like compound CeCuSi and of the Ce/Fe multilayer demonstrate that the XMCD spectra reflect the hybridization in the ground state of the cerium atoms in the multilayer. Ce $M_{4,5}$ XMCD spectra in strongly correlated ferromagnetic systems CeCuSi, $CeRh_3B_2$, and $CeFe_2$ measured in Ref. 5. By applying sum rules, it was shown that these experiments are able to yield both the magnitude and the direction of the $4f$ magnetic moments on Ce.

A systematic XMCD study at the Fe K edge on $RFe_{14}B$ series (R = rare earth and Y) performed in Ref. 6. The study identifies the influence of the rare-earth magnetic state into the K edge XMCD signals in $RFe_{14}B$ intermetallic compounds. This signal results from the addition of two components, each one being due to the magnetic contribution of both the iron and the rare-earth sublattices. The contribution of the R sublattice to the XMCD signal has been extracted yielding a direct correlation to the R magnetic moment. XMCD spectra has been measured in R–Co compounds (R = La, Tb, and Dy) at the Co K edge [7]. The experimental results have been interpreted within the multiple-scattering framework including the spin-orbit coupling. In the three systems, the XMCD spectra in the near edge region are well reproduced. Co K edge XMCD spectra in crystalline and amorphous Gd–Co alloys measured in Ref. 8. The results analyses using a semirelativistic full multiple scattering approach. It was shown that the spin polarization on Co atoms in $GdCo_5$ alloys is smaller than that in Co metal.

XMCD experiments have been performed in Ref. 9 at the R $L_{2,3}$ (R = rare earth) and Ni K edges on single crystals of $GdNi_5$ and $TbNi_5$. The spectra present huge and well-structured dichroic signals at both the R $L_{2,3}$ and N K edges. In $TbNi_5$ the negative XMCD structure, observed 3 eV below the edge at the Tb L_3 edge, was interpreted as the quadrupolar ($2p \rightarrow 4f$) transitions. A systematic study of XMCD, x-ray resonance magnetic scattering (XRMS), and resonance inelastic x-ray scattering (RIXS) at the $L_{2,3}$ edges of Nd on $Nd_2Fe_{14}B$ presented in Ref. 10 allowes to assign a dipole (E1) or quadrupole (E2) origin to different features appearing in the experimental spectra and to study the thermal dependence of the Nd moment orientation below the spin reorientation transition which take place at T_{SRT} = 135 K. A single crystal of Tb as a prototype system for a one-element magnet was used to investigate XMCD at the $L_{2,3}$ edge [11]. The high resolution of the experimental data allows for a clear identification of the E1 and E2 transitions. On the basis of *ab initio* calculations a simple procedure for extracting of the E2 part from the experimental XMCD data was developed.

Fe $L_{2,3}$ XMCD spectra on a single crystal of $Fe_{17}Dy_2$ measured by Castro et al. in Ref. 12. XMCD study at the K edge in the R_6Fe_{23} series (R = Ho and Y) presented in Ref. 13. This study identifies the influence of the rare-earth magnetic state on the K edge XMCD signals. The results demonstrate that the contribution of both Fe and R to the K edge XMCD spectra can be easily isolated

following its temperature-dependent behavior through compensation temperature and that they can be directly correlated to the Fe and R magnetic moments.

The distinguishing feature of the rare-earth elements in solids is the atomic character of the $4f$ levels, which lie relatively deep in the ion while having very small binding energies. It is this feature that account for the chemical similarity and magnetic diversity found in the series. A well-known consequence of this localized behavior is that a number of solid-state and spectroscopies involving the $4f$ electrons can be explained with the multiplet structure found from atomic calculations, with only small corrections being necessary to incorporate solid-state effects.

A $3d$ absorption process in rare-earth ions involves the electronic excitations to the $4f$ or the valence band (VB) levels [14], i.e.,

$$3d^{10}4f^{n}(\mathrm{VB})^{x} \rightarrow 3d^{9}4f^{n+1}(\mathrm{VB})^{x} \qquad (1)$$

or

$$3d^{10}4f^{n}(\mathrm{VB})^{x} \rightarrow 3d^{9}4f^{n}(\mathrm{VB})^{x+1}. \qquad (2)$$

The final-state configuration contains two open shells and due to strong $3d$–$4f$ overlap gives rise to large Coulomb and exchange correlation energies and produces a wide spread over the multiplet levels. The $3d \rightarrow$ VB excitations (2) have much weaker strength in comparison with the first ones (1) not only due to low $3d \rightarrow 6p$ cross section but also because near threshold the empty valence band states have mostly $5d$ character with a little hybridized $6p$ states. The total $3d^{9}4f^{n+1}$ multiplet structure is very complex and the total numbers of levels runs into thousands for many elements in the middle of the rare-earth series. There have been several calculations of the $3d(4d)^{9}4f^{n+1}$ multiplet structure in individual elements [15–26].

The theoretical analysis of magnetic circular dichroism of $4f$ photoemission spectra in Gd and Tb ions reported in Refs. 24–26. Imada and Jo calculate the $M_{4,5}$ and $N_{4,5}$ x-ray absorption spectra (XAS) [23] for left and right circularly polarized light in trivalent rare-earth ions. Thole et al. [20] measured and calculated in intermediate coupling the $M_{4,5}$ XAS for all the rare-earth metals.

The energy band approximation was used in Ref. 27 to calculated XMCD spectra of $Gd_5(Si_2Ge_2)$ compound. To treat the correlation effects at a simple level the LSDA + U method was used.

1.1. GdN

The Gd pnictides form an interesting family of materials, because of the great variety of their magnetic and electrical properties, despite their common simple crystal structure, the face-centered cubic of sodium chloride. While most Gd pnictides have been found to be antiferromagnetic, stoichiometric GdN after a controversial discussion over three decades [28,29] seems to be recognized now as a ferromagnet. It has a Curie temperature T_C around 60 K and a magnetic saturation moment near 7 μ_B/Gd ion consistent with the $^{8}S_{7/2}$ half filled $4f$ shell configuration of Gd^{3+} with zero orbital angular momentum [30].

An appealing property of GdN is that it is ferromagnetic with a large gap at the Fermi energy in the minority spin states, according to the electronic structure calculations based on the local density approximation [31–33]. At the same time, GdN is semimetallic in majority spin states with electron and hole pockets at the Fermi surface [32]. This latter property has led to some interest in GdN as a possible candidate for spin-dependent transport devices [34], exploiting the spin filter, giant magnetoresistance, or tunneling magnetoresistance effects.

X-ray absorption spectra and XMCD at the gadolinium $M_{4,5}$ and N K edges have been measured in GdN by Leuenberger at al. [35]. The ordered $4f$ moment extracted from the $M_{4,5}$ XMCD spectra was consistent with the $^{8}S_{7/2}$ configuration of Gd^{3+}. The exchange field generated by the Gd $4f$ electrons in the ferromagnetic phase of GdN induces a magnetic polarization of the N p band states, as can be concluded from the observation of strong magnetic circular dichroism at the K edge of nitrogen. However, a comparison of the spectra with the theoretical partial density of vacant N p states shows considerable disparities that are not well understood.

Figure 1 shows the fully relativistic spin-polarized energy band structure of GdN. In these calculations the $4f$ states have been considered as: (1) itinerant using the local spin-density approximation, (2) fully localized, treating them as core states, and (3) partly localized using the LSDA + U approximation.

The energy band structure of GdN with the $4f$ electrons in core can be subdivided into three regions separated by energy gaps. The bands in the lowest region around –12.9 to –11.1 eV have mostly N s character with some amount of Gd sp character mixed in. The next six energy bands are primarily N p bands separated from the s bands by an energy gap of about 6.2 eV. The width of the N p band is about 4.5 eV and is influenced by hybridization with Gd $5d$ states. The spin splitting of the N p bands is small (about 0.2 eV at the X symmetry point (Fig. 1)). The highest region can be characterized as Gd crystal field and spin-split d bands.

An important issue is the energy position of the occupied $4f$ states in the electron band structure of GdN. The LSDA calculations place the empty $4f$ states of Gd in GdN at 1 to 2 eV above the Fermi level with the occupied majority-spin $4f$ states situated at around –4 to –3.2 eV below Fermi level, E_F. It is well known that LSDA usually gives a wrong energy position for the $4f$ states in rare-earth compounds. For nonzero $4f$ occupation it

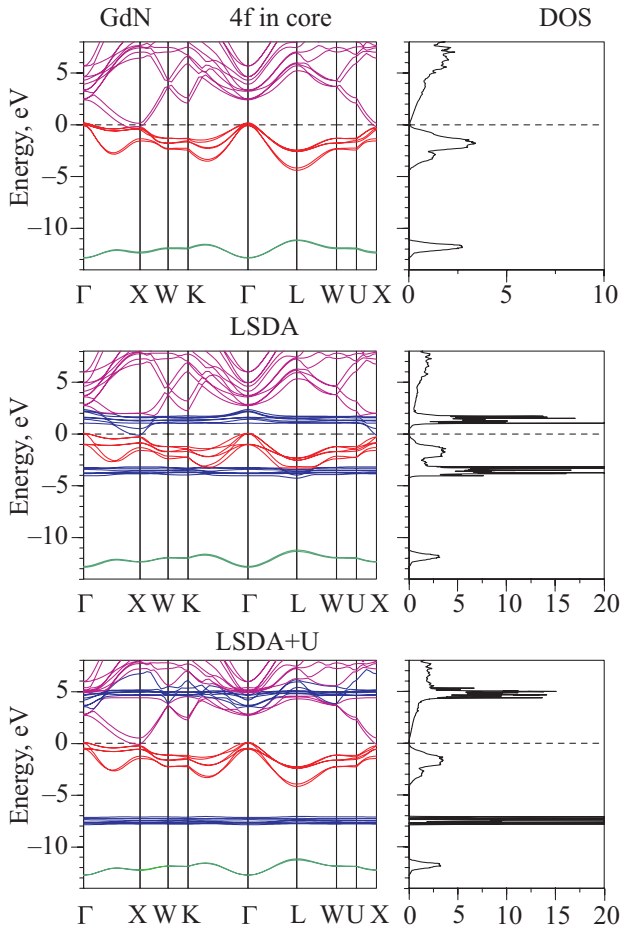

Fig. 1. Self-consistent fully relativistic spin-polarized energy band structure and total DOS (in states/(unit cell·eV)) calculated for GdN treating the 4*f* states as: (1) fully localized (4*f* in core); (2) itinerant (LSDA); and (3) partly localized (LSDA + *U*) [36].

places the 4*f* states right at the Fermi level [37,38] in contradiction with various experimental observations. In the case of Gd compounds the LSDA places the empty 4*f* states too close to the Fermi energy. For example, the LSDA calculations produce the empty 4*f* states in pure Gd metal at 2.7 eV above the Fermi level [39], although according to the x-ray bremsstrahlung isochromat spectroscopy (BIS) measurements they are situated around 5.5 eV above the Fermi level [40,41]. The XPS spectrum measured by Leuenberger et al. [35] in the valence band region of GdN shows the Gd^{3+} $4f^6$ final state multiplet located at around 8 eV below the Fermi level.

Figure 1 also presents the energy band structure of GdN calculated in the LSDA + *U* approximation. In such an approximation the Gd 4*f* empty states are situated around 5 eV above the Fermi level, well hybridized with Gd 5*d* and N 2*p* minority states. The majority-spin 4*f* states form a narrow band well below the Fermi energy and occupy a –7 to –8 eV energy interval in good agreement with the XPS measurements [35].

The partial density of states (DOS) of cubic ferromagnetic GdN are presented in Fig. 2 for the LSDA + *U* calculations. The majority 4*f* electrons create an exchange field that leads to spin splitting of the N *p* band. Furthermore, there is a visible Gd *d*–N *sp* as well as Gd 4*f*–N *p* hybridization in occupied part of GdN valence band. One of the consequences is that the N anion should carry a magnetic moment. The Gd *f* states above the Fermi level hybridize with the Gd $d_{t_{2g}}$ states only in the minority channel (Fig. 2). The Gd d_{e_g} states shift to higher energy due to the crystal-filed splitting and almost don't hybridize with the Gd 4*f* states. The orbital moments are equal to 0.057 μ_B and –0.0007μ_B on the Gd and N sites, respectively. Exchange and hybridization induce spin splitting of the conduction band states. As a result, the itinerant Gd 5*d* and N 2*p* derived band electrons carry small spin magnetic moments of 0.107 μ_B and –0.098 μ_B, respectively, that are of opposite each other and nearly cancel. The Gd 5*d* and N 2*p* orbital moments are equal to –0.0066 μ_B and –0.0007 μ_B, respectively.

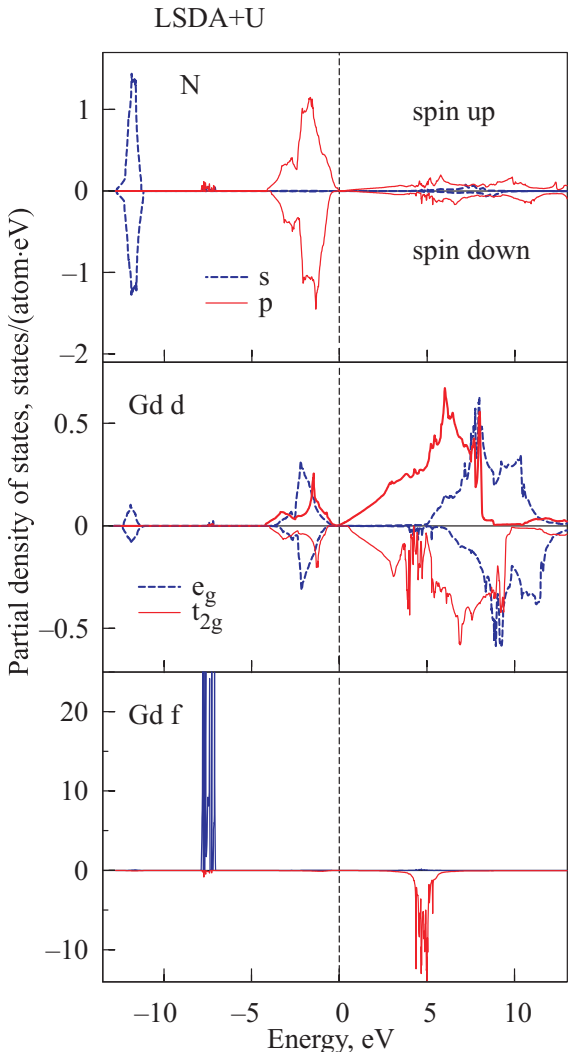

Fig. 2. Partial density of states of GdN [36]. The Fermi energy is at zero.

One should mention that although Gd^{3+} free ion consistent with the $^8S_{7/2}$ half filled $4f$ shell configuration possesses a zero orbital angular momentum, in solids Gd has small but nonzero orbital moment of around 0.063 μ_B due to hybridization with other states and also because in solids spin-up states are the linear combination of the $4f_{5/2}$ and $4f_{7/2}$ states and m_l for each state can be noninteger.

The study of the $4f$ electron shell in rare-earth compounds is usually performed by tuning the energy of the x-ray close to the $M_{4,5}$ edges of rare-earth where electronic transitions between $3d_{3/2,5/2}$ and $4f_{5/2,7/2}$ states are involved. Figure 3 shows the calculated XAS and XMCD spectra in the LSDA + U approximation for GdN at the $M_{4,5}$ edges together with the corresponding experimental data [35]. The experimentally measured dichroism is large, as is common for Gd-based systems at the $3d$ threshold; it amounts to more than 20 %.

The theoretically calculated XAS spectra have a rather simple line shape composed of two white line peaks at the M_5 and M_4 edges, however the experimentally measured spectra have well pronounced fine structures at high-energy part of the M_5 and M_4 XAS's. This fine structure are believed to be due to the multiplet structures which have not been included in the band structure calculations.

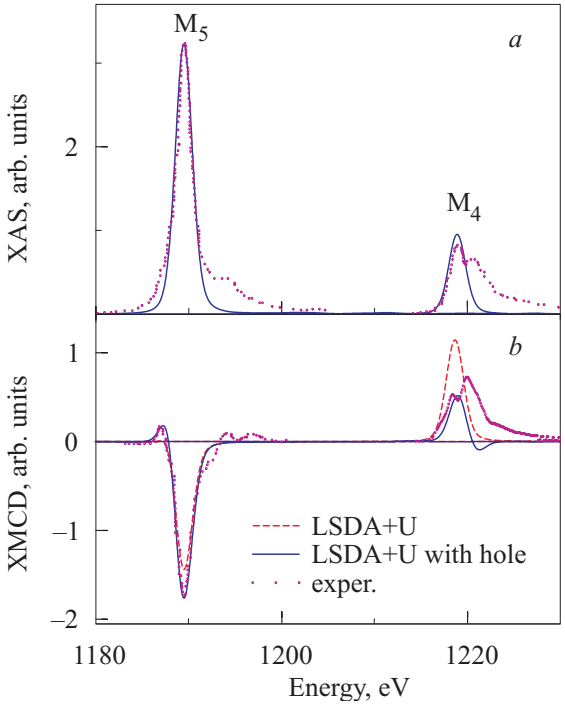

Fig. 3. (*a*) Theoretically calculated [36] (dotted lines) and experimental [35] (circles) isotropic absorption spectra of GdN at the Gd $M_{4,5}$ edges. Experimental spectra were measured with external magnetic field (0.1 T) at 15 K. (*b*) Experimental [35] (circles) XMCD spectra of GdN at the Gd $M_{4,5}$ edges in comparison with theoretically calculated ones using the LSDA + U approximation without (dotted lines) and with (full lines) taking into account core-hole effect.

Figure 3,*b* shows the calculated XMCD spectra in the LSDA + U approximation for GdN together with the corresponding experimental data [35]. The dichroism is mostly negative at the Gd M_5 edge and positive at the M_4 one. The calculations describe correctly the deep negative minimum at the Gd M_5 edge and the low-energy positive peak at the M_4 edge, however they don't produce the high-energy fine structures at both the edges, which are probably caused by the multiplet structure as described above. The XMCD at the M_5 edge also possesses an additional small positive lobe at the low-energy side which is not in the theoretical calculations. The LSDA + U theory underestimates the intensity for the XMCD spectrum at M_5 edge and overestimates it at the M_4 edge in comparison with the experiment.

We investigate also the effect of the core-hole effect in the final state using the supercell approximation. When the $3d$ core electron is photoexcited to the unoccupied $4f$ states, the distribution of the charge changes to account for the created hole. The final-state interaction improves the agreement between theory and the experiment at the M_5 edge in the intensity of the prominent negative peak and by producing correctly a positive lobe at the low-energy side.

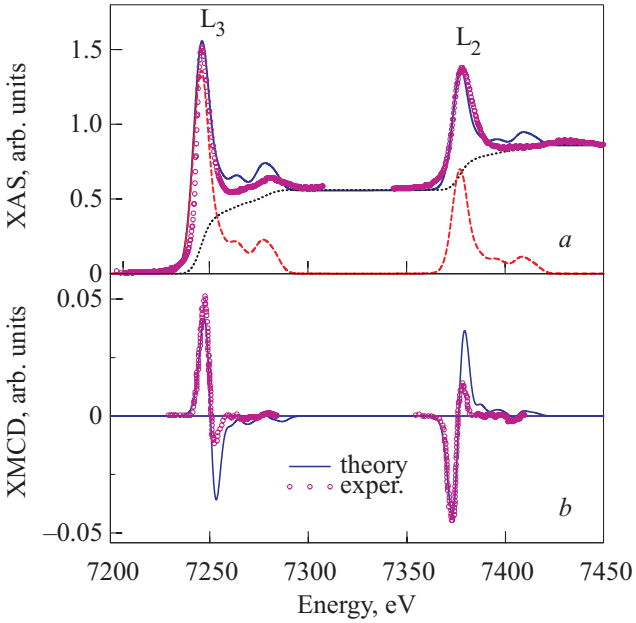

Fig. 4. (*a*) Theoretically calculated [36] (dashed line) and experimental [42] (circles) isotropic absorption spectra of GdN at the Gd $L_{2,3}$ edges (L_2 spectra are shifted towards smaller energy by 550 eV). Experimental spectra were measured at a bulklike GdN layer deposited on a Si substrate at 450 °C in total fluorescence yield mode. Dotted lines show the theoretically calculated background spectra, full thick lines are sum of the theoretical XAS and background spectra. (*b*) Experimental [42] (circles) XMCD spectra of GdN at the Gd $L_{2,3}$ edges in comparison with theoretically calculated ones using the LSDA + U (full lines) approximation.

Figure 4 shows the calculated XAS and XMCD spectra in the LSDA + U approximation at the $L_{2,3}$ edges together with the corresponding experimental data measured at bulklike layers of GdN [42].

Our calculations of Gd $L_{2,3}$ XAS produce two additional peaks at the high-energy side of the prominent peak, the position of the second high-energy peak is in good agreement with the experiment, however the first one is less pronounced in the experimental spectra.

The dichroism at the $L_{2,3}$ edges has two lobes, a positive and a negative one. The positive lobe is larger in comparison with the negative one for L_3 spectrum and *vice versa* for the L_2 edge. Our LSDA + U calculations overestimate the smaller lobe and underestimate the larger one at both the L_3 and L_2 edges.

We found minor influence of the final-state interaction on the shape of the Gd $L_{2,3}$ XMCD spectra in the whole energy interval. A small core-hole effect might come from the fact that the Gd 5d states are less localized in comparison with the 4f states and have smaller amplitude inside the MT sphere and thus are less subject to the core hole potential.

A qualitative explanation of the XMCD spectra shape is provided by the analysis of the corresponding selection rules, orbital character and occupation numbers of individual 5d orbitals. Because of the electric dipole selection rules ($\Delta l = \pm 1$; $\Delta j = 0, \pm 1$) the major contribution to the absorption at the L_2 edge stems from the transitions $2p_{1/2} \to 5d_{3/2}$ and that at the L_3 edge originates primarily from $2p_{3/2} \to 5d_{5/2}$ transitions, with a weaker contribution from $2p_{3/2} \to 5d_{3/2}$ transitions. For the later case the corresponding $2p_{3/2} \to 5d_{3/2}$ radial matrix elements are only slightly smaller than for the $2p_{3/2} \to 5d_{5/2}$ transitions. The angular matrix elements, however, strongly suppress the $2p_{3/2} \to 5d_{3/2}$ contribution. Therefore the contribution to XMCD spectrum at the L_3 edge from the transitions with $\Delta j = 0$ is one order of magnitude smaller than the transitions with $\Delta j = 1$ [43].

The selection rules for the magnetic quantum number m_j (m_j is restricted to $-j, \ldots + j$) are $\Delta m_j = +1$ for $\lambda = +1$ and $\Delta m_j = -1$ for $\lambda = -1$. Table 1 presents the dipole allowed transitions for x-ray absorption spectra at the L_3 and L_2 edges for left ($\lambda = +1$) and right ($\lambda = -1$) polarized x-rays.

To go further, we need to discuss the character of the 3d empty DOS. Since l and s prefer to couple antiparallel for less than half-filled shells, the $j = l - s = 3/2$ has a lower energy than the $j = l + s = 5/2$ level. Due to the intra-atomic exchange interaction the lowest sublevel of the $j = 3/2$ will be $m_{3/2} = -3/2$, however, for the $j = 5/2$ the lowest sublevel will be $m_{5/2} = +5/2$. This reversal in the energy sequence arises from the gain in energy due to alignment of the spin with the exchange field.

Table 1. The dipole allowed transitions from core $2p_{1/2,3/2}$ levels to the unoccupied $5d_{3/2,5/2}$ valence states for left ($\lambda = +1$) and right ($\lambda = -1$) polarized x-rays

Edge	$\lambda = +1$	$\lambda = -1$
L_3	$-3/2 \to -1/2$	$-3/2 \to -5/2$
	$-1/2 \to +1/2$	$-1/2 \to -3/2$
	$+1/2 \to +3/2$	$+1/2 \to -1/2$
	$+3/2 \to +5/2$	$+3/2 \to +1/2$
L_2	$-1/2 \to +1/2$	$-1/2 \to -3/2$
	$+1/2 \to +3/2$	$+1/2 \to -1/2$

The contribution to the L_3 absorption spectrum from the first two transitions (Table 1) for $\lambda = +1$ cancels to a large extent with the contribution of opposite sign from the last two transitions for $\lambda = -1$ having the same final states. Thus the XMCD spectrum of Gd at the L_3 edge ($I = \mu^- - \mu^+$) can be approximated by the following sum of m_j-projected partial densities of states: $(N^{5/2}_{-5/2} + N^{5/2}_{-3/2}) - (N^{5/2}_{3/2} + N^{5/2}_{5/2})$. Here we use the notation $N^{j}_{m_j}$ for the density of states with the total momentum j and its projection m_j. From this expression one would expect the L_3 XMCD spectrum with two peaks of opposite signs with almost the same intensity. The corresponding L_2 XMCD spectrum can be approximated by the following partial DOS's: $(N^{3/2}_{-1/2} + N^{3/2}_{-3/2}) - (N^{3/2}_{1/2} + N^{3/2}_{3/2})$. From this expression one would also expect two peak structure of L_2 XMCD spectrum with an opposite signs. Besides, due to the reversal energy sequences for the $j = 3/2$ and $j = 5/2$ sublevels the energy positions of the positive and negative peaks are opposite to each other for the L_3 and L_2 XMCD spectra.

We should note, however, that the explanation of the XMCD line shape in terms of m_j-projected DOS's presented above should be considered as only qualitative. First, there is no full compensation between transitions with equal final states due to difference in the angular matrix elements; second, in our consideration we neglect cross terms in the transition matrix elements. Besides, we have used here the *jj*-coupling scheme, however, the combination of the hybridization, Coulomb, exchange and crystal-field energies may be so large relative to the 5d spin-orbit energy that the *jj*-coupling is no longer an adequate approximation.

The XMCD spectra at the Gd $L_{2,3}$ edges are mostly determined by the strength of the spin-orbit coupling of the initial Gd 2p core states and spin-polarization of the final empty $5d_{3/2,5/2}$ states while the exchange splitting of the Gd 2p core states as well as the SO coupling of the 5d valence states are of minor importance for the XMCD at the Gd $L_{2,3}$ edges of GdN.

The XAS and XMCD spectra in metals at the K edge in which the $1s$ core electrons are excited to the p states through the dipolar transition usually attract only minor interest because p states are not the states of influencing magnetic or orbital order. Recently, however, understanding p states has become important since XMCD spectroscopy using K edges of transition metals became popular. The K edge XMCD is sensitive to electronic structures at neighboring sites, because of the delocalized nature of the p states.

It is documented that sizable XMCD signals can be detected at the K edge of nonmagnetic atoms, like sulfur and oxygen in ferromagnetic EuS [44] and EuO [45], respectively. The experimental K edge photoabsorption and XMCD spectra of nitrogen in GdN were investigated by Leuenberger et al. [35]. It was found that the dichroic peak amplitude amounts to 4% of the edge jump of the isotropic XA spectrum at 401 eV (Fig. 5), which is a remarkably large value for K edge XMCD. The N K edge dichroic signal in GdN is about three times larger than at the K edge of oxygen in EuO and exceeds that at the K edge of sulfur in EuS by an order of magnitude; it surpasses even that at the onsite Fe K edge of iron metal where it is on the order of 0.3% [46].

A comparison of the XMCD spectra with the theoretical partial density of empty N p states calculated by Aerts et al. [47] shows considerable disparities that were not well understood [35]. Clearly, to reproduce the XMCD spectra one has to include the transition matrix elements.

Figure 5 shows the theoretically calculated x-ray absorption spectra at the N K edge as well as XMCD spectra in GdN in comparison with the corresponding experimental data [35]. The experimentally measured XA spectrum has a three peak structure. The first maximum in the spectrum is at around 400 eV which has a low energy shoulder not reproduced in the theoretical LSDA or LSDA + U calculations. The energy position of the theoretical second peak at around 402 eV is in good agreement with the experimental measurements. The position of the third high-energy peak is shifted to higher energy in the theory.

Figure 5,b shows the experimental XMCD spectrum [35] and theoretically calculated ones using the LSDA approximation and with 4f electrons placed in the core. The experimental spectrum is very complicated and consists of three positive (A, B, C) and two negative (D, F) peaks. The LSDA calculations as well the calculations with 4f electrons in the core give a completely inadequate description of the shape of N K XMCD spectrum. The most prominent discrepancy in the LSDA XMCD spectrum is the resonance structure with negative and positive peaks at around 396 to 398 eV which is caused by the strong hybridization of unoccupied Gd N p states with the 4f states situated too close to the Fermi level in the LSDA calculations. This structure disappears when we put 4f electrons in core.

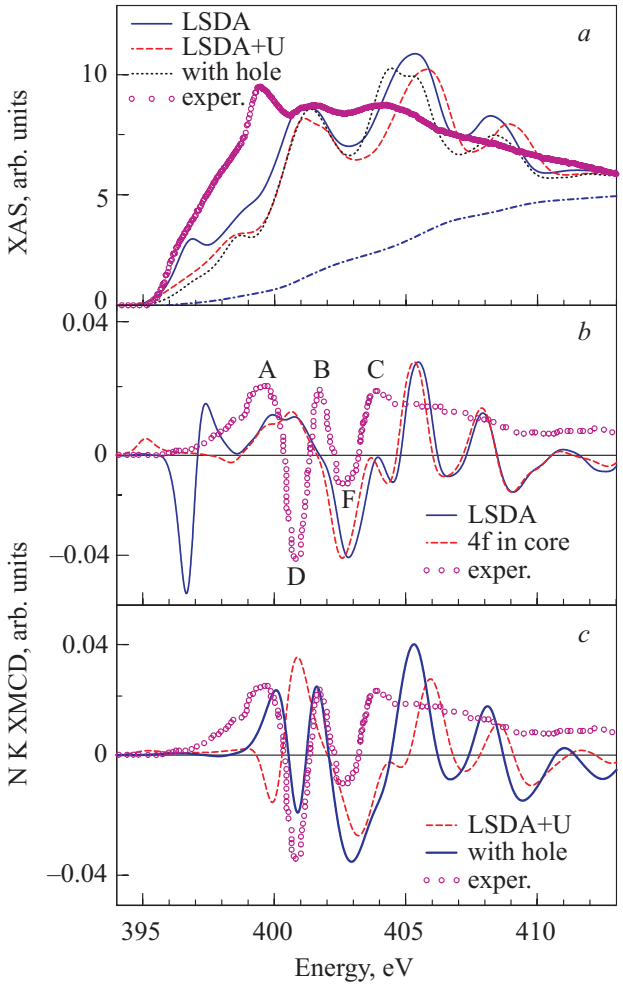

Fig. 5. (*a*) The experimental [35] (circles) isotropic absorption spectrum of GdN at the N K edge in comparison with the calculated ones [36] using the LSDA (full line) and LSDA + U approximations without (dashed line) and with (dotted line) taking into account the core hole-effect. Experimental spectra were measured with external magnetic field (0.1 T) at 15 K. Dashed-dotted line shows the theoretically calculated background spectrum. (*b*) Experimental [35] (circles) XMCD spectrum of GdN at the Gd K edge in comparison with theoretically calculated ones using the LSDA (full line) and putting the 4f states in core (dashed line) approximations; (*c*) experimental (circles) XMCD Gd K spectrum in comparison with theoretically calculated using the LSDA + U approximation with (full line) and without (dashed line) taking into account the core-hole effect.

The N 2p–Gd (4f, 5d) hybridization and the spin-orbit interaction in the 2p states play crucial roles for the N K edge dichroism. The K XMCD spectra come from the orbital polarization in the empty p states, which may be induced by (1) the spin polarization in the p states through the spin-orbit interaction, and (2) the orbital polarization at neighboring sites through hybridization. We calculated

the K XMCD spectrum at N site with turning the SOI off separately on the N $2p$ states and at the Gd site (at both the $4f$ and $5d$ states), respectively. We found that the K XMCD spectrum is slightly changed when the SOI on the N site is turned off, while the spectrum almost disappears (reduced its intensity almost two order of magnitude) when the SOI on the Gd site is turned off. This indicates that the SOI on Gd site is influencing the orbital mixture of N $2p$ states through the N ($2p$)–Gd (d, f) hybridization.

The LSDA + U approach (Fig. 5,*c*) improves the agreement between theory and the experiment, especially in describing the peak B. However, LSDA + U theory fails to produce the peak A, besides the peaks B and D are shifted toward lower energy at around 0.6 eV in comparison with the experimental measurements. Also for the energies higher than peak C theory gives some additional oscillating structures, while the experimental spectrum is a smooth positive function of energy.

We investigate also the core-hole effect in the final state using the supercell approximation. In our calculations we used a supercell containing eight conventional GdN cells. At one of the eight N atoms we create a hole at the $1s$ level for the self-consistent LSDA + U calculations of the K spectrum. We found that the core-hole interactions significantly improve the agreement between theoretically calculated and experimentally measured N K XMCD spectra (Fig. 5,*c*). The oscillation behavior of the high-energy part of the theoretical spectrum above 405 eV could possibly be damped by the quasiparticle life-time effect, which is not taken into account in our calculations. The core-hole effect improves also the agreement in the energy position of the third high-energy peak in the XAS (Fig. 5,*a*).

However, all the calculations were not able to produce the first maximum of the N K XAS above the edge at around 400 eV. One of the possible reasons for such disagreements might be the surface effect. The N K edge occurs at a relatively small energy and one would expect larger surface affects at the N K edge than, for example, at the Gd $M_{4,5}$ or $L_{2,3}$ edges. To model the surface effects we carried out band structure calculations using a tetragonal supercell containing 4 unit cells of GdN along the z direction in which 3 GdN layers are replaced by 3 layers of empty spheres. We calculated the XAS and XMCD spectra at N K edge for such a 5 layer slab separated by 3 layers of empty spheres (5/3 multilayered structure (MLS)) using the LSDA + U approximation. We also carried out the band structure calculations for a 9 layer slab separated by 3 layers of empty spheres (9/3 MLS). We found that the K XMCD spectrum for N in the middle of the 9/3 MLS (5th layer) is identical to the corresponding bulk LSDA + U spectrum (not shown). The corresponding spectrum for the middle layer in the 5/3 MLS (3th layer) is still slightly different from the bulk spectrum, therefore the convergence was achieved only in the 9/3 MLS. Figure 6 shows the N p empty partial DOS's for the surface layer in the 9/3 MLS and the bulk structure in comparison with the experimental XA spectrum at the N K edge. It can be seen that the partial DOS strongly increases at the first maximum above the edge for the surface layer.

Actually the importance of the surface effect has some experimental evidence. The authors of Ref. 35 mention that the spectral feature at 400 eV was not contained in a preliminary N K edge XA spectrum recorded on a Cr-covered 30 Å GdN layer using the total fluorescence yield detection mode due to the larger probing depth of this method compared to the measurements with the total electron yield (TEY) detection in Ref. 35. This indicates that the first maximum above the edge in the XA spectrum at 400 eV is likely related to the GdN surface or interface where the TEY detection is sensitive. The peak is a signature of the surface GdN XA behavior of the sample. This also applies for the slowly rising part of the XMCD signal below 400 eV. This result supports our conclusion that the first maximum above the edge in the XA spectrum might be related to the GdN surface or interface.

It is also important to note that the energy position of the first XA maximum above the edge at around 400 eV coincides with the position of the Gd $4f$ DOS and any kind of change in the N $2p$–Gd $4f$ hybridization (which we discussed in previous paragraph) might influence the intensity of the XAS at that energy. The possible existence of interstitial N atoms may also influence the low-energy part of the spectrum via stronger direct Gd $4f$–N $2p$ hybridization.

Due to the delocalized nature of the p states and wide spread of p wave functions K XMCD spectra are very sensitive to the surrounding neighborhood and, hence, the K XMCD spectroscopy can be used as an effective probe which can detect details of magnetic interatomic interactions in rare-earth compounds.

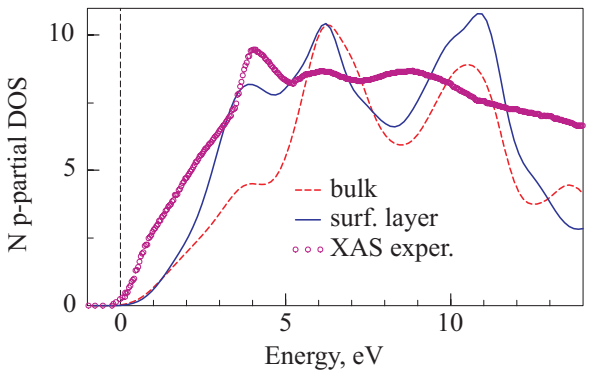

Fig. 6. N p empty partial DOS's (in arbitrary units) for the surface layer in the 9/3 MLS (full line) and the bulk structure (dashed line) [36] in comparison with the experimental XA spectrum at the N K edge [35] (circles).

2. Uranium compounds

Uranium compounds exhibit rich variety of properties to large extent because of the complex behavior of $5f$ electrons which is intermediate between the itinerant behavior of $3d$ electrons in transition metals and the localized one of $4f$ electrons in rare-earth compounds. The dual character of $5f$ electrons alongside with the presence of strong spin-orbit coupling make the determination of the electronic structure of U compounds a challenging task because in many of them the width of $5f$ bands, their spin-orbit splitting, and the on-site Coulomb repulsion in the partially filled $5f$ shell are of the same order of magnitude and should be taken into account on the same footing. An interest to uranium compounds has recently been renewed, especially after the discovery of such unusual effects as heavy fermion superconductivity and coexistence of superconductivity and magnetism.

Because of the great number of papers which have been produced in recent years on actinide intermetallics, and in particular on heavy-fermion compounds, these would deserve one or more specialized review articles. Various aspects of these systems and of general heavy-fermion systems have already been reviewed in the past [48–60]. For this reason we will merely outline some general concepts relevant to uranium intermetallics, rather than doing a systematic review of all their physical properties.

For heavy-fermion compounds the attribute «heavy» is connected to the observation of a characteristic energy much smaller than in ordinary metals that reflects a thermal effective mass m^* of the conduction electrons orders of magnitude larger than the bare electron mass. These heavy masses manifest themselves, for example, by a large electronic coefficient γ of the specific heat C ($\gamma = C/T$ for $T \to 0$), an enhanced Pauli susceptibility, a huge T^2 term in the electrical resistivity, and highly temperature-dependent de Haas–van Alphen oscillation amplitudes at very low temperatures. The large m^* value is usually believed to derive from the strong correlation electrons. While at high temperature the $5f$ electrons and conduction electrons interact weakly, at low temperature these two subsets of electrons become strongly coupled, resulting in the formation of a narrow resonance in the density of states near the Fermi energy. Thus, at a sufficiently low temperature, the heavy-fermion compounds behave like a system of heavy itinerant electrons, the properties of which can be described in the framework of a Landau Fermi-liquid formalism.

Among uranium heavy-fermion compounds superconductivity is observed in UBe_{13}, UPt_3, URu_2Si_2, U_2PtC_2, UPd_2Al_3, and UNi_2Al_3. Superconductivity usually in these compounds coexists with AF order and this has led to the suggestion that the effective attractive interaction between the superconducting electrons may be mediated by spin fluctuations, rather than by the electron-phonon interaction. This is supported by the fact that the observed superconducting states are highly anisotropic, with nodes in the gap function not explainable by a *s*-wave theory.

A fascinating aspect of this class of compounds is the observation that, within the heavy-fermion regime, a wealth of ground states can occur. Although a myriad of experiments have been devoted to the characterization of these ground states, a comprehensive understanding of heavy-fermion properties at low temperature is still lacking. The heavy-fermion ground-state properties are highly sensitive to impurities, chemical composition, and slight changes of external parameters. This sensitivity indicates that a subtle interplay between different interactions produces a richness of experimental phenomena. It is widely believed that the competition between the Kondo effect (reflecting the interaction between the localized $5f$ moments and the conduction electrons) and the magnetic correlations between the periodically arranged $5f$ moments constitutes the key factor for as far as the magnetic properties of heavy-fermion compounds are concerned [48].

The x-ray magnetic circular dichroism technique developed in recent years has evolved into a powerful magnetometry tool to separate orbital and spin contributions to element specific magnetic moments. Study of the $5f$ electron shell in uranium compounds is usually performed by tuning the energy of the x-ray close to the $M_{4,5}$ edges of uranium (located at 3552 and 3728 eV, respectively) where electronic transitions between $3d_{3/2,5/2}$ and $5f_{5/2,7/2}$ states occur. Recently XMCD measurements have been successfully performed for uranium compounds such as US [61,62], $USb_{0.5}Te_{0.5}$ [63], $U_xLa_{1-x}S$ [64], UBe_{13} and UPt_3 [65], UFe_2 [66,67], UNi_2Al_3 [68], UPd_2Al_3 and URu_2Si_2 [69], URhAl [70], UCoAl and UPtAl [71]. There are some features in common for all the uranium compounds investigated up to now. First, the dichroism at the M_4 edge is much larger, sometimes of one order of magnitude, than at the M_5 one. Second, the dichroism at the M_4 edge has a single negative lobe that has no distinct structure, on the other hand, two lobes, a positive and a negative one, are observed at the M_5 edge. Concerning the line shape of the XMCD signal, the investigated metallic uranium compounds fall into two types according to a relative intensity of the positive and negative lobes observed at the M_5 edge. The two lobes have almost equal intensity for UP_3, UPd_2Al_3, UPtAl, and UBe_{13}. On the other hand, the positive lobe is smaller in comparison with the negative one for US, $USb_{0.5}Te_{0.5}$, UFe_2, URu_2Si_2, UCoAl, and URhAl.

With the aim of undertaking a systematic investigation of the trends in uranium compounds we present the theoretically calculated electronic structure and XMCD spectra at $M_{4,5}$ edges for the following uranium compounds:

UPt_3, URu_2Si_2, UPd_2Al_3, UNi_2Al_3, UBe_{13}, UFe_2, UPd_3, UXAl (X = Co, Rh, and Pt), and UX (X = S, Se, and Te). The first five compounds belong to heavy-fermion superconductors, UFe_2 is widely believed to be an example of compound with completely itinerant $5f$ electrons, while UPd_3 is the only known compound with completely localized $5f$ electrons. The electronic structure and XMCD spectra of UGe_2 which possesses simultaneously ferromagnetism and superconductivity also presented.

2.1. Intermetallic compounds

2.1.1. UFe_2

Figure 7 shows the calculated fully relativistic spin-polarized partial $5f$ density of states of ferromagnetic UFe_2 [72]. Because of the strong spin-orbit interaction of $5f$ electrons, $j = 5/2$ and $j = 7/2$ states are well separated in energy and the occupied states are composed mostly of $5f_{5/2}$ states whereas $5f_{7/2}$ states are almost empty. One can note, however, that an indirect hybridization between $j = 5/2$ and $j = 7/2$ states via Fe $3d$ states is rather strong.

In order to compare relative amplitudes of M_4 and M_5 XMCD spectra we first normalize the corresponding isotropic x-ray absorption spectra (XAS) to the experimental ones taking into account the background scattering intensity. Figure 8 shows the calculated isotropic x-ray absorption and XMCD spectra in the LSDA and LSDA + U(OP) approximations together with the experimental data [66]. The contribution from the background scattering is shown by dashed lines in the upper panel of Fig. 8.

The experimentally measured dichroic M_4 line consists of a simple nearly symmetric negative peak that has no distinct structure. Such a peak is characteristic of the M_4 edge of all uranium systems. The dichroic line at the M_5 edge has an asymmetric s shape with two peaks — a stronger negative peak and a weaker positive peak. The dichroism at the M_4 edge is more than two times larger than at the M_5 one.

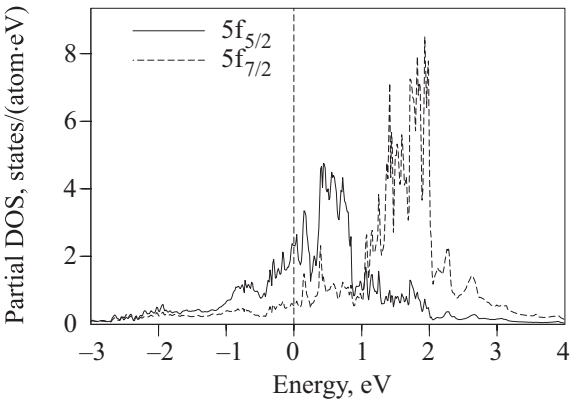

Fig. 7. The LSDA partial $5f_{5/2}$ and $5f_{7/2}$ density of states in UFe_2 [72].

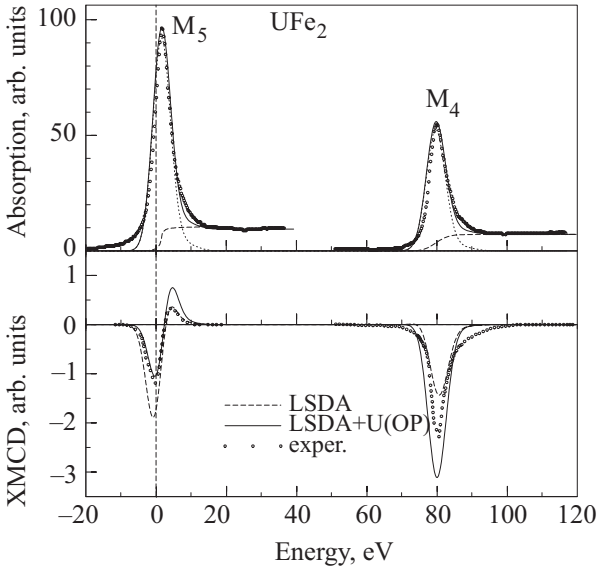

Fig. 8. Isotropic absorption and XMCD spectra of UFe_2 at the uranium $M_{4,5}$ edges calculated in the LSDA (solid lines) and LSDA + U(OP) (dashed lines) approximations [72]. Experimental spectra [66] (circles) were measured at 20 K and at magnetic field 2 T (the U M_4 spectrum is shifted by –95 eV to include it in the figure). Upper panel also shows the background spectra (dashed line) due to the transitions from inner $3d_{3/2,5/2}$ levels to the continuum of unoccupied levels.

Because of the electric dipole selection rules ($\Delta l = \pm 1$; $\Delta j = 0, \pm 1$) the major contribution to the absorption at the M_4 edge stems from the transitions $3d_{3/2} \to 5f_{5/2}$ and that at the M_5 edge originates primarily from $3d_{5/2} \to 5f_{7/2}$ transitions, with a weaker contribution from $3d_{5/2} \to 5f_{5/2}$ transitions. For the later case the corresponding $3d_{5/2} \to 5f_{7/2}$ radial matrix elements are only slightly smaller than for the $3d_{5/2} \to 5f_{7/2}$ transitions. The angular matrix elements, however, strongly suppress the $3d_{5/2} \to 5f_{5/2}$ contribution. Therefore the contribution to XMCD spectrum at M_5 edge from the transitions with $\Delta j = 0$ is about 15 times smaller than the transitions with $\Delta j = 1$.

The selection rules for the magnetic quantum number m_j (m_j is restricted to $-j, \ldots +j$) are $\Delta m_j = +1$ for $\lambda = +1$ and $\Delta m_j = -1$ for $\lambda = -1$. Table 2 presents the dipole allowed transitions for x-ray absorption spectra at M_5 and M_4 edges for left ($\lambda = +1$) and right ($\lambda = -1$) polarized x-rays.

To go further, we needs to discuss the characteristic of the $5f$ empty DOS. Since l and s prefer to couple antiparallel for less than half-filled shells, the $j = l - s = 5/2$ has a lower energy than the $j = l + s = 7/2$ level. Due to the intra-atomic exchange interaction the lowest sublevel of the $j = 5/2$ will be $m_{5/2} = -5/2$, however, for the $j = 7/2$ the lowest sublevel will be $m_{7/2} = +7/2$. This reversal in the

energy sequence arises from the gain in energy due to alignment of the spin with the exchange field [65].

Table 2. The dipole allowed transitions from core $3d_{3/2,5/2}$ levels to the unoccupied $5f_{5/2,7/2}$ valence states for left ($\lambda = +1$) and right ($\lambda = -1$) polarized x-rays

Edge	$\lambda = +1$	$\lambda = -1$
M_5	$-5/2 \to -3/2$	$-5/2 \to -7/2$
	$-3/2 \to -1/2$	$-3/2 \to -5/2$
	$-1/2 \to +1/2$	$-1/2 \to -3/2$
	$+1/2 \to +3/2$	$+1/2 \to -1/2$
	$+3/2 \to +5/2$	$+3/2 \to +1/2$
	$+5/2 \to +7/2$	$+5/2 \to +3/2$
M_4	$-3/2 \to -1/2$	$-3/2 \to -5/2$
	$-1/2 \to +1/2$	$-1/2 \to -3/2$
	$+1/2 \to +3/2$	$+1/2 \to -1/2$
	$+3/2 \to +5/2$	$+3/2 \to +1/2$

The $5f_{7/2}$ states are almost completely empty in all the uranium compounds. Therefore all the transitions listed in Table 2 are active in the M_5 absorption spectrum. The contribution from the first four transitions for $\lambda = +1$ cancels to a large extent with the contribution of the opposite sign from the last four transitions for $\lambda = -1$ having the same final states. Thus the XMCD spectrum of U at the M_5 edge ($I = \mu^- - \mu^+$) can be roughly approximated by the following sum of m_j-projected partial densities of states [72]: $(N^{7/2}_{-7/2} + N^{7/2}_{-5/2}) - (N^{7/2}_{7/2} + N^{7/2}_{5/2})$. Here we use the notation $N^j_{m_j}$ for the density of states with the total momentum j and its projection m_j. As a result, the shape of the M_5 XMCD spectrum contains of two peaks of opposite signs — a negative peak at lower energy and a positive peak at higher energy. As the separation of the peaks is smaller than the typical lifetime broadening, the peaks cancel each other to a large extent, thus leading to a rather small signal. Since the splitting of states with $m_j = \pm |m_j|$ increases with the increase of the magnetization at the U site, the amplitude of the M_5 spectrum should be proportional to the U magnetic moment.

A rather different situation occurs in the case of the M_4 x-ray absorption spectrum. Usually in uranium compounds the U atom is in $5f^3$ (U^{3+}) or $5f^2$ (U^{4+}) configurations and has partly occupied $5f_{5/2}$ states. In the first case the $5f_{5/2}$ states with $m_j = -5/2$, $-3/2$, and $-1/2$ are usually occupied. The dipole allowed transitions for $\lambda = +1$ are $-1/2 \to +1/2$, $+1/2 \to +3/2$ and $+3/2 \to +5/2$ and those for $\lambda = -1$ are $+3/2 \to +1/2$. The transitions with the same final states $m_j = +1/2$ mostly cancel each other and the XMCD spectrum of U at the M_4 edge can be roughly represented by the sum [72] $-(N^{5/2}_{3/2} + N^{5/2}_{5/2})$. The corresponding analysis for the $5f^2$ (U^{4+}) configuration with occupied $f_{5/2,-5/2}$ and $f_{5/2,-3/2}$ states shows that the dipole allowed transitions for $\lambda = +1$ are $-3/2 \to -1/2$, $-1/2 \to +1/2$, $+1/2 \to +3/2$, and $+3/2 \to +5/2$ and for $\lambda = -1$: $+1/2 \to -1/2$ and $+3/2 \to +1/2$. Again, the XMCD spectrum of U at the M_4 edge can be approximated by $-(N^{5/2}_{3/2} + N^{5/2}_{5/2})$ [72]. This explains why the dichroic M_4 line in uranium compounds consists of a single nearly symmetric negative peak.

We should note, however, that the explanation of the XMCD line shape in terms of m_j-projected DOS's presented above should be considered as only qualitative. First, there is no full compensation between transitions with equal final states due to difference in the angular matrix elements; second, in our consideration we neglect cross terms in the transition matrix elements; third, there is no pure $5f^3$ or $5f^2$ configurations in uranium compounds. It is always difficult to estimate an appropriate atomic $5f$ occupation number in band structure calculations. Such a determination is usually obtained by the integration of the $5f$ electron charge density inside of the corresponding atomic sphere. In the particular UFe_2 case, the occupation number of U $5f$ states is around 2.9 in the LSDA calculations. We, however, should keep in mind that some amount of the $5f$ states are derived from the so-called «tails» of Fe $3d$ states arising as a result of the decomposition of the wave function centered at Fe atoms. The careful analysis in the case of UPd_3 presented in Ref. 73 shows that the occupation number of the «tails» of Pd $4d$ states sum up to give the $5f$ occupation of 0.9 electrons in the U atomic sphere. We should also note that due to the strong hybridization between U $5f$ and Fe $3d$ states, the U $5f_{7/2}$ states in UFe_2 are not completely empty, some of them are occupied, also some amount of U $5f_{5/2}$ states, which we have been considering as fully occupied, are partially empty.

The overall shapes of the calculated and experimental uranium $M_{4,5}$ XMCD spectra correspond well to each other (Fig. 8). The major discrepancy between the calculated and experimental XMCD spectra is the size of the M_4 XMCD peak. The LSDA underestimates the integral intensity of the XMCD at the M_4 edge. As the integrated XMCD signal is proportional to the orbital moment [74] this discrepancy may be related to an underestimation of the orbital moment by LSDA-based computational methods. On the other hand, the LSDA + U(OP) approximation gives larger intensity for the M_4 XMCD spectrum in comparison with the experimentally measured one. It reflects the overestimation of the orbital moment at U site in the LSDA + U(OP) calculations. In the case of the M_5 XMCD spectrum, the LSDA reproduces the amplitude of the positive peak and overestimates the amplitude of the

negative peak. The LSDA + U(OP) approximation, in contrast, gives good agreement in the amplitude of the negative peak but overestimates that of the positive peak.

To investigate the influence of the initial state on the resulting U XMCD spectra we calculated also the XAS and XMCD spectra of UFe_2 compound at the $N_{4,5}$ and $O_{4,5}$ edges (not shown). We found a substantial decrease of the XMCD in terms of $R = \Delta\mu/(2\mu^0)$ at $N_{4,5}$ edges in comparison with the $M_{4,5}$ ones. The theoretically calculated dichroic N_4 line consists of a simple nearly symmetric negative peak that has no distinct structure as was observed at the M_4 XMCD spectrum. The LSDA calculations give much smaller dichroic signal at the N_4 edge in comparison with the LSDA + U(OP) calculations. The dichroic line at the N_5 edge is reminiscent of the corresponding M_5 spectrum and has an asymmetric s shape with two peaks — a stronger negative peak and much weaker positive peak. In contrast to the dichroism at the $M_{4,5}$ edges where XMCD at M_4 edge is more than two times larger than at the M_5 one, the dichroism at the N_4 edge has almost the same intensity as at the N_5 edge.

Due to MO selection rules the O_4 XMCD spectrum resembles the M_4 spectrum, whereas the O_5 spectrum is similar to the M_5 one. Because of the relatively small spin-orbit splitting of the 5d states of U (~ 11 eV), the O_4 and O_5 spectra almost overlap each other. The magnetic dichroism at quasi-core $O_{4,5}$ edges is of one order of magnitude larger than the dichroism at the $N_{4,5}$ edges and become almost as large as that at the $M_{4,5}$ edge. Besides, the lifetime broadening of the core $O_{4,5}$ levels is much smaller than the broadening of the $M_{4,5}$ ones [75]. Therefore the spectroscopy of U atoms in the ultra-soft x-ray energy range at the $O_{4,5}$ edges may be a very useful tool for investigation of the 5f electronic states in magnetic U materials.

The XAS at the $M_{4,5}$, $N_{4,5}$, and $O_{4,5}$ edges involve electronic transitions between $nd_{3/2,5/2}$ (n = 3, 4, and 5) and $5f_{5/2,7/2}$ states and therefore are used to study of the 5f empty electronic states in uranium compounds. To investigate the 6d states of U one should tune the energy of the x-ray close to the $M_{2,3}$, $N_{2,3}$, $O_{2,3}$, or $N_{6,7}$ edges of uranium. The first three doublets are due to the $np_{1/2,3/2} \to 6d_{3/2,5/2}$ (n = 3, 4, and 5) interband transitions.

Figure 9 presents the theoretically calculated XMCD spectra of U $M_{2,3}$, $N_{2,3}$, and $O_{2,3}$ edges. The XMCD signals at these edges are two order of magnitude less than the corresponding signals at the $M_{4,5}$ edges.

Because of the dipole selection rules, apart from the $ns_{1/2}$ states (which have a small contribution to the XAS's due to relatively small $np \to 7s$ matrix elements only $6d_{3/2}$ states occur as final states for the M_2, N_2, and O_2 XAS's for unpolarized radiation, whereas for the M_3, N_3, and O_3 XAS's the $6d_{5/2}$ states also contribute. Although the $np_{3/2} \to 6d_{3/2}$ radial matrix elements are only slightly

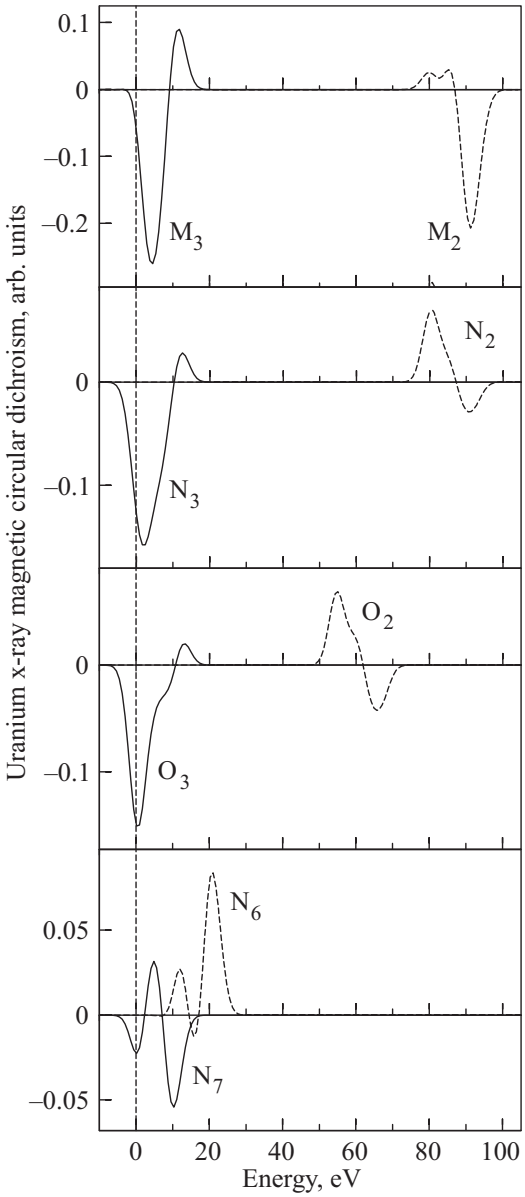

Fig. 9. XMCD spectra of UFe_2 at the uranium $M_{2,3}$, $N_{2,3}$, $O_{2,3}$ and $N_{6,7}$ edges calculated in the LSDA approximation [72]. All the XMCD spectra are multiplied by a factor 10^2 (the M_2 and N_2 spectra are shifted by –800 and –150 eV, respectively, to include them in the figure).

smaller than for the $np_{3/2} \to 6d_{5/2}$ transitions the angular matrix elements strongly suppress the $np_{3/2} \to 6d_{3/2}$ contribution. Therefore, neglecting the energy dependence of the radial matrix elements, the M_2, N_2, and O_2 absorption spectra can be viewed as a direct mapping of the DOS curve for $6d_{3/2}$, and the M_3, N_3, and O_3 XAS's reflect the DOS curve for $6d_{5/2}$ states. The shape of X_3 ($X = M, N$, or O) XMCD spectra consists of two peaks of opposite sign — a negative peak at lower energy and a positive peak at higher energy. The shape of X_2 ($X = M, N$, or O) XMCD spectra also have two peaks of an opposite sign,

but the negative peaks situated at higher energy and the positive peak at lower energy (Fig. 9).

Figure 9 also presents the theoretically calculated XMCD spectra at U $N_{6,7}$ edges. Because of the electric dipole selection rules the major contribution to the absorption at the N_7 edge stems from the transitions $4f_{7/2} \to 6d_{5/2}$ and that at the N_6 edge originates primarily from $4f_{5/2} \to 6d_{3/2}$ transitions (the contribution from $4f_{5/2} \to 6d_{5/2}$ transitions are strongly suppressed by the angular matrix elements). The XMCD signals at these edges are even smaller than the corresponding signals at the $X_{2,3}$ ($X = M, N$, or O) edges. Because of the relatively small spin-orbit splitting of the $4f$ states of U, the N_6 and N_7 spectra have an appreciable overlap. Besides, in the case of $N_{6,7}$ XAS one would expect a strong electrostatic interaction between the created $4f$ core hole and the valence states. It can lead to an additional multiplet structure in the XAS and XMCD spectra at the $N_{6,7}$ edges. We have not considered multiplet structure in our XMCD calculations. This structure can be captured using full atomic multiplet structure calculations.

We also calculated the x-ray magnetic circular dichroism at the Fe K, $L_{2,3}$, and $M_{2,3}$ edges, with the results being presented in Fig. 10. For comparison we also show the XMCD spectra in bcc Fe. Although the XMCD signal at the Fe K edge has almost the same amplitude both in bcc Fe and UFe_2, their shapes are quite different (Fig. 10).

The dichroism at Fe L_2 and L_3 edges is influenced by the spin-orbit coupling of the initial $2p$ core states. This gives rise to a very pronounced dichroism in comparison with the dichroism at the K edge. Figure 10 shows the theoretically calculated Fe $L_{2,3}$ XMCD spectra in UFe_2 and bcc Fe. The dichroism at the L_3 edge has a negative sign and at the L_2 edge a positive one. The XMCD dichroic signals at the Fe $L_{2,3}$ and $M_{2,3}$ edges are three times smaller in UFe_2 than the corresponding XMCD in bcc Fe due to strongly reduced magnetic moment at the Fe site in UFe_2 in comparison with pure Fe. Besides, the shape of the spectra is more asymmetrical in UFe_2.

The magnetic dichroism at the Fe $M_{2,3}$ edges is much smaller than at the $L_{2,3}$ edges (Fig. 10). Besides the M_2 and the M_3 spectra are strongly overlapped and the M_3 spectrum contributes to some extent to the structure of the total $M_{2,3}$ spectrum in the region of the M_2 edge. To decompose a corresponding experimental $M_{2,3}$ spectrum into its M_2 and M_3 parts will therefore be quite difficult in general. It worth mentioning that the shape of Fe L_3 and M_3 XMCD spectra are very similar.

2.1.2. UXAl (X = Co, Rh, *and* Pt)

The group of ternary uranium compounds with composition UTX, where T is a transition metal (Fe–Ni and 4*d*, 5*d* equivalents) and X a *p* element (Al, Ga, Ge, Sn), has

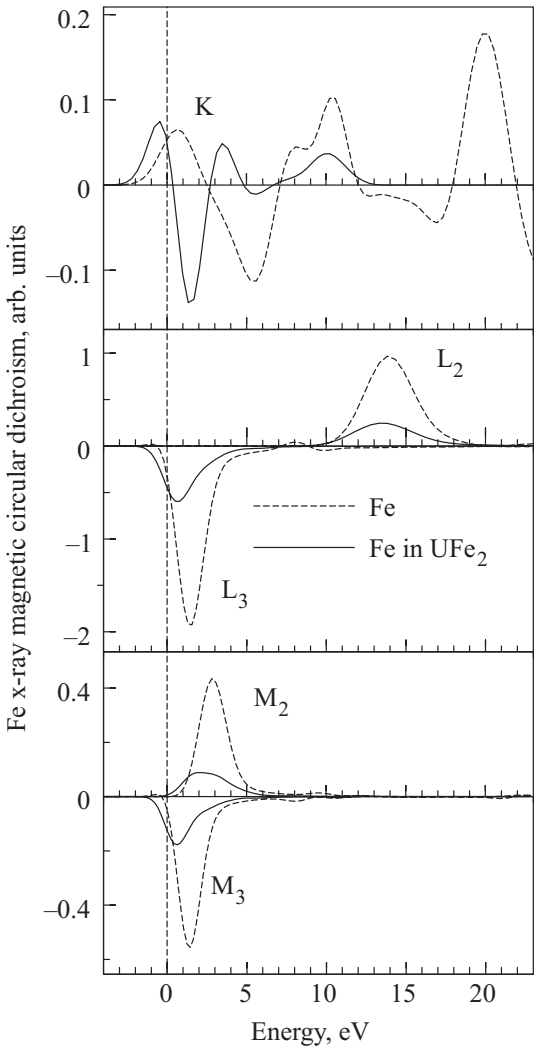

Fig. 10. XMCD spectra of UFe_2 at the Fe K, $L_{2,3}$, and $M_{2,3}$ edges in bcc Fe and Fe in UFe_2 calculated in the LSDA approximation [72]. The XMCD spectrum at the K edge has been multiplied by a factor 10^2.

recently attracted attention [76]. These compounds provide wide possibilities for study via the variation of atom types. The compounds forming with atoms to the left of the transition metal series (Fe, Co, and Ru) are paramagnetic — although UCoAl is metamagnetic — while URhAl, UIrAl and UPtAl are ferromagnetic and UNiAl is antiferromagnetic.

One of the key questions to be addressed when discussing actinide compounds is the degree of localization of the $5f$ electrons, which may range from nearly localized to practically itinerant, depending on the specific compound. Since the $5f$ electrons are simultaneously involved in the chemical bonding and magnetism, a broad variety of physical properties may emerge from the degree of $5f$ localization. UTAl (T = Co, Rh, and Pt) compounds have been also considered in this respect [71,77–80].

UCoAl shows no magnetic ordering down to the lowest temperatures, but in a relatively low magnetic field, of about 0.7 T, applied along the *c* axis a metamagnetic transition to a ferromagnetic state is observed at low temperatures. The metamagnetic transition in UCoAl is attributed to band metamagnetism [71]. The metamagnetism is induced only when the magnetic field is applied along the *c* axis, whereas in fields in a perpendicular direction UCoAl behaves like a Pauli paramagnet and no metamagnetic transition is observed in magnetic fields up to 42 T [77]. The strong uniaxial magnetic anisotropy is preserved in UCoAl, at least up to room temperature. It is of interest to note a rather low ordered magnetic moment of UCoAl which amounts to 0.30 μ_B/f.u. at 4.2 K, above the metamagnetic transition. The moment steadily increases with magnetic field, showing no saturation tendency up to 35 T where it reaches the value of 0.6 μ_B/f.u. [77,78].

The UPtAl compound is an appropriate reference system for the same structure and with composition and bonding similar to that of UCoAl. It orders ferromagnetically below a T_C of 43 K with a saturated magnetization of 1.38 μ_B/f.u. at 2 K in fields applied along the *c* axis [81]. The strong uniaxial anisotropy is manifested by the fact that the magnetization measured along the *a* axis is much smaller and has no spontaneous component. In fact, it resembles the magnetic response of a paramagnet exhibiting 0.28 μ_B/f.u. at 40 T.

As for the URhAl compound, a sizable induced moment of 0.28 μ_B on the Rh atom within the basal uranium plane was detected in a polarized neutron study, whereas, interestingly, only a very small induced moment of 0.03 μ_B was detected on the equally close Rh site out of the plane [79]. The large anisotropy in the induced Rh moments clearly reflects the anisotropy of the U(5*f*)–Rh(4*d*) hybridization: a strong hybridization occurs between the valence orbitals of the U and Rh atoms within the basal plane, but the hybridization between the valence orbitals of the U atom and those of the equally close Rh atom in the adjacent plane is much smaller.

Later, inelastic neutron-scattering experiments found a peak at 380 meV, which was interpreted as the signature of an intermultiplet transition [80], thus promoting the localized picture. The 380 meV peak occurred at the same energy where a uranium intermultiplet transition was observed [82] in UPd_3, which is one of the uranium compounds where the 5*f* electrons are undoubtedly localized.

Five electronic band structure calculations for URhAl were carried out recently [71,83–86]. These indicated, first, that the bonding and magnetism are governed by the U (5*f*)–Rh (4*d*) hybridization [84] and, second, that the calculated magneto-optical Kerr spectrum [83] — based on the assumption of delocalized 5*f*'s — compares reasonably well to the experimental Kerr spectrum. Besides, the authors of Ref. 85 were able to describe satisfactory the equilibrium volume, bulk modulus, and magnetocrystalline anisotropy in URhAl using the LSDA-based full potential relativistic LAPW method. Somewhat less well explained were the uranium orbital moment and the XMCD spectra.

Experimental and theoretical x-ray magnetic circular dichroism studies of the intermetallic compounds UCoAl and UPtAl at the uranium M_4 and M_5 edges are reported in Ref. 71. The results show that the orbital-to-spin moment ratio is of comparable value, $M_l/M_s \sim -2$, for both compounds. The reduction of the M_l/M_s ratio compared to the U^{3+} ($5f^3$) free ion value of –2.57, and the sizable decrease of orbital and spin moments, especially for UCoAl, indicate a significant delocalization of the 5*f* electron states in these compounds.

1. Band structure. UTAl (T = Co, Rh, or Pt) crystallize in the hexagonal ZrNiAl structure (Fe_2P type), which contains three formula units per unit cell. The ZrNiAl structure has a layered structure, consisting of planes of uranium atoms admixted with one-third of the T atoms, that are stacked along the *c* axis, while two adjacent uranium planes are separated from one another by a layer consisting of the remaining T atoms and the Al atoms. The uranium atoms have transition metal nearest neighbors and vice versa, so both uranium and T atoms are well separated from atoms of the same type. The uranium interlayer exchange coupling is relatively weak and depends sensitively on the specific T elements, which gives rise to a variety of magnetic behaviors observed in the UTX compounds [76].

The fully relativistic spin-polarized LSDA energy band structure and total density of states of the ferromagnetic UTAl (T = Co, Rh, and Pt) compounds are shown in Fig. 11 [86]. The bands in the lowest region of UPtAl, between –9.2 and –6.0 eV, have mostly Al *s* character with a small amount of U *spd* and Al *p* character mixed in. The energy bands between –6.0 and –3.0 eV are predominantly Pt 5*d* states. Due to increasing of the spatial expansion of valence transition metal *d* states in going from Co to Pt the corresponding *d* energy widths are increased and shifted downwards. Co 3*d* energy bands are occupied in the –1.2 to –2.8 eV energy interval in UCoAl, the 4*d* bands of Rh in URhAl are situated in the –2.0 to –4.5 eV energy range, and Pt 5*d* bands are in the –3.0 to –6.0 eV interval. Therefore the valence *d* energy band widths are equal to 1.6, 2.5, and 3.0 eV in UCoAl, URhAl, and UPtAl, respectively (Fig. 11). The U 5*f* energy bands occupy the same energy interval above and below E_F in all the compounds under consideration, namely, about –1.0 to 2.0 eV. There is a strong hybridization between the U 6*d*, transition metal *d*, and Al *p* states.

The itinerant character of electron states usually implies a strong reduction of the orbital magnetic moment with respect to the free-atom expectation value. Never-

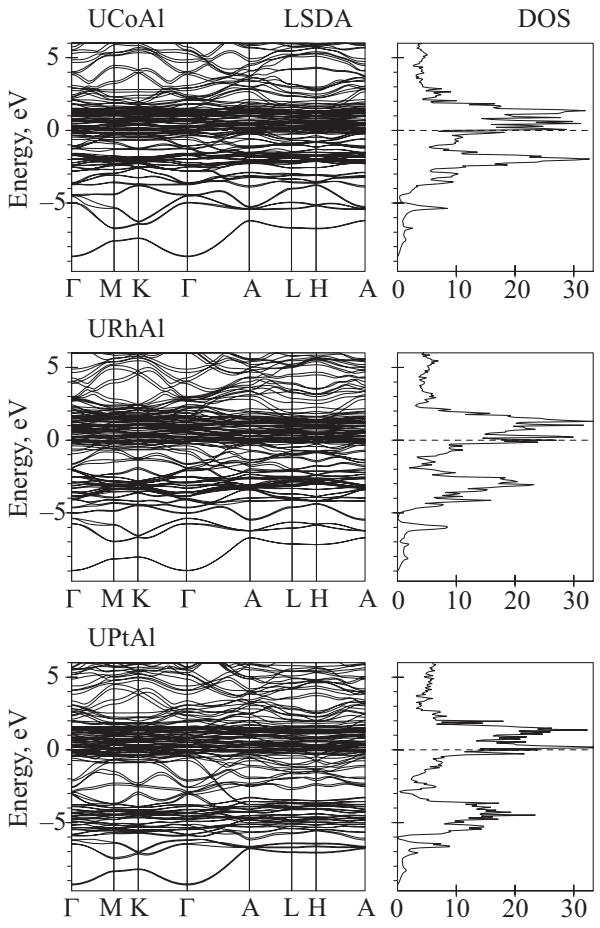

Fig. 11. The LSDA self-consistent fully relativistic, spin-polarized energy band structure and total DOS (in states/(unit cell·eV)) of UCoAl, URhAl, and UPtAl [86].

theless, in contrast to 3*d* electrons in transition metals, sizable orbital magnetic moments are observed in U intermetallic compounds with apparently strongly delocalized 5*f* electrons. It is the very strong spin-orbit coupling present in actinides that enhances an orbital moment in the case of itinerant 5*f* electron states. Analyzing spin and orbital magnetic moments in various actinide compounds, Lander et al. suggested that the ratio of the orbital to the spin moments provides information on the strength of 5*f* ligand hybridization, and consequently the delocalization of the 5*f* electrons [87]. The individual values of orbital and spin components, however, contain essential information, and therefore relevant experiments and first-principles electronic structure calculations which independently evaluate orbital and spin moments become an important issue for 5*f* electron compounds. The recently developed x-ray magnetic circular dichroism experimental method combined with several sum rules [74,88] has attracted much attention as a site- and symmetry-selective way to determine M_s and M_l. It should be mention, however, that the reported quantitative results inferred from the XMCD spectra are based on a sum rule analysis of the spin-orbit split spectra of the core levels of uranium. The sum rules enable one to estimate the spin and orbital components of the uranium ions, however, the values of magnetic moments rely on theoretical inputs such as the number of holes in the 5*f* subshell and a value of the dipolar term. In particular, the spin moment is retrieved with a higher relative error. Comparing the XMCD-derived moments with the results of polarized neutron diffraction and first-principles calculations, one usually obtains smaller moments from the XMCD sum rules for uranium compounds [71,85]. A more reliable quantity that can be extracted from the sum rule analysis is the ratio between orbital and spin moments and their relative orientation.

Table 3 lists the calculated spin M_s, orbital M_l, and total M_t magnetic moments (in μ_B) of UTAl (T = Co, Rh, and Pt) as well as the ratio M_l/M_s [86]. Our LSDA results are in good agreement with previous LSDA-based calculations [71,85]. All the LSDA calculations strongly underestimate the orbital moment in the compounds. The inclusion of the orbital polarization (OP) correction in Ref. 84 brings the calculated total U moment in URhAl to 0.60 μ_B, in better agreement with experiment (0.94 μ_B according to Ref. 79) in comparison with the LSDA calculations (Table 3).

Table 3. The experimental and calculated spin M_S, orbital M_l, and total M_t magnetic moments at the uranium site (in μ_B) of UCoAl, URhAl, and UPtAl

Compound	Method	M_S	M_l	M_t	$-M_l/M_S$
UCoAl	LSDA	–0.92	1.09	0.17	1.18
	LSDA + U(OP)	–1.14	2.29	1.15	2.01
	LSDA + U	–1.50	3.47	1.97	2.31
	LSDA [71]	–1.01	1.19	1.18	1.18
	exper. [71]	—	—	—	1.95
URhAl	LSDA	–1.23	1.72	0.49	1.40
	LSDA + U(OP)	–1.40	2.94	1.54	2.10
	LSDA + U	–1.66	3.83	2.17	2.31
	LSDA [71]	–1.22	1.59	0.37	1.30
	LSDA [85]	–1.24	1.63	0.39	1.31
	LSDA + OP [84]	–1.01	1.61	0.60	1.59
	exper. [79]	–1.16	2.10	0.94	1.81
UPtAl	LSDA	–1.63	2.08	0.45	1.28
	LSDA + U(OP)	–1.60	3.32	1.72	2.08
	LSDA + U	–1.85	4.26	2.41	2.30
	LSDA [71]	–1.63	2.06	0.43	1.26
	exper. [71]	—	—	—	2.10

As mentioned, we also carried out energy band structure calculations for the UTAl compounds using a gene-

ralization of the LSDA + U method [73]. In these calculations we used $U = J = 0.5$ eV, which gives $U_{\text{eff}} = 0$ (the LSDA + U(OP) approximation) as well as $U = 2.0$ eV and $J = 0.5$ eV. Figure 12 shows the $5f_{5/2}$ partial density of states in UPtAl calculated in the LSDA, LSDA + U(OP), and LSDA + U approximations. As can be seen from Fig. 12 the LSDA + U(OP) approximation, which takes into account the correlations between spin and orbital magnetic moment directions, strongly affects the relative energy positions of m_j projected $5f$ density of states and substantially improves their orbital magnetic moments (Table 3). The ratio M_l/M_s in the LSDA + U(OP) calculations is equal to 2.01, 2.10, and 2.08 for UCoAl, URhAl, and UPtAl, respectively. The correspondent experimental data are 1.95, 1.81, and 2.10 estimated from the XMCD measurements [71].

The orbital magnetic moments calculated in the LSDA + U approximation with $U = 2.0$ eV and $J = 0.5$ eV are larger than those calculated using $U = J = 0.5$ eV, which leads to slightly overestimated ratio M_l/M_s in comparison with the experimental data (Table 3).

2. XMCD spectra. Figure 13 shows the calculated x-ray isotropic absorption and XMCD spectra in the LSDA, LSDA + U(OP), and LSDA + U approximations for UPtAl [86] together with the experimental data [71]. To calculate the x-ray isotropic absorption $M_{4,5}$ spectra we take into account the background intensity which appears due to the transitions from inner levels to the continuum of unoccupied levels [89].

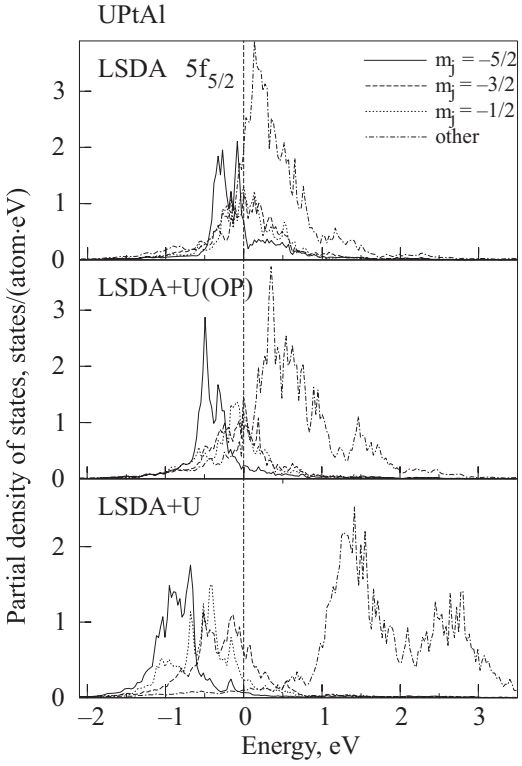

Fig. 12. The partial $5f_{5/2}$ density of states in UPtAl calculated in the LSDA and LSDA + U(OP) approximations [86].

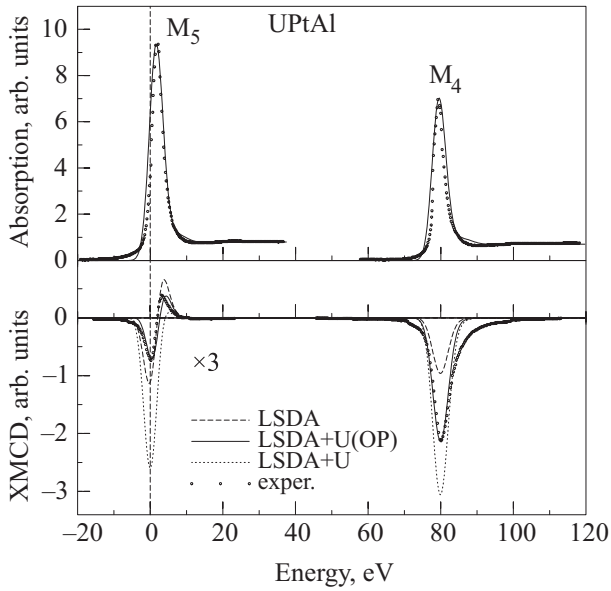

Fig. 13. Isotropic absorption and XMCD spectra of UPtAl at the uranium $M_{4,5}$ edges calculated in the LSDA (dotted lines) and LSDA + U(OP) (solid lines) approximations [86]. Experimental spectra [71] (circles) were measured at 10 K and at magnetic field 2 T (the U M_4 spectrum is shifted by –95 eV to include it in the figure).

Due to underestimation of the orbital magnetic moment the theory produces much smaller intensity of the XMCD spectrum at the M_4 edge in comparison with the experiment in the LSDA calculations and simultaneously gives a larger dichroic signal at the M_5 edge of UPtAl (Fig. 13). On the other hand, the LSDA + U(OP) approximation produces an excellent agreement not only for the value of the magnetic moments but also in the shape and intensity of XMCD spectra both at the M_4 and M_5 edges. The LSDA + U approximation with $U = 2.0$ eV and $J = 0.5$ eV overestimates the negative signal at the M_4 edge due to the overestimation of the U orbital magnetic moment. This approximation also underestimates the positive peak and strongly overestimates the negative one at the M_5 edge (Fig. 13).

In the case of URhAl the LSDA + U(OP) approximation also produces an XMCD spectrum at the M_4 edge in excellent agreement with experiment, but slightly overestimates the value of the positive shoulder at the M_5 edge (Fig. 14). The LSDA + U approximation with $U = 2.0$ eV and $J = 0.5$ eV overestimates the negative signal at the M_4 edge, although, slightly improves the agreement with the experimental spectrum at U M_5 edge (Fig. 14).

The LSDA + U(OP) approximation overestimates and the LSDA + U one strongly overestimates the intensity of XMCD signal at the M_4 edge in UCoAl, probably due to the fact that the measured spontaneous magnetic moment

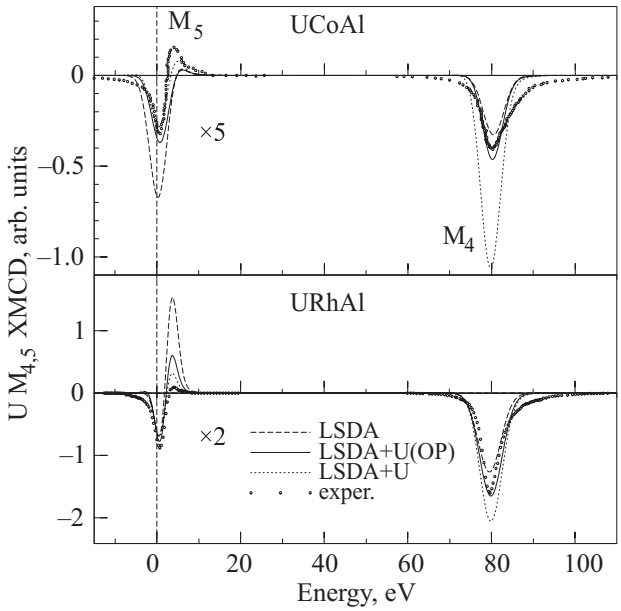

Fig. 14. The XMCD spectra of UCoAl and URhAl at the uranium $M_{4,5}$ edges calculated in the LSDA (dashed lines) and LSDA + U(OP) (solid lines) approximations [86]. Experimental spectra for UCoAl [71] (circles) were measured at magnetic field 7 T. Experimental data for URhAl is from Ref. 70 (the U M_4 spectra are shifted by –95 eV to include them in the figure).

of UCoAl is far from the saturation in the experimentally applied external magnetic field of 7 T [71]. One would expect, therefore, that in a higher magnetic field UCoAl will have larger orbital magnetic moment and, hence, larger dichroism at the M_4 edge. As was the case for URhAl, the LSDA + U calculations with $U = 2.0$ eV and $J = 0.5$ eV give a better description of the positive peak at the M_5 edge in UCoAl (Fig. 14).

The $5f_{7/2}$ states are almost completely empty in all the uranium compounds, therefore the XMCD spectrum of U at the M_5 edge can be roughly represented by the following m_j projected partial density of states [72]: $[N^{7/2}_{-7/2} + N^{7/2}_{-5/2}] - [N^{7/2}_{7/2} + N^{7/2}_{5/2}]$. Thus the shape of M_5 XMCD spectrum consists of two peaks of opposite sign: a negative peak at lower energy and a positive peak at higher energy. The XMCD spectrum of U at the M_4 edge can be represented by the $-[N^{5/2}_{3/2} + N^{5/2}_{5/2}]$ DOS's, [72] thus it consists of a single negative peak.

In UCoAl (above the metamagnetic transition) the dichroic line at the M_5 edge has an asymmetric s shape with two peaks: a stronger negative peak and a weaker positive peak. The shape of the M_5 XMCD spectrum strongly depends on the value of the external magnetic field, the positive peak is increased relative the negative one upon increasing the external magnetic field from 0.9 to 7 T (see Fig. 2 in Ref. 71). From the qualitative description of the M_5 XMCD spectra in terms of partial

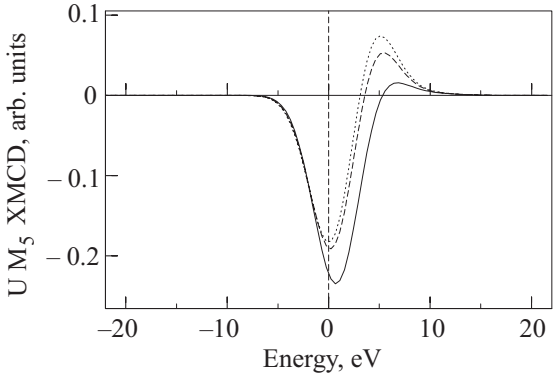

Fig. 15. Uranium M_5 XMCD spectrum of UCoAl calculated in the LSDA + UOP) approximation (full line) and spectra calculated with $[N_{7/2} + N_{5/2}]$ and $[N_{-7/2} + N_{-5/2}]$ DOS's artificially shifted by 10 meV (dashed line) and 20 meV (dotted line) [86].

density of states we can conclude that the shape of the M_5 XMCD spectrum depends on the relative energy positions of the $[N^{7/2}_{7/2} + N^{7/2}_{5/2}]$ and $[N^{7/2}_{-7/2} + N^{7/2}_{-5/2}]$ partial DOS's which depend on the value of crystal field and Zeeman splittings of the $5f_{7/2}$ electronic states [72]. Upon increasing of the external magnetic field the Zeeman splitting is increased, leading to larger separations between the m_j projected partial DOS's. Figure 15 shows uranium M_5 XMCD spectrum of UCoAl calculated in the LSDA + U(OP) approximation and the spectra calculated with $[N^{7/2}_{7/2} + N^{7/2}_{5/2}]$ and $[N^{7/2}_{-7/2} + N^{7/2}_{-5/2}]$ DOS's artificially shifted by 10 and 20 meV. It is clearly seen that model calculations correctly reproduce the experimental tendency in the shape of UCoAl M_5 XMCD spectrum in the external magnetic field.

In conclusion, the LSDA + U approximation with $U = 2.0$ eV and $J = 0.5$ eV overestimates the negative signal at the M_4 edge for all the compounds under the consideration due to the overestimation of the U orbital magnetic moment. This approximation provides poor description of the XMCD spectrum at the M_5 edge in UPtAl, but gives rather good agreement with the experiment in the case of URhAl and UCoAl. One can conclude that the U $5f$ states in UPtAl have more itinerant character than those in URhAl and UCoAl.

2.2. Uranium monochalcogenides

The uranium compounds US, USe, and UTe belong to the class of uranium monochalcogenides that crystallize in the NaCl structure and order ferromagnetically (on the uranium sublattice) at Curie temperatures of 178, 160, and 102 K, respectively (see, e.g., the review [49]). These uranium compounds exhibit several unusual physical phenomena, which are the reason for a continuing on-going interest in these compounds. Despite their relatively simple and highly symmetrical NaCl structure, it has been found that the magnetic ordering on the uranium atoms is

strongly anisotropic [90,91], with the uranium moment favoring a [111] alignment. The magnetic anisotropy in US, e.g., is one of the largest measured in a cubic material, with a magnetic anisotropy constant K_1 of more than $2 \cdot 10^8$ erg/cm^3 [92]. Also the magnetic moment itself is unusual, consisting of an orbital moment that is about twice as large as the spin moment, and of opposite sign [93–95]. A bulk magnetization measurements [91] yields an ordered moment of 1.55 μ_B per unit formula and neutron scattering measurements [96] show a slightly larger value of 1.70 μ_B, which is assigned to the $5f$ magnetic moment. These values are far smaller than that expected for the free ion, indicating that some sort of «solid state effect» takes place with the $5f$ states. From several experimental results (for instance, photoemission [97], electrical resistivity [98], pressure dependence of Curie temperature [99], and specific heat measurements [100,101]), the $5f$ electrons of US are considered to be itinerant.

It has been suggested that uranium monochalcogenides are mixed valence systems [102]. Low-temperature ultrasonic studies on USe and UTe were performed in the context of questioning the possibility of the coexistence of magnetism and intermediate valence behavior [103]. They found a monotonic trend of the Poisson's ratio, which decreases with increasing chalcogenide mass, and is positive in US, negative in USe and UTe. This indicates the possibility of intermediate valence in the last two compounds. Indeed, a negative Poisson's ratio, i.e., a negative C_{12} elastic constant, is quite common for intermediate valence systems, and its occurrence seems to be due to an anomalously low value of the bulk modulus. A negative C_{12} means that it costs more energy to distort the crystal from cubic to tetragonal structure, than to modify the volume. Thus, when uniaxially compressed along a [100] direction, the material will contract in the [010] and [001] directions, trying to maintain a cubic structure. An explanation for a negative C_{12} may be given through a breathing deformability of the actinide ion due to a valence instability [104].

The dependence of the Curie temperatures T_C of US, USe and UTe on hydrostatic pressure up to 13 GPa has been determined in Ref. 105. For USe and UTe, T_C initially increases with applied pressure, passing through maxima at pressure of about 6 and 7 GPa, respectively. For US, T_C decreases monotonically with pressure, which is compatible with pressure-dependent itinerant electron magnetism. Pressure increases the bandwidth and correspondingly decreases the density of states at the Fermi level, which leads to a decrease of T_C. The behavior of USe and UTe is suggestive of localized interacting $5f$ moments undergoing Kondo-type fluctuations, which begin to exceed the magnetic interaction when T_C passes through maximum. A theoretical analysis of these experiments is given in Ref. 106. On the basis of band structure calculations it is argued that the nonmonotonic behavior of T_C under pressure is solely the result of pressure-driven increased $5f$ itineracy.

It must be remarked that the behavior of uranium monochalcogenides cannot be explained entirely by a simple trend of increasing localization with increasing chalcogen mass [48]. Whereas such a trend is evident in the dynamic magnetic response, in the pressure-dependence of the Curie temperatures and in the value of the ordered moment, the behavior of Poisson's ratio and of the Curie temperature is the opposite from what one would naively expect.

There are several band structure calculations of uranium monochalcogenides in literature [95,107–116]. Kraft et al. [110] have performed the LSDA calculation with the spin-orbit interaction in a second variational treatment for ferromagnetic uranium monochalcogenides (US, USe, and UTe) using the ASW method, and have shown that the magnitude of the calculated orbital magnetic moment M_l is larger than that of spin moment M_s and they couple in an antiparallel way to each other. However, the magnitude of the total magnetic moment ($M_s + M_l$) is too small compared to the experimental data, indicating that the calculated M_l is not large enough.

The optical and MO spectra of uranium monochalcogenides have been investigated theoretically in Refs. 107, 108, 110, 112. These theoretical spectra are all computed from first principles, using Kubo linear-response theory, but it appears that there are large differences among them. Cooper and co-worker [109] find good agreement with experiment for the real part of the diagonal conductivity ($\sigma_{xx}^{(1)}$) of UTe, but the much more complicated off-diagonal conductivity ($\sigma_{xy}^{(2)}$) of US and UTe is about 4 times larger than experiment and also the shape of their spectrum is different from the experimental one. Halilov and Kulatov [107] also find an off-diagonal conductivity which is much larger than the experimental one, but they additionally obtain a diagonal conductivity $\sigma_{xx}^{(1)}$ that differs substantially from experiment. Gasche [108] find a Kerr rotation spectrum of US that is quite different from experiment, and subsequently consider the effect of an orbital polarization term to improve the *ab initio* Kerr spectra. Kraft et al. [110] obtained for US, USe, and UTe reasonable agreement with experiment for the absolute value of the Kerr spectra. However, the shape of the Kerr spectra is not reproduced by LSDA theory, since the theoretical spectra exhibit a double-peak structure, but experimental spectra have only a one-peak structure. The LSDA + U calculations presented in Ref. 112 take into account the strong Coulomb correlations among the $5f$ orbitals and are greatly improve the agreement between theory and experiment for all three materials. This finding appears to be consistent with the quasilocalized nature of the $5f$ electrons in these compounds.

3. Band structure. All the three chalcogenides, namely, US, USe, and UTe crystallize in the NaCl type structure (B1) with space group symmetry *Fm*3*m*. The uranium atom is positioned at (0,0,0) and chalcogen at (1/2,1/2,1/2).

The LSDA energy band structure of US (Fig. 16) can be subdivided into three regions separated by energy gaps. The bands in the lowest region around –15 eV have mostly S *s* character with a small amount of U *sp* character mixed in. The next six energy bands are S *p* bands separated from the *s* bands by an energy gap of about 6 eV. The width of the S *p* band is about 4 eV. U 6*d* bands are broad and extend between –2.5 and 10 eV. The sharp peaks in the DOS just below and above the Fermi energy are due to $5f_{5/2}$ and $5f_{7/2}$ states, respectively. Figure 16 also shows the energy bands and total density of states of US in the LSDA + *U* approximation [116]. The Coulomb repulsion splits partially occupied U $5f_{5/2}$ states and the LSDA + *U* calculations give a solution with three localized 5*f* electrons in US. U 5*f* states just above the Fermi level are formed by the remaining $5f_{5/2}$ states whereas the peak of $5f_{7/2}$ states is pushed about 1 eV upward from its LSDA position.

Table 4 presents the comparison between calculated and experimental magnetic moments in uranium monochalcogenides. For comparison, we list also the results of previous band structure calculations. Our LSDA results obtained by fully relativistic spin-polarized LMTO method are in good agreement with the ASW Kraft et al. results [110]. The LSDA calculations for ferromagnetic uranium monochalcogenides (US, USe, and UTe) give the magnitude of the total magnetic moment M_t too small compared to the experimental data, indicating that the calculated M_l is not large enough.

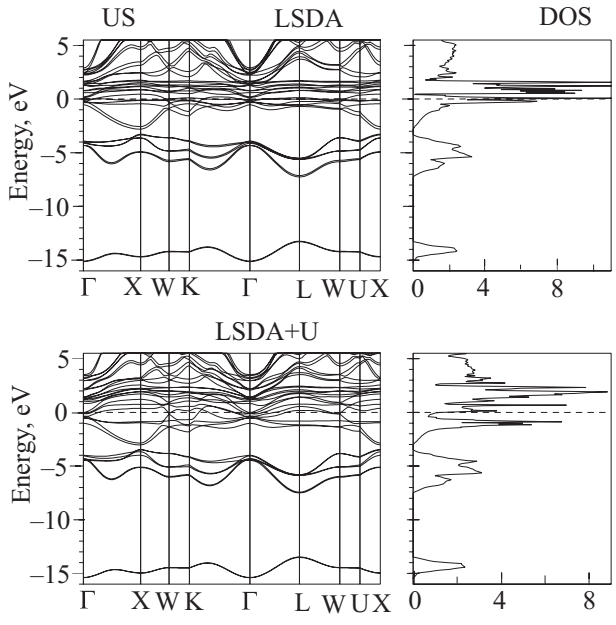

Fig. 16. Self-consistent fully relativistic energy band structure and total DOS (in states/(unit cell·eV)) of US calculated within the LSDA and LSDA + *U* approximations with *U* = 2 eV and *J* = 0.5 eV [116].

Table 4. The experimental and calculated spin M_s, orbital M_l, and total M_t magnetic moments at uranium site (in μ_B) of US, USe, and UTe [116]

Compound	Method	M_s	M_l	M_t	$-M_l/M_s$
US	LSDA	–1.53	2.14	0.60	1.41
	LSDA + *U*(OP)	–1.48	3.21	1.72	2.17
	LSDA + *U*	–1.35	3.42	2.07	2.53
	LSDA [110]	–1.6	2.5	0.9	1.6
	LSDA + OP [95]	–2.1	3.2	1.1	1.5
	OP scaled HF [117]	–1.51	3.12	1.61	2.07
	HF(TB) [114]	– 1.49	3.19	1.70	2.14
	exper. [96]	–1.3	3.0	1.7	2.3
	exper. [91]	—	—	1.55	—
USe	LSDA	–1.75	2.54	0.79	1.45
	LSDA + *U*(OP)	–1.65	3.65	2.00	2.21
	LSDA + *U*	–1.96	4.61	2.65	2.35
	LSDA [110]	–1.8	2.8	1.0	1.5
	LSDA + OP [95]	–2.4	3.4	1.0	1.4
	exper. [96]	—	—	2.0	—
	exper. [91]	—	—	1.8	—
UTe	LSDA	–2.12	3.12	1.00	1.47
	LSDA + *U*(OP)	–1.91	4.09	2.17	2.14
	LSDA + *U*	–2.13	4.95	2.81	2.32
	LSDA [110]	–2.2	3.4	1.2	1.5
	LSDA + OP [95]	–2.6	3.4	0.8	1.3
	exper. [118]	–1.57	3.48	1.91	2.21
	exper. [96]	—	—	2.2	—
	exper. [91]	—	—	1.9	—

It is a well-known fact, however, that the LSDA calculations fail to produce the correct value of the orbital moment of uranium compounds [95,117,119–121]. In LSDA, the Kohn–Sham equation is described by a local potential including the spin-dependent electron density. The electric current, which describes M_l, is, however, not included. This means, that although M_s is self-consistently determined in LSDA, there is no framework to simultaneously determine M_l self-consistently.

Using the LSDA + OP method Brooks [95] obtained larger magnitude of M_l and improvement in M_t. However, they have stated that the individual magnitudes of M_s and M_l are considered to be too large from the analysis of the magnetic form factor and the ratio M_l/M_s is still

far from the experimental value for all the three uranium monochalcogenides (Table 4).

Table 4 presents the calculated magnetic moments in uranium monochalcogenides using a generalization of the LSDA + U method [73,122]. In this calculations we used $U = 2.0$ eV and $J = 0.5$ eV. Table 4 presents also the LSDA + U calculated magnetic moments with $U = J = 0.5$ eV (the LSDA + U(OP) approximation).

Figure 17 shows $5f_{5/2}$ partial density of states in US calculated within the LSDA, LSDA + U(OP) and LSDA + U approximations [116]. The LSDA + U(OP) approximation strongly affects the relative energy positions of m_j projected $5f$ density of states and substantially improve their orbital magnetic moments (Table 4). For example, the ratio M_l/M_s in the LSDA + U(OP) calculations is equal to –2.17 and –2.14 for US and UTe, respectively. The corresponding experimental value are –2.3 for US from the neutron measurements [96] and –2.21 for UTe from the magnetic Compton profile measurements [118].

The $5f$ spin M_s and orbital M_l magnetic moments in US have been also calculated in Ref. 114 on the basis of the HF approximation for an extended Hubbard model. The tight-binding model includes the intra-atomic $5f$–$5f$ multipole interaction and the SOI in the $5f$ state. The parameters involved in the model were determined by fitting with the energy of Bloch electrons in the paramagnetic state obtained in the LDA band structure calculation. The calculated ratio of the moments M_l/M_s of –2.14 and M_l of –3.19 μ_B are in good agreement with available experimental results (Table 4).

We should mention that the results of the LSDA + U(OP) calculations are in close agreement with the results obtained using the HF approximation for an extended Hubbard model [114] (Table 4). Both the approximations take into account the SOI and the intra-atomic $5f$–$5f$ Coulomb interaction in Hubbard model. The small differences in magnetic moments are due to slightly different values of U_{eff}. In our calculations we used $U = J = 0.5$ eV, which gives $U_{\text{eff}} = 0$. Authors of Ref. 114 used $U = 0.76$ eV and $J = 0.5$ eV, which gives $U_{\text{eff}} = 0.26$ eV. Besides, there are some small differences in F^2, F^4 and F^6 Slater integrals in two the calculations.

Figure 17 also shows the m_j projected $5f_{5/2}$ density of states in US calculated in the LSDA + U approximation with $U = 2.0$ eV and $J = 0.5$ eV [116]. The corresponding partial DOS's for USe and UTe are presented in Fig. 18. The degree of localization of occupied $5f_{5/2}$ states is increasing going from US to UTe. In US the $5f_{5/2}$ states with $m_j = -5/2$ is strongly hybridized with other occupied states, while the hybridization in USe and particularly in UTe almost vanishes. The $5f_{5/2}$ states with $m_j = -5/2$ are responsible for the narrow single peak in UTe (Fig. 18). The orbital magnetic moments calculated in the LSDA + U approximation are larger than calculated in the LSDA + U(OP) approximation, which leads to slightly overestimated ratio M_l/M_s in comparison with the experimental data for the LSDA + U calculations (Table 4).

4. XMCD spectra. Figure 19 shows the XMCD spectra of US, USe, and UTe at the uranium $M_{4,5}$ edges calculated within the LSDA and LSDA + U approximations [116]. It is clearly seen that the LSDA calculations give

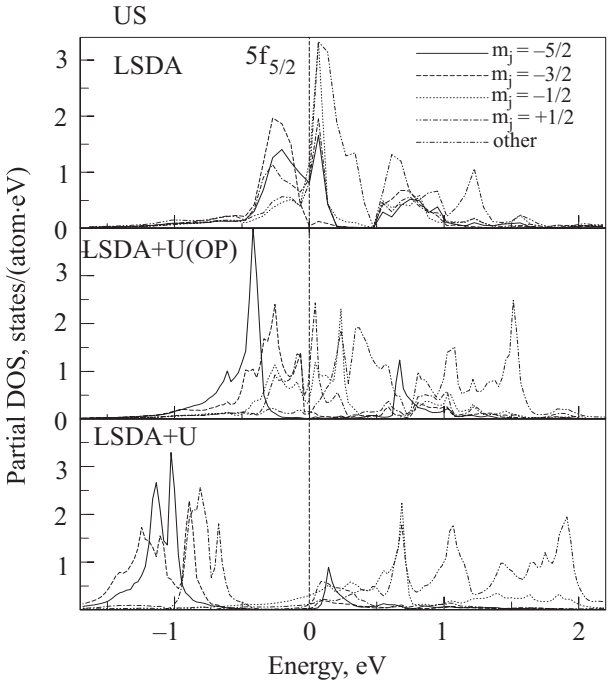

Fig. 17. The partial $5f_{5/2}$ and $5f_{7/2}$ density of states within US, USe, and UTe calculated in the LSDA and LSDA + U approximations [116].

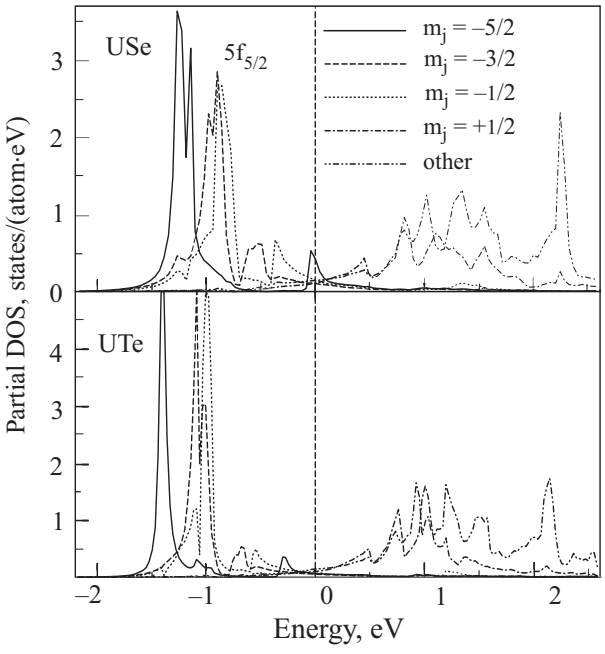

Fig. 18. The partial $5f_{5/2}$ density of states in USe and UTe calculated within the LSDA + U approximation [116].

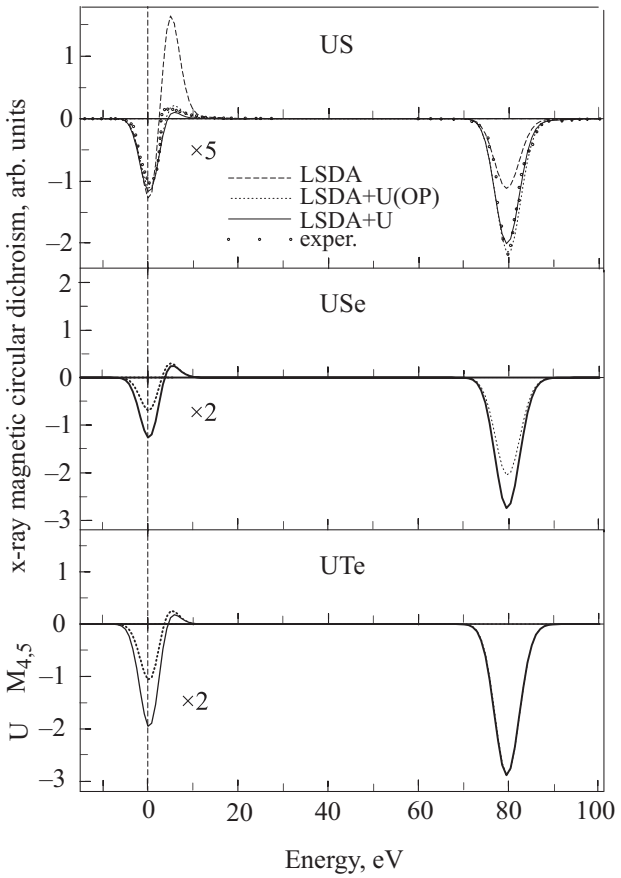

Fig. 19. The XMCD spectra of US, USe, and UTe at the uranium $M_{4,5}$ edges calculated within the LSDA (dashed lines), LSDA + U(OP) (dotted lines), and LSDA + U (solid lines) approximations [116]. Experimental spectra of US [71] (circles) were measured at magnetic field 2 T (the U M_4 spectra are shifted by –95 eV to include them in the figure).

inappropriate results. The major discrepancy between the LSDA calculated and experimental XMCD spectra is the size of the M_4 XMCD peak. The LSDA underestimates the integral intensity of the XMCD at M_4 edge. As the integrated XMCD signal is proportional to the orbital moment [74] this discrepancy could be related to an underestimation of the orbital moment by LSDA-based computational methods (Table 4). On the other hand, the LSDA + U approximation produces good agreement with the experimentally measured intensity for the M_4 XMCD spectrum. In the case of the M_5 XMCD spectrum, the LSDA strongly overestimates the value of the positive peak. The LSDA + U(OP) approximation gives a good agreement in the shape and intensity of the XMCD spectrum at the M_5 edge.

The behavior of the 5f electrons ranges from nearly delocalized to almost localized: US is considered to be nearly itinerant [123], while UTe is considered to be quasilocalized [124]. So the failure of LSDA description of XMCD spectra in US comes as a surprise, because, if the 5f electrons are itinerant, one would expect the delocalized LSDA approach to be applicable. However, as the integrated XMCD signal is proportional to the orbital moment [74] this discrepancy could be related to an underestimation of the orbital moment by LSDA-based computational methods.

It is interesting to note, that the LSDA + U(OP) and LSDA + U calculations give similar results for XMCD spectrum at the M_5 edge in the case of US and became relatively more different going through USe and UTe, probably, reflecting the increase of degree of localization of 5f electrons. Besides, the relative intensity of the M_5 and M_4 XMCD spectra is strongly increased going from US to UTe. The experimental measurements of the XMCD spectra in USe and UTe are highly desired.

2.3. Heavy-fermion compounds

2.3.1. UPt_3

UPt_3 is a well known heavy-fermion system [125,126]. The Sommerfeld coefficient of the linear low-temperature specific heat is strongly enhanced, i.e., γ = = 420 mJ/(mol U·K^2). Strong electron-electron correlations are also manifest in a $T^3 \log T$ term in the low-temperature specific heat, which is believed to be due to spin fluctuations. At low temperature UPt_3 is a superconductor, with a T_C of 0.54 K [59]. UPt_3 is the archetype of a heavy-fermion system. It has the qualitative properties of a Fermi liquid, but the magnitude of the effective masses, reflected in the specific heat and magnetic susceptibility, is very much larger than the free-electron value. The heaviness of the electrons is generally attributed to electron correlations which come from the strong Coulomb interactions among the localized 5f electrons on the U sites.

UPt_3 has attracted a great deal of interest from band-structure theorists [127–131], particularly when it became clear that reliable experimental information on the Fermi surface could be obtained by measurements of the de Haas–van Alphen (dHvA) effect [132,134]. These experiments unambiguously confirm that UPt_3 has to be regarded as a strongly correlated Fermi liquid. Although a detailed picture of the low-temperature phase of UPt_3 has emerged, a comprehensive theoretical picture of the heavy quasiparticles is still missing.

It has been considered a success of the LSDA that the dHvA frequencies could be related to extremal orbits on the Fermi surface obtained by band-structure calculations which treat the U 5f states as itinerant. There are good reasons that standard band-structure calculations reproduce well the complex topology of the Fermi surface in UPt_3. In great contrast, however, no such agreement is found for the measured cyclotron masses. The calculated energy bands are too broad for explaining the effective masses: dHvA masses are by a factor of order 20 bigger than the band masses m_b obtained from the LSDA calcu-

lations [129–131]. This is of course the defining characteristic of a heavy-fermion compound and is due to the strong electron-electron correlations not included in the band-structure calculations. It is interesting that even in the presence of such strong correlations, there is no evidence of any breakdown of Fermi-liquid theory. The standard Lifshitz–Kosevich formula for the field and temperature dependence of the amplitude of quantum oscillations is perfectly verified down to 10 mK and up to 18 T [59].

UPt_3 shows a static antiferromagnetic order below about $T_N = 5$ K with a very small staggered moment of order 0.01 μ_B/U atom. This ordering was first noticed in muon spin relaxation measurements by Heffner et al. [135] and was soon confirmed by neutron scattering [136]. The magnetic order is collinear and commensurate with the crystal lattice, with a moment aligned in the basal plane. It corresponds to antiferromagnetic coupling within planes and ferromagnetic coupling between planes. All aspects of this ordering were reproduced by later neutron studies on a different crystal [137,138] and by magnetic x-ray scattering [139]. The moment at lower temperatures grows to a maximum magnitude of 0.02–0.03 μ_B/U atom.

1. Band structure. UPt_3 crystallizes in the $MgCd_3$-type structure. The uranium atoms form a closed-packed hexagonal structure with the platinum atoms bisecting the planar bonds. There are two formula units per unit cell. The compound belongs to the space group $P6_3/mmc$ and the point group D_{6h}. The lattice parameters are a = = 5.753 Å and c/a = 4.898. The nearest U–U distance is between atoms in adjacent layers, equal to 4.132 Å, and the conductivity is greatest along the c axis.

The fully relativistic spin-polarized LSDA energy band structure and total DOS of the ferromagnetic UPt_3 compound is shown in Fig. 20 [140]. The occupied part of the valence band is formed predominantly by Pt 5d states. The characteristic feature of the LSDA band structure is a narrow peak of U 5$f_{5/2}$ states situated just at the Fermi level (E_F) 1.0 eV above the top of Pt 5d states. U 5$f_{7/2}$ states are split off by strong SO coupling and form another narrow peak 1 eV above E_F.

Figure 20 also shows the band structure of UPt_3 calculated in the LSDA + U approximation with U = 2.0 eV and J = 0.5 eV [140]. The Coulomb repulsion splits partially occupied U 5$f_{5/2}$ states and the LSDA + U calculations give a solution with two localized 5f electrons. These localized 5f states are situated above the top of Pt 5d and form a rather narrow peak at 0.2 eV below E_F. The position of the peak agrees well with the results of recent resonant photo-emission spectroscopy (PES) [141] and angular resolved PES (ARPES) [142] measurements. U 5f states just above the Fermi level are formed by the remaining 5$f_{5/2}$ states whereas the peak from the 5$f_{7/2}$

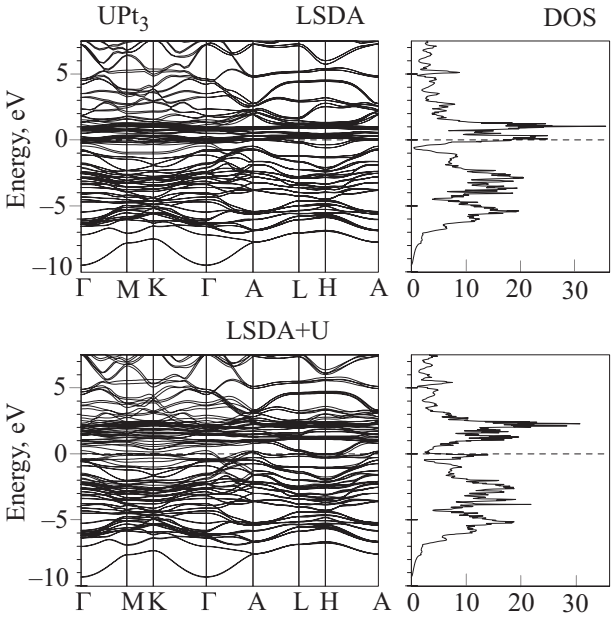

Fig. 20. The self-consistent fully relativistic, spin-polarized energy band structure and total DOS (in states/(unit cell·eV)) of UPt_3 calculated in the LSDA and LSDA + U approximations [140].

states is pushed from its LSDA position at 1 eV above E_F to 2.3 eV.

An orbital resolved DOS corresponding to the orbitals with the largest occupation numbers is shown in Fig. 21 for UPt_3 and for UPd_3 as a reference material. Two peaks at –1.0 to –0.5 eV in UPd_3 are formed by 5$f_{5/2}$ states with $m_j = -5/2$ and $m_j = -3/2$. Their occupation numbers are $n_{5/2} = 0.988$ and $n_{3/2} = 0.982$, which corresponds to an f^2 configuration of the U ion [73]. The corresponding

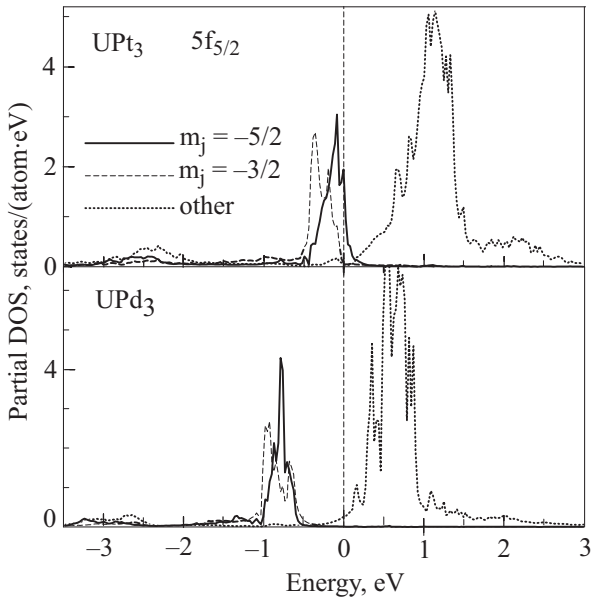

Fig. 21. The partial 5$f_{5/2}$ density of states in UPt_3 and UPd_3 calculated in the LSDA + U approximation.

states in UPt_3 are situated in –0.5 to 0.2 eV energy range, very close to the Fermi level and partially occupied. Such a different energy position of occupied $5f_{5/2}$ states in UPd_3 and UPt_3 can be explained by the larger spatial extent of Pt 5*d* wave functions as compared to the Pd 4*d* states which causes a proportional increase of the part of *f* electron density at U site provided by the «tails» of *d* states. The screening of the localized U $5f$ states by this delocalized density becomes stronger in UPt_3 and their occupied $5f_{5/2}$ states shift to higher energy [73].

The above-mentioned self-consistent LSDA + *U* solutions for UPd_3 and UPt_3 are magnetic with a rather large U magnetic moment. This is contrary to the experimental data which show that the ordered magnetic moment is only 0.01 μ_B and 0.02–0.03 μ_B per U atom in UPd_3 and UPt_3, respectively [137–139,143]. This extremely small U magnetic moment is explained by the fact that according to the crystalline electric field (CEF) level scheme derived from neutron scattering experiments, the lowest CEF level of U^{4+} ion in both compounds is a singlet [139,144] which leads to a nonmagnetic ground state for these compounds. The LSDA + *U* is still a one electron approximation and can not fully account for the subtle many-body effects responsible for the small value of the U magnetic moment in the UPd_3 and UPt_3. It tries to obey the Hund's rules in the only way it is allowed to, i.e., by producing a magnetic solution. A possible way to overcome this discrepancy between the calculations and the experiment is to force a nonmagnetic ground state in the LSDA + *U* calculations as it was done by H. Harima et al. in Refs. 143, 145. We have verified, however, that this leads to an increase of the total energy as compared to magnetic states obtained in the calculations.

It should be mentioned that depending on the starting conditions another self-consistent LSDA + *U* solution very close in total energy can obtained for UPd_3 as well as for UPt_3. This solution also results in two localized U $5f$ electrons but in this case the occupied states are $|5/2,-5/2\rangle$ and $|5/2,-1/2\rangle$ (here we used the notation $|j,m_j\rangle$ for the state with the total momentum j and its projection m_j) [140]. The existence of two almost degenerate solutions can be understood if one compares the matrix elements of Coulomb interaction U_{m_j,m'_j} calculated between $5f_{5/2}$ states with different m_j [73]. The matrix elements $U_{5/2,3/2}$ and $U_{5/2,1/2}$ are equal and the energy difference is caused not by the on-site Coulomb interaction but instead by a difference in the hybridization between U $5f_{5/2}$ and conduction electrons. Also, the lowest unoccupied $5f$ state, which is either $|5/2,-1/2\rangle$ or $|5/2,-3/2\rangle$, feels the same Coulomb repulsion of the localized electrons. Total energy calculations, however, show that lower energy solution is associated with $|5/2,-3/2\rangle$ occupied states.

2. XMCD spectra. As we mentioned above, for the $5f^2$ configuration in UPt_3 we have two solutions with close total energies, in the first case the $5f_{5/2}$ states with $m_j = -5/2$ and $-3/2$ are occupied, in the second case the occupied states are $m_j = -5/2$ and $-1/2$. In the first case the dipole allowed transitions for left circularly polarized light, $\lambda = +1$ are $-3/2 \to -1/2$, $-1/2 \to +1/2$, $+1/2 \to +3/2$, and $+3/2 \to +5/2$ and for right circularly polarization $\lambda = -1$: $+1/2 \to -1/2$ and $+3/2 \to +1/2$. The transitions with equal final states $m_j = -1/2$ and $m_j = +1/2$ mostly cancel each other and the XMCD spectrum of U at the M_4 edge ($I = \mu^- - \mu^+$) can be roughly represented by $-[N^{5/2}_{3/2} + N^{5/2}_{5/2}]$ partial density of states [72]. In the second case, however, the dipole allowed transitions for $\lambda = +1$ are $-1/2 \to +1/2$, $+1/2 \to +3/2$, and $+3/2 \to +5/2$ and for $\lambda = -1$: $-1/2 \to -3/2$ and $+3/2 \to +1/2$. Therefore U M_4 XMCD spectrum can be roughly represented by $N^{5/2}_{1/2} - [N^{5/2}_{3/2} + N^{5/2}_{5/2}]$ partial density of states. One would expect therefore smaller intensity of dichroic signal at the M_4 edge for the second case in comparison with the first one due to the compensation between $N_{1/2}$ and $[N_{3/2} + N_{5/2}]$ partial density of states in the second case.

The $5f_{7/2}$ states are almost completely empty in all the uranium compounds. Therefore the XMCD spectrum of U at the M_5 edge can be roughly represented by the m_j projected partial density of states [72]: $[N^{7/2}_{-7/2} + N^{7/2}_{-5/2}] - [N^{7/2}_{7/2} + N^{7/2}_{5/2}]$. As a result, the shape of the M_5 XMCD spectrum consists of two peaks of an opposite sign: a negative peak at lower energy and a positive peak at higher energy. As the separation of the peaks is smaller than the typical lifetime broadening, the peaks cancel each other to a large extent, thus leading to a rather small signal.

Although we neglect cross terms in the transition matrix elements and there is no full compensation between transitions with equal final states due to difference in the angular matrix elements, such a simple representation qualitatively reproduces all the peculiarities of the experimentally measured XMCD spectra in UPt_3. It gives a simple, slightly asymmetric negative peak at the M_4 edge and an *s* shaped two-peak structure at the M_5 edge (Fig. 22). It also correctly gives the dichroism at the M_4 edge of approximately one order of magnitude larger than at the M_5 one. The spectrum at the M_4 edge is very sensitive to the character of the occupied $5f_{5/2}$ states and has larger intensity for the solution with occupied $|5/2,-3/2\rangle$ states.

Figure 23 shows the calculated XMCD spectra in the LSDA and LSDA + *U* approximations for UPt_3 [140] together with the experimental data [65]. The intrinsic broadening mechanisms have been accounted for by folding the XMCD spectra with a Lorentzian of 3.2 and 3.4 eV for M_5 and M_4 spectra, respectively. The overall shapes of the calculated and experimental uranium $M_{4,5}$ XMCD spectra correspond well to each other. The major discrepancy between the calculated and experimental XMCD spectra is the size of the M_4 XMCD peak. The LSDA the-

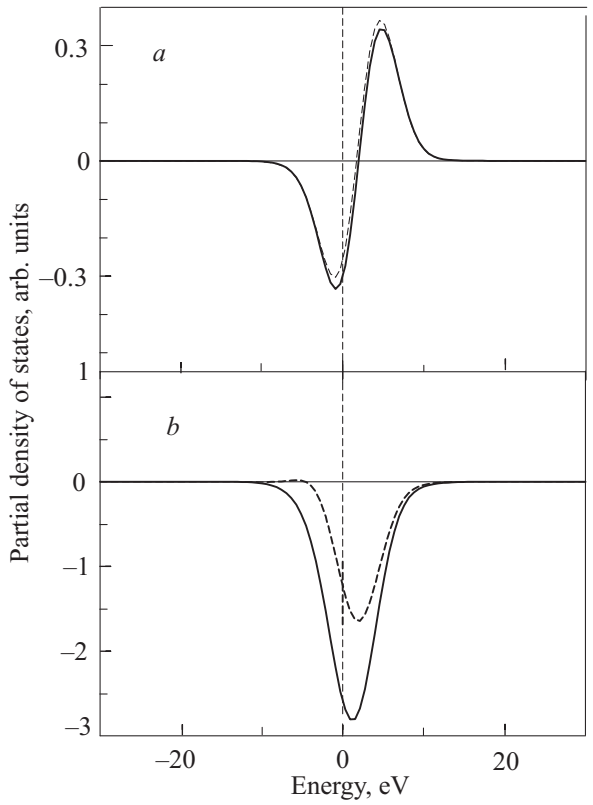

Fig. 22. The model representation of the M_5 (*a*) and M_4 (*b*) XMCD of UPt_3 for two solutions with $|5/2,-3/2\rangle$ occupied states (full lines) and $|5/2,-1/2\rangle$ ones (dashed lines): (*a*) presents the partial densities of states $[N^{7/2}_{-7/2} + N^{7/2}_{-5/2}] - [N^{7/2}_{7/2} + N^{7/2}_{5/2}]$; (*b*) $-[N^{5/2}_{3/2} + N^{5/2}_{5/2}]$ (full line) and $N^{5/2}_{1/2} - [N^{5/2}_{3/2} + N^{5/2}_{5/2}]$ (dashed lines) [140] (see the explanation in the text).

ory produces a much smaller intensity for the XMCD spectrum at M_4 edge in comparison with the experiment and simultaneously gives a larger dichroic signal at M_5 edge. On the other hand, the LSDA + U approximation produces excellent agreement in the shape and intensity of XMCD spectra both at the M_4 and M_5 edges for the solution with the $|5/2,-3/2\rangle$ state occupation. The solution with $|5/2,-1/2\rangle$ occupation produces a smaller intensity for the XMCD spectrum at the M_4 edge in comparison with the experiment. This observation is consistent with the total energy calculations which show that the lowest energy state has the solution with $|5/2,-3/2\rangle$ states occupied.

The LSDA + U(OP) approximation, which describes the correlations between spin and orbital magnetic moment directions ($U_{\text{eff}} = 0$) gives a correct value of the XMCD spectrum at U M_4 edge, but slightly overestimates the positive peak and underestimates the negative one at the M_5 edge (not shown).

Figure 23 shows also the XMCD spectra in UPd_3 calculated using the LSDA + U approximation for the solution with occupied $|5/2,-3/2\rangle$ states [140]. The XMCD

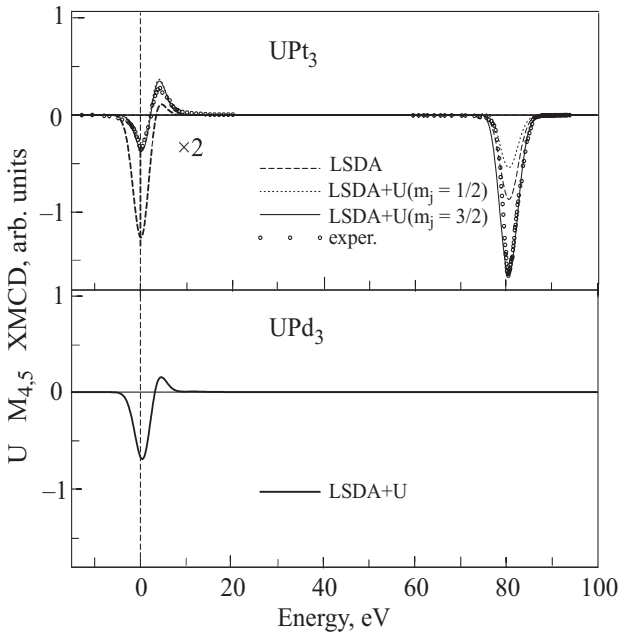

Fig. 23. The XMCD spectra of UPt_3 and UPd_3 at the uranium $M_{4,5}$ edges calculated in the LSDA, LSDA + U(OP), and LSDA + U approximations [140]. Experimental spectra for UPt_3 [65] (circles) were measured in a magnetic field of 5 T at 20 K (the U M_4 spectra are shifted by –95 eV to include them in the figure).

spectra of UPd_3 and UPt_3 are very similar, except, the positive peak at the M_5 edge is slightly less pronounced in UPd_3 than in UPt_3. Experimental measurements of XMCD spectra in UPd_3 are highly desired.

2.3.2. URu_2Si_2

The heavy-fermion superconductor URu_2Si_2 has attracted continuous attention in the last decade for its unusual ground-state properties. URu_2Si_2 crystallizes in the body-centered tetragonal $ThCr_2Si_2$ structure with lattice constant $a = 4.126$ Å and $c/a = 2.319$. At $T_N = 17.5$ K the system undergoes an antiferromagnetic phase transition which is accompanied by a sharp peak in the specific heat [146,147] and thermal expansion [148]. A second transition occurs at $T_C = 1.2$ K and indicates the onset of superconductivity which coexists with the antiferromagnetic order. Neutron-scattering measurements [149,150] revealed a simple antiferromagnetic structure with a tiny ordered moment of $(0.04 \pm 0.01)\ \mu_B$/U atom, oriented along the c axis of the tetragonal crystal structure. The formation of an energy gap in the magnetic excitation spectrum is reflected by an exponential temperature dependence of the specific heat [146,147], the thermal expansion [148] and the NMR and nuclear quadruple-resonance NQR relaxation rates [151] in the ordered state. Electrical resistivity [152] and point-contact spectroscopy measurements [153] show a similar energy gap, indicating a strong scattering of the conduction electrons by

the magnetic excitations. Magnetization measurements in high magnetic fields [154,155] show a suppression of the heavy-fermion state in three consecutive steps at 35.8, 37.3, and 39.4 T for fields along the easy axis ($B||c$). These transitions have been confirmed in high-field measurements of the magnetoresistance and Hall coefficient [156].

There are several LSDA band structure calculations of URu_2Si_2 in the literature [157–160]. A self-consistent calculation of electronic band structure for antiferromagnetically ordered URu_2Si_2 was performed using an all-electron fully relativistic spin-polarized LAPW method by Yamagami and Hamada [160]. They obtained a magnetic moment at the uranium site with a tiny value of 0.09 μ_B due to cancellation between the spin and the orbital moments. The theoretically calculated frequencies as functions of the direction of applied magnetic field are in reasonable agreement with the dHvA frequencies measured by Ohkuni et al. [161].

The electronic band structure and the Fermi surface of paramagnetic URu_2Si_2 have been studied also with high-resolution angle-resolved photoemission spectroscopy in Ref. 162. It was found that Ru 4*d* bands form the main body of the valence band and exhibit a remarkable energy dispersion in qualitatively good agreement with the band structure calculations. In addition to the dispersive Ru 4*d* bands, a less dispersive band was found near the Fermi level, which can be assigned to the U 5*f*–Ru 4*d* hybridized band.

1. Band structure. Self-consistent LSDA calculations produce an antiferromagnetic ground state in URu_2Si_2 [140] in agreement with the experimental observation [148]. The spin moment at the U site is obtained as –0.04 μ_B, the orbital moment is 0.09 μ_B. The total magnetic moment is, therefore, 0.05 μ_B. This is in a good agreement with the magnetic moment of 0.04 μ_B observed by neutron-scattering measurements [149,150]. The fully relativistic spin-polarized LSDA energy band structure and total DOS of the antiferromagnetic URu_2Si_2 is shown in Fig. 24. Figure 25 shows the LSDA partial density of states of URu_2Si_2 [140]. Si 3*s* states are located mostly at the bottom of the valence band in the –11 to –8 eV energy interval. Si 2*p* states hybridize strongly with Ru 4*d*, U 6*d* and U 5*f* valence states and occupy a wide energy range from –6.5 to 11 eV. There is an energy gap of around 0.5 eV between Si 3*s* and 3*p* states. Ru 4*d* states are situated below and above Fermi level in the –6.5 to 3.5 eV range. The Fermi level falls in the local minimum of Ru 4*d* states (Fig. 25). U 6*d* states are strongly hybridized with Ru 4*d* as well as Si 3*p* and even Si 3*s* states. A narrow peak of U $5f_{5/2}$ states situated just at the Fermi level E_F. U $5f_{7/2}$ states are split off by strong SO coupling and form another narrow peak 1.2 eV above E_F. Because U 5*f* states are situated at the local minimum of Ru 4*d* states there is rather week U 5*f*–Ru 4*d* hybridization.

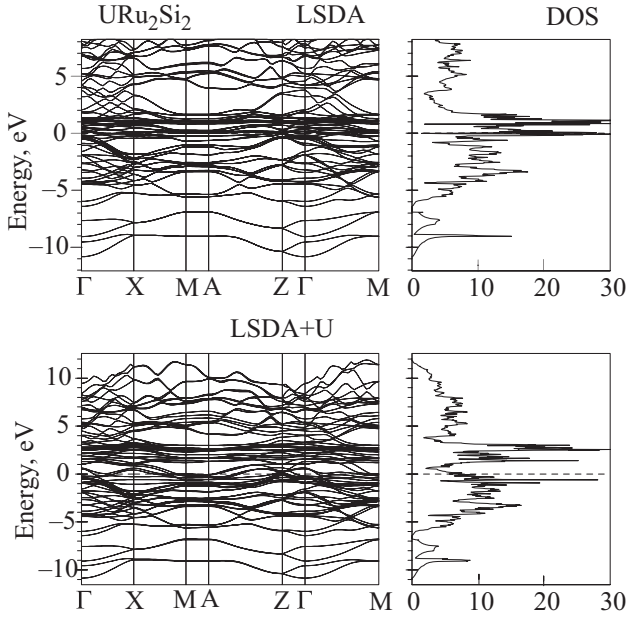

Fig. 24. The self-consistent fully relativistic, spin-polarized energy band structure and total DOS (in states/(unit cell·eV)) of URu_2Si_2 calculated in the LSDA and LSDA + U approximations [140].

Figure 24 also shows the band structure of URu_2Si_2 calculated in the LSDA + U approximation with U = 2.0 eV and J = 0.5 eV [140]. The Coulomb repulsion U_{eff} strongly influences the electronic structure of URu_2Si_2. The occupied on-site 5*f* energies are shifted downward by $U_{\text{eff}}/2$ and the unoccupied levels are shifted upwards by this amount. As a result both the occupied and empty U 5*f* states move to a position with large Ru 4*d* DOS and the degree of U 5*f*–Ru 4*d* hybridization increases going from the LSDA to the LSDA + U solution. In the Hartree–Fock like LSDA + U solution with nonspherical correction to Coulomb matrix elements, three particular $5f_{5/2}$ states ($m_j = -5/2$, $-3/2$, and $-1/2$) are occupied which leads to large spin (–2.01 μ_B) and orbital (4.78 μ_B) magnetic moments for the U atom. U 5*f* states just above the Fermi level are formed by the remaining $5f_{5/2}$ states whereas the peak of $5f_{7/2}$ states is pushed from its LSDA position above E_F by 2.8 eV.

2. XMCD spectra. Figure 26 shows the calculated x-ray isotropic absorption and XMCD spectra in the LSDA and LSDA + U approximations for URu_2Si_2 [140] together with the experimental data [69]. To calculate the x-ray isotropic absorption $M_{4,5}$ spectra we take into account the background intensity which appears due to transitions from occupied levels to the continuum of unoccupied levels [89].

The theory [140] produces a much smaller intensity of the XMCD spectrum at the M_4 edge in comparison with the experiment in the LSDA calculations. It also gives a larger positive peak and a two times smaller negative

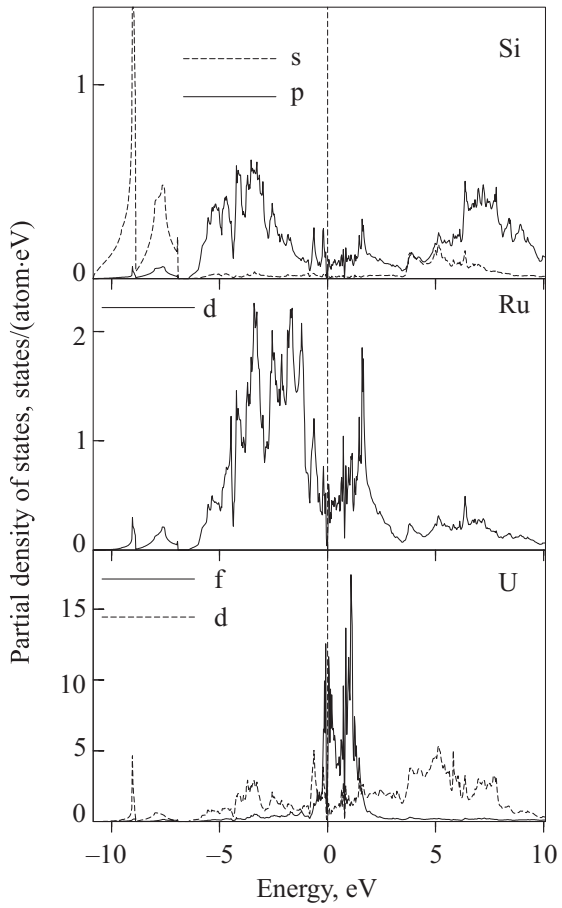

Fig. 25. The partial density of states in URu_2Si_2 calculated in the LSDA approximation [140] (the 6*d* partial DOS has been multiplied by factor 3 for clarity).

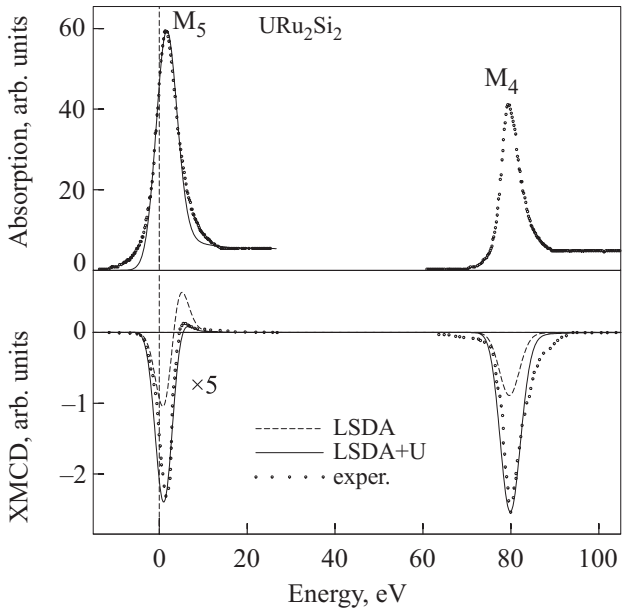

Fig. 26. Isotopic absorption and XMCD spectra of URu_2Si_2 at the uranium $M_{4,5}$ edges calculated in the LSDA (dashed lines) and LSDA + U (full lines) approximations [140]. Experimental spectra [69] (circles) were measured at 50 K and in a magnetic field of 5 T (the U M_4 spectra are shifted by –95 eV to include them in the figure).

peak at the M_5 edge (Fig. 26). The LSDA + U approximation with J = 2.0 and J = 0.5 eV and nonspherical corrections to Coulomb matrix elements [69] produces excellent agreement in shape and intensity for the XMCD spectra both at the M_4 and M_5 edges. This can be considered as evidence in favor of a picture of partly localized U 5*f* states in URu_2Si_2.

One should mention that the LSDA + U(OP) calculations (U_{eff} = 0) underestimate the negative XMCD peak and overestimate the positive one at the M_5 edge (not shown). This approximation also slightly underestimates the XMCD signal at the M_4 edge.

2.3.3. UPd_2Al_3 *and* UNi_2Al_3

The most recently discovered heavy-fermion superconductors UPd_2Al_3 and UNi_2Al_3 [163,164] exhibit coexistence between superconductivity and a magnetic state with relatively large ordered magnetic moments. UPd_2Al_3 was found to exhibit a simple antiferromagnetic structure [wave vector $\mathbf{q}$ = (0,0,1/2)] below $T_N \sim 14.5$ K and static magnetic moments of U lying in the basal plane [165]. The neutron-scattering data are consistent with an ordered magnetic moment $M_t \sim 0.85\ \mu_B$, reduced compared to the effective moment obtained from the high-temperature susceptibility, but exceeding by up to two orders of magnitude the small moments found, for example, in UPt_3. Hence, in contrast to UPt_3, a picture of local-moment magnetism seems to describe the magnetic state in UPd_2Al_3. Surprisingly, this large-moment magnetism was found to coexist with heavy-fermion superconductivity exhibiting the highest T_C reported to date for this class of materials.

The electronic structure and Fermi surface of the antiferromagnetic UPd_2Al_3 were calculated using the LSDA approximation in Refs. 166–168. The calculated magnetic moment was in good agreement with experiment as was the calculated magnetocrystalline anisotropy. The calculations reveal the importance of hybridization of the U 5*f* states with the valence states of Pd and Al even though this hybridization appears to be rather weak and to influence only a restricted energy interval in the U 5*f* bands. The calculated dHvA frequencies are found to be in good agreement with the experimental data. However, the observed heavy masses cannot be obtained within the LSDA [168].

The measured (in Ref. 169) x-ray photoemission and bremsstrahlung isochromat spectra of UPd_2Al_3 are well reproduced by the LSDA calculated U 5*f* density of states. On the other hand, the resonance photoemission spectra of UPd_2Al_3 does not match the calculated U 5*f* DOS in shape or position, while the calculated Pd 4*d* DOS matches very well with the off-resonance spectrum [170].

The superconducting and magnetic properties of UNi_2Al_3 are not so well documented compared to those of UPd_2Al_3 owing to the difficulties of preparing good single crystals [68]. UNi_2Al_3 undergoes transitions to antiferromagnetism at $T_N \sim 4.6$ K and to superconductivity at $T_C \sim 1.2$ K [164]. Muon spin rotation (μSR) experiments [171] on polycrystalline UNi_2Al_3 showed evidence for antiferromagnetism with an ordered moment of the order of 0.1 μ_B. Elastic neutron scattering from a single-crystal sample of UNi_2Al_3 has revealed the onset of long-range magnetic order below $T_N = 4.6$ K [172]. The order is characterized by wave vector of the form $(1/2 \pm \tau, 0, 1/2)$, with $\tau = 0.110 \pm 0.0003$, indicating an incommensurate magnetic structure within the basal plane, which is simply stacked antiferromagnetically along c to form the full three-dimensional magnetic structure. The maximum amplitude of the ordered moment is estimated to be $(0.21 \pm 0.10)\ \mu_B$.

1. Band structure. UPd_2Al_3 and UPd_2Al_3 crystallize in a rather simple hexagonal structure $P6/mmm$ (D^1_{6h}, $PrNi_3Al_3$-type structure) with lattice constant $a = 5.365$ Å and $c/a = 4.186$ for UPd_2Al_3 and $a = 5.207$ Å and $c/a = 4.018$ for UNi_2Al_3.

The fully relativistic spin-polarized LSDA energy band structures and total DOS's of the antiferromagnetic UPd_2Al_3 and UNi_2Al_3 are shown in Fig. 27 [140]. The results of our band structure calculations of UPd_2Al_3 are in good agreement with previous calculations of Sandratskii et al. [167]. Al 3*s* states are located mostly at the bottom of the valence band in the –9.7 to –5 eV energy interval. Al 3*p* states occupy wide energy range from –6 to 11 eV

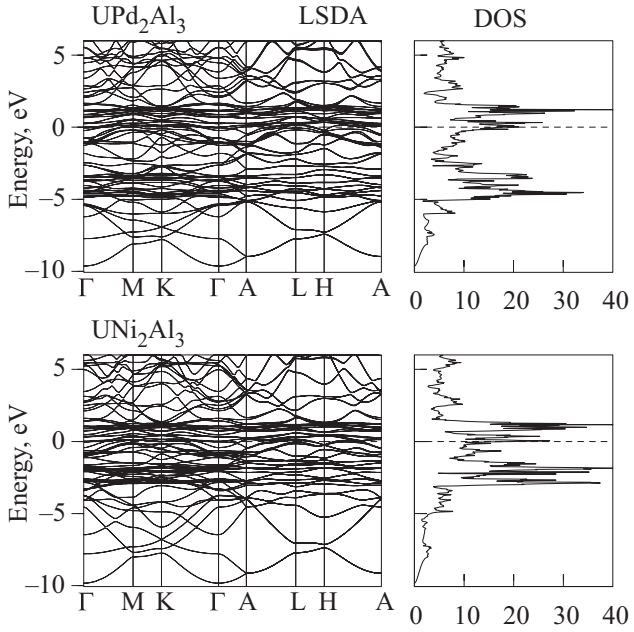

Fig. 27. The self-consistent fully relativistic, spin-polarized energy band structure and total DOS (in states/(unit cell·eV)) of UPd_2Al_3 and UNi_2Al_3 calculated in the LSDA approximation [140].

hybridized strongly with Pd 4*d*, U 6*d* and U 5*f* valence states. Pd 4*d* states are almost fully occupied and situated below Fermi level in the –5 to –2.5 eV range. The magnetic moment at the Pd site, therefore, is extremely small. U 6*d* states are strongly hybridized with Pd 4*d* as well as Al 3*p* states. The characteristic feature of the LSDA band structure is a narrow peak of U $5f_{5/2}$ states situated just at the Fermi level E_F. U $5f_{7/2}$ states are split off by strong spin-orbit coupling and form another narrow peak 1.2 eV above E_F. Because Pd 4*d* states are located far below the Fermi level, there is rather week U 5*f*–Pd 4*d* hybridization. We should mention, however, that this hybridization is of primary importance and influences greatly the form and width of the 5*f* peaks (the analysis of the hybridization effects in UPd_2Al_3 are presented in Ref. 167).

In agreement with experiment [165] we found the basal plane of the hexagonal structure to be the plane of easy magnetization in UPd_2Al_3. The magnetic structures with magnetic moments lying in the *xy* plane possess lower energy than those with atomic moments along the *z* axis. A rotation of the magnetic moment within the *xy* plane does not noticeably change the energy of the configuration as well as the value of the spin and orbital magnetic moments.

Our calculations, unfortunately, yield for the total energy of the in-plane ferromagnetic structure a slightly lower value than for the energy of the corresponding antiferromagnetic structure, although the difference of the total energy of the ferromagnetic and antiferromagnetic in-plane solutions is very small, about 9 meV per formula unit, and is close to the accuracy limit of our LMTO–LSDA calculations. This disagrees with experiment which shows the ground-state magnetic structure to be antiferromagnetic [165]. The same results were obtained by Sandratskii et al. in Ref. 167.

The energy band structure of UNi_2Al_3 and UPd_2Al_3 are very similar (Fig. 27) [140]. The major difference is in the energy location and width of the transition metal bands. Due to less spatial expansion of Ni 3*d* wave functions compared to Pd 4*d* wave functions the Ni 3*d* energy band is 1.5 times narrower than the corresponding 4*d* band in UPd_2Al_3. The Ni 3*d* energy band is situated in the –3 to –1.2 eV energy interval. Due to a shift of the Ni 3*d* band toward the Fermi level, the U 5*f*–Ni 3*d* hybridization in UNi_2Al_3 is increased in comparison with the U 5*f*–Pd 4*d* hybridization in UPd_2Al_3. A stronger interaction between 5*f* and conduction electrons when replacing Pd by Ni is manifested in a shift toward higher temperatures of the maxima of both the resistivity and the susceptibility together with the decrease of the magnetic ordering temperature T_N, the superconductivity temperature T_C, the antiferromagnetic moment and the smaller entropy change at T_N [68].

Figure 28 shows m_j projected $5f_{5/2}$ density of states in UPd_2Al_3 calculated in the LSDA and LSDA + U approximations [140]. We performed two LSDA + U band structure calculations. In the first calculation we used $U = J = 0.5$ eV, which gives $U_{\text{eff}} = 0$ (the so-called LSDA + U(OP) approximation). In the second one $U = 2.0$ eV and $J = 0.5$ eV. The LSDA approximation places the $5f_{5/2}$ density of states in close vicinity of the Fermi level at –0.5 to 0.5 eV with strong hybridization between states with different m_j. The Coulomb repulsion U_{eff} strongly influences the electronic structure of UPd_2Al_3 and UNi_2Al_3. In the Hartree–Fock-like LSDA + U solution with nonspherical corrections to Coulomb matrix elements, three particular $5f_{5/2}$ states ($m_j = -5/2$, $-3/2$, and $-1/2$) are almost completely occupied producing the $5f^3$ configuration for U in UPd_2Al_3 and UNi_2Al_3.

Table 5 lists the calculated spin M_s, orbital M_l, and total M_t magnetic moments at uranium site (in μ_B) as well as the ratio M_l/M_s for UPd_2Al_3 and UNi_2Al_3 [140]. Our LSDA results are in good agreement with previous LSDA calculations [167]. Surprisingly, LSDA calculations produce the total magnetic moments in UPd_2Al_3 and UNi_2Al_3 in good agreement with the experimental data. On the other hand, the LSDA calculations strongly underestimate the ratio M_l/M_s (especially in UNi_2Al_3) due to the underestimation of the orbital moment by LSDA-based computational methods. The ratio M_l/M_s in the LSDA + U(OP) calculations is in reasonable agreement with the experimental data for both the compounds.

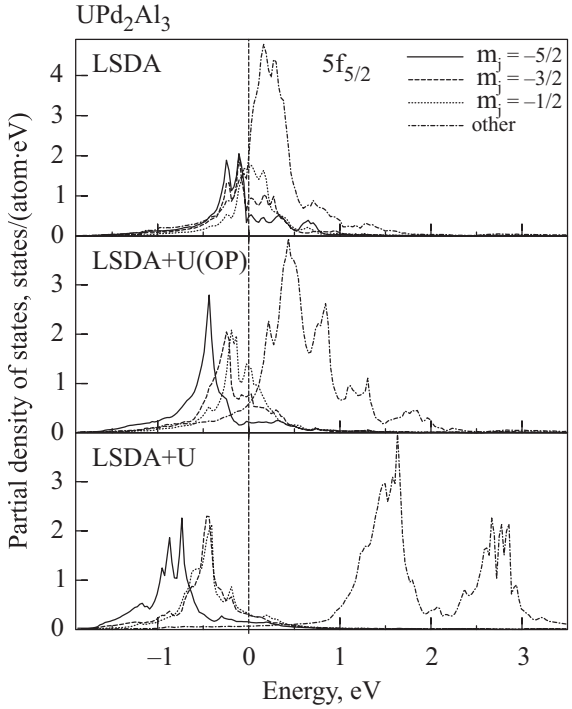

Fig. 28. The partial $5f_{5/2}$ density of states in UPd_2Al_3 [140].

Table 5. The experimental and calculated spin M_s, orbital M_l, and total M_t magnetic moments at uranium site (in μ_B) of UPd_2Al_3 and UNi_2Al_3. The magnetic moments calculated for easy magnetic axes, namely, hexagonal plane in UPd_2Al_3 and c axis in UNi_2Al_3 [140]

Compound	Method	M_s	M_l	M_t	$-M_l/M_s$
UPd_2Al_3	LSDA	–1.38	2.22	0.84	1.61
	LSDA [167]	–1.62	2.49	0.87	1.54
	LSDA + U(OP)	–1.59	3.73	2.14	2.34
	LSDA + U	–1.92	4.61	2.69	2.40
	exper. [165]	—	—	0.85	—
	exper. [68]	—	—	—	2.01
	exper. [69]	—	—	—	1.91
UNi_2Al_3	LSDA	–0.47	0.54	0.07	1.15
	LSDA + U(OP)	–1.22	2.90	1.68	2.38
	LSDA + U	–1.74	4.46	2.72	2.56
	exper. [165]	—	—	0.2	—
	exper. [68]	—	—	—	2.49

2. XMCD spectra. Figure 29 shows the calculated XMCD spectra in the LSDA, LSDA + U(OP) and LSDA + U approximations for UPd_2Al_3 [140] together with the corresponding experimental data [69]. The overall shapes of the calculated and experimental uranium $M_{4,5}$ XMCD spectra correspond well to each other. The major discrepancy between the calculated and experimental XMCD spectra is the size of the M_4 XMCD peak. The LSDA theory produces much smaller intensity for the XMCD spectrum at the M_4 edge in comparison with experiment and simultaneously strongly overestimates the negative peak at the M_5 edge. On the other hand, the LSDA + U(OP) approximation produces an excellent agreement in the shape and intensity of the XMCD spectra both at the M_4 and M_5 edges. The LSDA + U calculations with U = 2.0 eV slightly overestimate the intensity of the dichroic signal at the M_4 edge and produce a larger negative peak and smaller positive one at the M_5 edge.

Figure 29 shows also the XMCD spectra for UNi_2Al_3 [140]. The experimental data exist only for the M_4 edge in this compound [68]. For the LSDA calculations the theory produces a smaller intensity of the XMCD spectrum at the M_4 edge in comparison with the experiment. On the other hand, the intensity of the experimentally measured M_4 XMCD spectrum is in between the results obtained by LSDA + U(OP) and LSDA + U approximations.

2.3.4. UBe_{13}

The system UBe_{13} was the first U-based heavy-fermion superconductor discovered [173] and, similar to UPt_3, it shows peculiar properties, pointing to an unconventional superconducting order parameter. UBe_{13} is cer-

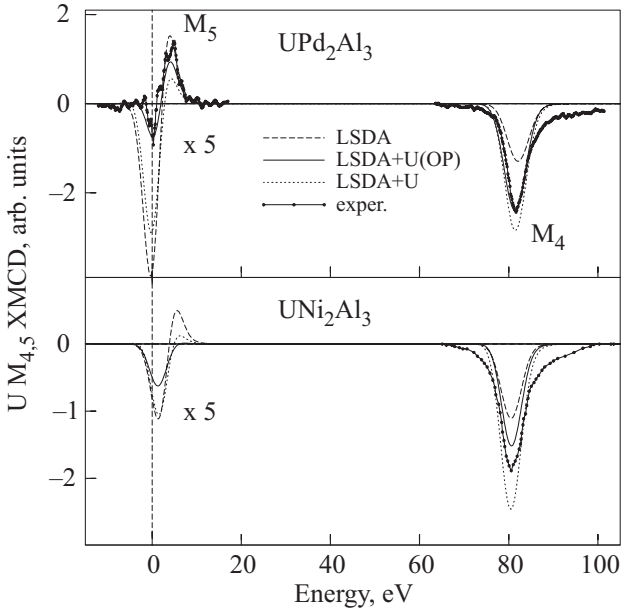

Fig. 29. The XMCD spectra of UPd_2Al_3 and UNi_2Al_3 at the uranium $M_{4,5}$ edges calculated in LSDA and LSDA + U approximations [140]. Experimental spectra for UPd_2Al_3 [69] were measured in a magnetic field of 5 T and 35 K. The experimental data for the U M_4 XMCD spectrum of UNi_2Al_3 is from Ref. 68 (the U M_4 spectra are shifted by –95 eV to include them in the figure).

tainly the most anomalous of the heavy-fermion superconductors.

The specific heat in UBe_{13} is very weakly dependent upon magnetic field and highly sensitive to pressure [174]. The low-temperature value of the electronic specific heat coefficient, γ is of order 1000 mJ/(mol·K^2), corresponding to an effective mass of several hundred free-electron masses. The magnetic susceptibility is weakly pressure dependent in comparison with the specific heat and under pressure has a completely different temperature dependence [175]. Doping on the U sublattice which drives away the specific heat anomaly leaves the low-temperature susceptibility essentially unchanged. The magnetization is linear in fields up to 20 T [174].

The dynamic magnetic susceptibility reveals no significant structure on the scale of 1 meV as is evidenced in *C/T* and instead shows a broad «quasielastic» response on the scale of 15 meV as evidenced in both neutron scattering and Raman spectra. Concomitant with the peak in χ'' is a Schottky anomaly in the specific heat, suggesting that the 15 meV peak represents highly damped crystal-field levels for which further evidence appears in the nuclear magnetic relaxation of the ^{9}Be sites. This dynamic susceptibility peak integrates to give 80% of the static susceptibility up to the experimental cut-off. This places a stringent bound on any hypothetical moment-carrying state in the low-frequency region; given a 10 K Kondo scale, to explain the residual susceptibility the effective squared moment must be less than 0.25 μ_B, which would appear to rule out an interpretation in terms of a $5f^3\ \Gamma_6$ ground state [174].

There are several different interpretations of these experimental data in literature. Miranda and coworkers suggested the non-Fermi-liquid (NFL) behavior of UBe_{13} could be driven by disorder [176]. Cox proposed, based on symmetry grounds, the NFL behavior can be explained by the two-channel Kondo model description [177]. More recently, Anders et al. tackled the problem for the corresponding lattice model [178]. They also performed a calculation of the optical properties within such a two-channel Anderson lattice model for which the suppression of the low-frequency Drude component and the development of a mid-infrared absorption in the excitation spectrum at low temperatures have been suggested [178].

One framework for describing the low-temperature properties of UBe_{13} characterizes the material's behavior in terms of its energy scales. Whereas common metals may be characterized by a single energy scale (the Fermi energy), UBe_{13} appears to require several. One may considered four energy scales [174]: a crystal field splitting of 150–189 K, a Kondo temperature of about 25 K, a spin-fluctuation temperature of about 2 K, and the superconducting transition temperature of about 0.8 K.

The energy band structure and Fermi surface of UBe_{13} have been investigated in Refs. 179–182 in a frame of the LSDA approximation. It was shown [182] that the hybridization between the U 5f states and the Be 2p states occurs in the vicinity of the Fermi level. The sheets of the Fermi surface are all small in size and closed in topology. The cyclotron effective mass calculated for the dHvA branches in the three symmetry directions varies from 1.08 m_0 to 4.18 m_0. The theoretical electronic specific-heat coefficient $\gamma_{\text{band}}^{LDA}$ is 13.0 mJ/(K^2·mol) [182]. The theoretical results for the electronic specific-heat coefficient are much less than the experimental ones, suggesting a large enhancement due to many-body effects. This disagreement between theory and experiment might be ascribed to the enhancements due to the electron correlations and/or the electron-phonon interaction which the LDA fails to take into account.

1. Band structure. UBe_{13} crystallizes in the $NaZn_{13}$-type fcc structure with the space group O_h^6–*Fm*3*c* (No 226) and contains 28 atoms per unit cell. There are two distinct Be sites, Be_1 and Be_2, with the 24 Be_2 sites having a very low site symmetry (only a mirror plane). The U atoms are surrounded by cages of 24 Be_2 atoms (Fig. 30) at the distance of 3.02 Å. Eight Be_1 atoms are separated from the U atom by 4.443 Å. This ensures that the U atoms widely separated. The U atoms form a simple cubic sublattice with a large U–U nearest-neighbor distance of $a/2$ = 5.13 Å, which guarantees that the *f*–*f* overlap is negligible. Therefore, all broadening of the U 5f states into bands results

entirely from hybridization with the conduction bands, rather than partially from direct *f–f* overlap, as occurs in many U compounds.

Self-consistent LSDA calculations produce a nonmagnetic ground state in UBe_{13} [140]. To calculate the electronic structure and XMCD spectra of UBe_{13} in the LSDA approximation, the term $2\mu_B \mathbf{B}\cdot\mathbf{s}$ which couples the spin of an electron to the external magnetic field was added to the Hamiltonian at the variational step. The fully relativistic spin-polarized LSDA energy band structure and total DOS of UBe_{13} is shown in Fig. 31 calculated in an external magnetic field of 20 T [140]. The occupied part of the valence band is formed predominantly by Be 2*s* and 2*p* states. U $5f_{5/2}$ states are situated just at the Fermi level 1.0 eV above the top of Be 2*p* states. U $5f_{7/2}$ states are split off by strong SO coupling and form another narrow peak 1 eV above E_F. Be 2*s* states are located mostly at the bottom of the valence band. Be 2*p* states are strongly hybridized with U 6*d* states in the –6 to –1 eV energy interval. On the other hand, there is quite large U 5*f*–Be 2*p* hybrization in vicinity of the Fermi level in the –0.6 to 1.4 eV energy range. Although every individual Be atom produces a quite small 2*p* partial density of states, due to the large number of Be atoms they sum up to a 2*p* DOS comparable in intensity with the U 5*f* DOS (Fig. 31).

Figure 31 also shows the band structure of UBe_{13} calculated in the LSDA + *U* approximation with U = 2.0 eV and J = 0.5 eV. Partially occupied U $5f_{5/2}$ states split due to the Coulomb repulsion and the LSDA + *U* calculations give a solution with three localized 5*f* electrons. These localized 5*f* states form a rather narrow peak at 0.6 eV below E_F. U 5*f* states just above the Fermi level are formed by the remaining $5f_{5/2}$ states whereas the peak of $5f_{7/2}$ states is pushed from its LSDA position at 1.2 eV above E_F to 2.2 eV.

Figure 32 shows m_j projected $5f_{5/2}$ and total $5f_{7/2}$ density of states in UBe_{13} calculated in the LSDA and LSDA + *U* approximations [140]. We performed two LSDA + *U* band

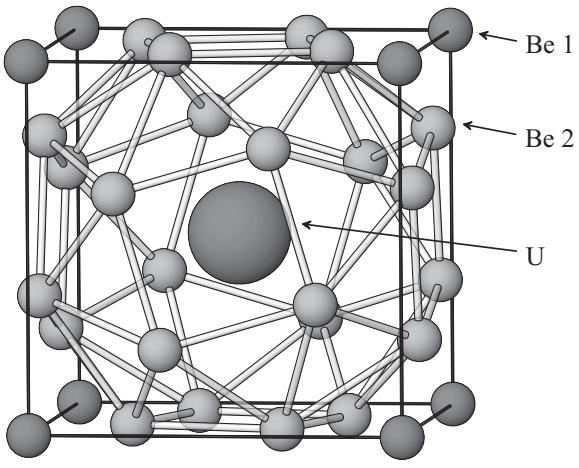

Fig. 30. Crystal structure of UBe_{13}.

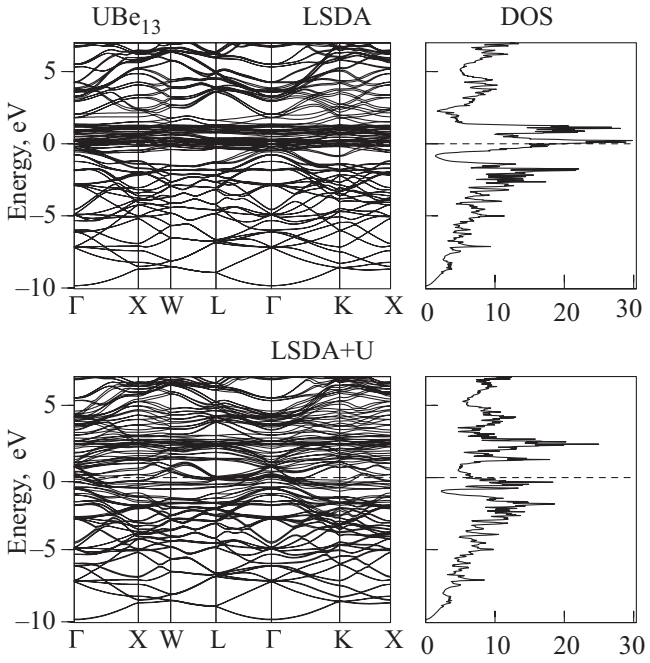

Fig. 31. The energy band structure and total density of states (in states/(unite cell·eV) in UBe_{13} calculated in the LSDA and LSDA + *U* approximations [140].

structure calculations both with U = 2.0 eV and J = 0.5 eV. In the first calculation we used the LSDA + *U* method with nonspherical corrections to the Coulomb matrix elements [73]. The effect of a less asymmetric density of localized 5*f* electrons can be simulated by replacing the matrix elements $U_{mmm'm'}$ and $J_{mm'm'm}$ by averaged Coulomb U and exchange J integrals, respectively, and setting all other matrix elements to zero [73]. In the nonrelativistic limit this would correspond, except for the approximation to the double counting term, to the original version of the LSDA + *U* method proposed in Ref. 183. In this case all unoccupied U 5*f* electrons independently of their angular momentum experience the same Coulomb repulsion as the localized ones. In the Hartree–Fock-like LSDA + *U* solution with nonspherical corrections to the Coulomb matrix elements three particular $5f_{5/2}$ states ($m_j = -5/2$, $-3/2$, and $-1/2$) are occupied which leads to (i) large spin ($-1.95\ \mu_B$) and orbital ($4.47\ \mu_B$) magnetic moments of U atom and (ii) strongly anisotropic Coulomb interaction of the remaining 5*f* electrons with the occupied ones. In the calculations using the LSDA + *U* method with spherically averaged U and J an unoccupied U 5*f* electrons feel a much more isotropic repulsive potential and is situated closer to the Fermi energy. This gives smaller magnetic moments (spin moment is equal to –1.82 μ_B and orbital moment 4.08 μ_B) in comparison with the nonspherial solution. The $5f_{5/2}$ states with $m_j = -1/2$ became partly empty for the calculations with spherically averaged U and J and the main peak of $N_{-1/2}$ DOS is situated just above the Fermi level (Fig. 32).

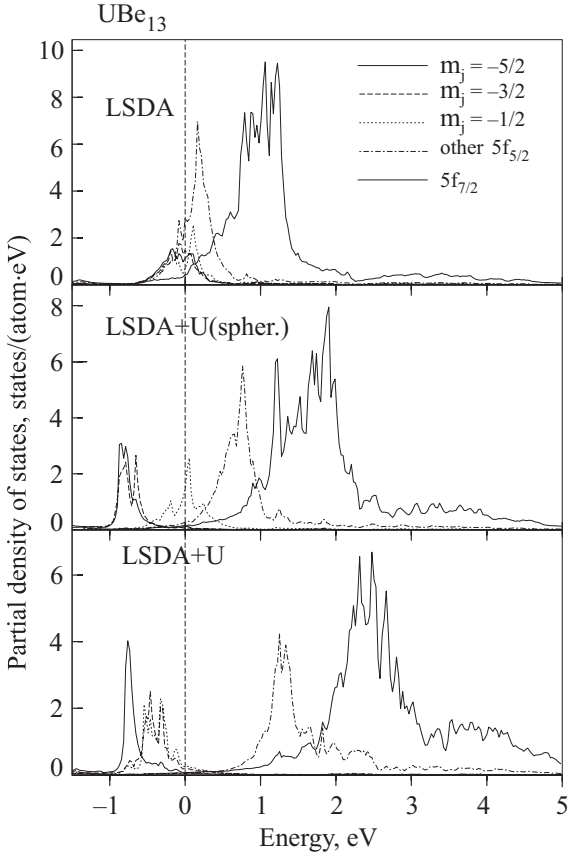

Fig. 32. The m_j projected $5f_{5/2}$ and total $5f_{7/2}$ density of states in UBe_{13} calculated in the LSDA and LSDA + U approximations [140].

The three calculations presented in Fig. 32 produce rather different energy locations for the empty 5f states [140]. The principal question of the energy position of the empty 5f states is usually answered by bremsstrahlung isochromat spectroscopy (BIS) measurements. Figure 33 shows the experimental BIS spectrum of UBe_{13} [184] compared with the calculated energy distribution for the unoccupied partial U 5f density of states in the LSDA and LSDA + U approximations. The LSDA places empty 5f states too close to the Fermi level (Fig. 33). The LSDA + U calculations with nonspherical solution place the maximum of empty 5f states more than 1 eV higher than the experiment. The LSDA + U calculations with spherically averaged U and J give the correct position of empty 5f states within the experimental resolution (Fig. 33). The main peak in the BIS spectrum is derived from the U $5f_{7/2}$ states, while the low energy shoulder split off from the main peak is from the $5f_{5/2}$ states.

2. XMCD spectra. Figure 34 shows the UBe_{13} x-ray isotropic absorption and XMCD spectra calculated in the LSDA and LSDA + U approximations [140] together with the experimental data [65]. The LSDA calculations produce much smaller intensity of the XMCD spectrum at the M_4 edge in comparison with the experiment and simultaneously give larger dichroic signal for the negative peak

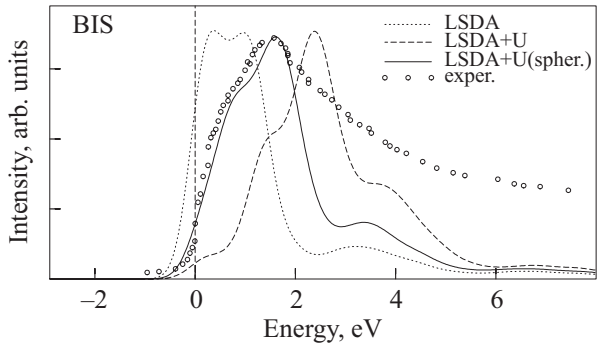

Fig. 33. Comparison of the calculated U partial 5f DOS in the LSDA (dotted line), LSDA + U approximations with the experimental BIS spectrum (circles) of UBe_{13} [184]. Dashed line presents DOS calculated with nonspherical correction to Coulomb matrix elements whereas full line are calculated with averaged U and J [140].

and do not produce the positive shoulder at the M_5 edge (Fig. 34). On the other hand, the LSDA + U calculations improve the agreement between the theory and the experiment in the shape and intensity of XMCD spectra both at the M_4 and M_5 edges. The LSDA + U method with nonspherical corrections to the Coulomb matrix elements slightly overestimates the dichroic signal at the M_4 edge, underestimates the intensity of the positive peak and strongly overestimates the negative peak at the M_5 edge.

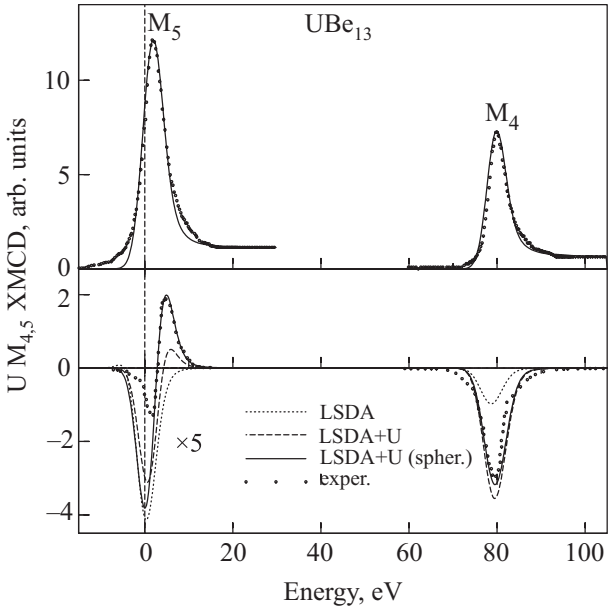

Fig. 34. Isotropic absorption and XMCD spectra of UBe_{13} at the uranium $M_{4,5}$ edges calculated in the LSDA (dotted lines), and LSDA + U approximations. The dashed line presents XMCD spectra calculated with nonspherical corrections to Coulomb matrix elements whereas the full line results are calculated with averaged U and J [140]. Experimental spectra [65] (circles) were measured at 12 K and in a magnetic field of 5 T (the U M_4 spectrum is shifted by –95 eV to include it in the figure).

The LSDA + U calculations with averaged U and J give a correct value of the positive peak at the M_5 edge and the negative peak at the M_4 one but still overestimate the intensity of the negative peak at the M_5 edge.

UBe_{13} is unlike the other heavy-fermion compounds in that the better description of its XMCD and BIS spectra requires spherically averaged U and J values. The physical reason for that is not clear, however there are some indications from the calculations. Compare the orbital resolved $5f_{5/2}$ DOS's shown in Fig. 32 one can see that in the LSDA + U solution with nonspherical corrections to the Coulomb matrix elements, three particular $5f_{5/2}$ states ($m_j = -5/2$, $-3/2$, and $-1/2$) are fully occupied which leads to a pure $5f^3$ configuration. The calculations using the spherically averaged U and J values give a solution with partly empty $m_j = -1/2$ states with the main peak of the $N_{-1/2}$ DOS very close to the Fermi level (Fig. 32). This is the typical situation for a system with mixed valence [38,185]. One should mention that the LSDA + U method which combines LSDA with a basically static, i.e., Hartree–Fock-like, mean-field approximation for a multi-band Anderson lattice model does not contain true many-body physics and cannot treat a systems with mixed valence properly. The evaluation of the electronic structure of UBe_{13} needs further theoretical investigations.

2.4. UGe_2

The coexistence of ferromagnetism (FM) and superconductivity (SC) has been at the forefront of condensed matter research since a pioneering paper by Ginzburg [186]. The interplay between two long-range orderings FM and SC is a fascinating aspect in strongly correlated electron systems because generally SC does not favorably coexist with FM since the FM moment gives rise to an internal magnetic field, which breaks the pairing state.

During the last three decades, however, the discovery of a number of magnetic superconductors has allowed for a better understanding of how magnetic order and superconductivity can coexist. It seems to be generally accepted that antiferromagnetism with local moments coming from rare-earth elements readily coexists with type-II superconductivity [187]. This is because superconductivity and magnetism are carried by different types of electrons; magnetism is connected with deeply seated $4f$ electrons, while superconductivity is fundamentally related to the outermost electrons such as s, p, and d electrons. In the case of a ferromagnetic superconductor the situation is more complex because internal fields are not canceled out in the range of a superconducting coherence length in contrast with an antiferromagnetic superconductor.

Recently, UGe_2 has attracted considerable attention because the coexistence of SC and FM was found under high pressure [188,189]. It is particularly interesting to note that both of ferromagnetism and superconductivity may be carried by itinerant $5f$ electrons, which can be homogeneously spread in the real space, although it is still a matter of debate and remains to be resolved.

UGe_2 crystallizes in the orthorhombic $ZrGa_2$ structure (space group *Cmmm*). At ambient pressure, UGe_2 orders ferromagnetically below the Curie temperature $T_C = 52$ K with the ordered moment of $1.4\,\mu_B$. The magnetic properties are strongly anisotropic, and the easy magnetization axis is the crystallographic a axis of the $ZrGa_2$ structure. Superconductivity is found in the pressure range of 1.0 to 1.6 GPa. The highest superconducting critical temperature $T_{SC} = 0.8$ K at the pressure $P_C = 1.2$ GPa, while $T_C = 35$ K at that pressure. As the applied pressure increases, the superconductivity disappears where the ferromagnetism disappears at around 1.7 GPa. Therefore, the superconductivity and ferromagnetism in UGe_2 seem to be closely related, although the mechanism of superconductivity has not been understood yet, and it is very important to characterize the magnetic properties of UGe_2. The XMCD technique developed in recent years has evolved into a powerful magnetometry tool to separate orbital and spin contributions to element specific magnetic moments. XMCD experiments measure the absorption of x-rays with opposite (left and right) states of circular polarization.

In a recent publication [190] we reported on the x-ray absorption and magnetic circular dichroism measurements performed at the $M_{4,5}$ edges of uranium in the ferromagnetic superconductor UGe_2. The spectra are well described with the LSDA + U electronic structure computation method. Combined with the analysis of the published (i) x-ray photoemission spectrum, (ii) two-dimensional electron positron momentum density, and (iii) angular dependence of the de Haas–van Alphen frequencies, we infer for the Coulomb repulsion energy within the $5f$ electron shell $U = 2$ eV.

The present work is an extension of the previous study. Recently, Okane et al. [191] measured x-ray absorption magnetic circular dichroism at the U $N_{4,5}$ and $N_{2,3}$ edges as well as at the Ge $L_{2,3}$ ones for the ferromagnetic superconductor UGe_2 in the normal state. The orbital and spin magnetic moments deduced from the sum rule analysis of the XMCD data indicate that the U atom in UGe_2 is considered to be closer to the trivalent state rather than the tetravalent state. The XMCD measurement at the U $N_{2,3}$ indicates that the U $6d$ electrons have negligibly small magnetic contributions.

Inada et al. [192] also performed XMCD experiments at the Ge K edge in UGe_2. The Ge K edge XMCD spectrum shows a main negative peak near the edge and a small positive one at 7 eV above the edge. The amplitude of this spectrum is unusually very large in spite of being at ligand sites.

1. U $N_{4,5}$ *XMCD spectra*. Figure 35 shows the calculated XAS and XMCD spectra in the LSDA and LSDA + U approximations for UGe_2 at the $N_{4,5}$ edges together with the corresponding experimental data [191]. The experimentally measured XAS spectra have a rather simple line shape composed of two white line peaks at the N_5 and N_4 edges and no distinct fine structures due to multiplet splitting were observed. This justifies the description of the absorption of the incident x-rays in terms of a one-particle approximation. Hence, valuable information on the nature of the $5f$ electrons can be obtained from comparison of experimental data to results of band-structure calculations.

The XMCD signals at the N_5 and N_4 edges have the same sign, and the XMCD signals at the N_4 edge have a much higher intensity than those at the N_5 edge. These behaviors were commonly observed in the XMCD spectra at the U $M_{4,5}$ edges of the ferromagnetic uranium compounds [43] from which one can conclude that the orbital and the spin magnetic moments are directed in the opposite direction to each other.

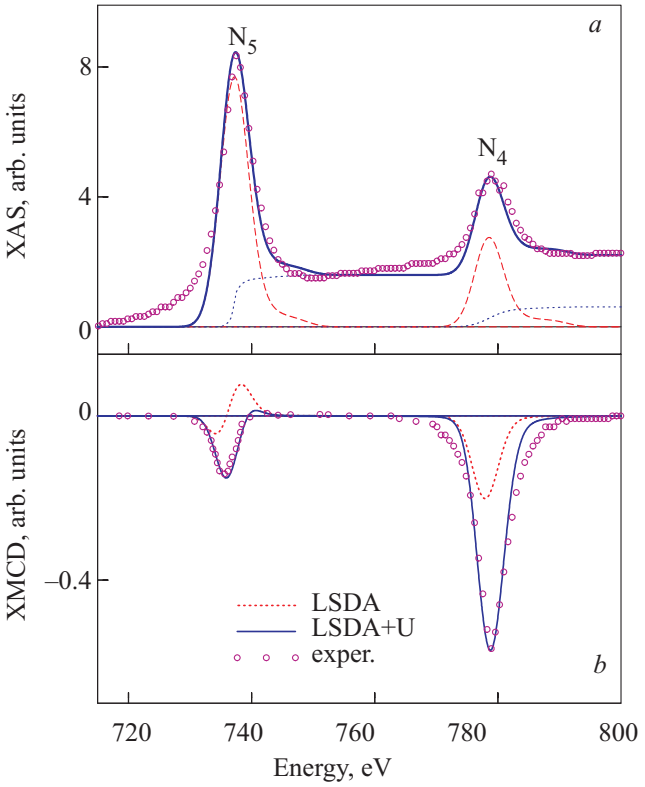

Fig. 35. (*a*) Theoretically calculated [193] (dashed line) and experimental [191] (circles) isotropic absorption spectra of UGe_2 at the U $N_{4,5}$ edges. Experimental spectra were measured with external magnetic field (2 T) at 25 K. Dotted lines show the theoretically calculated background spectra, full thick lines are sum of the theoretical XAS and background spectra. (*b*) Experimental [191] (circles) XMCD spectra of UGe_2 at the U $N_{4,5}$ edges in comparison with theoretically calculated ones using the LSDA (dotted lines) and LSDA + U (full lines) approximations.

A qualitative explanation of the XMCD spectra shape is provided by the analysis of the orbital character, occupation numbers of individual $5f$ orbitals and corresponding selection rules. Because of the electric dipole selection rules ($\Delta l = \pm 1$; $\Delta j = 0, \pm 1$) the major contribution to the absorption at the N_4 edge stems from the transitions $4d_{3/2} \to 4f_{5/2}$ and that at the N_5 edge originates primarily from $4d_{5/2} \to 5f_{7/2}$ transitions, with a weaker contribution from $4d_{5/2} \to 5f_{5/2}$ transitions. The selection rules for the magnetic quantum number m_j (m_j is restricted to $-j, \ldots + j$) are $\Delta m_j = +1$ for $\lambda = +$ and $\Delta m_j = -1$ for $\lambda = -$.

In our previous paper [72] we show that qualitatively the XMCD spectrum of U at the M_5 edge ($I = \mu^- - \mu^+$) can be roughly represented by the following m_j projected partial density of states: $[N^{7/2}_{-7/2} + N^{7/2}_{-5/2}] - [N^{7/2}_{7/2} + N^{7/2}_{5/2}]$. Here we used the notation $N^{j}_{m_j}$ with the total momentum j and its projection m_j. As a result, the shape of M_5 XMCD spectrum usually results in two peaks of opposite sign: a negative peak at lower energy and a positive peak at higher energy. Relative intensity of the negative and positive lobes depends on the value of crystal field and Zeeman splitting of the $5f_{7/2}$ electronic states [116]. As the separation of the peaks is smaller than the typical lifetime broadening, the peaks cancel each other to a large extent, thus leading to a rather small signal. Similar consideration is valid also for the N_5 edge.

It can be shown (see [72]) that the XMCD spectrum of U at the M_4 and N_4 edges can be fairly well represented by considering m_j projected partial density of states: $-[N^{5/2}_{3/2} + N^{5/2}_{5/2}]$. It explains why the dichroic M_4 as well as N_4 lines in uranium compounds consist of a single nearly symmetric negative peak.

We should note, however, that the explanation of the XMCD line shape in the terms of partial DOS's presented above should be considered only qualitatively. First, there is no full compensation between transitions with equal final states due to difference in the angular matrix elements; second, in our consideration we neglect cross terms in the transition matrix elements. Besides, we have used here the *jj*-coupling scheme where the total momentum $\mathbf{j}$ is written as $\mathbf{j} = \mathbf{l} + \mathbf{s}$. However, the combination of the hybridization, Coulomb, exchange and crystal-field energies may be so large relative to the $5f$ spin-orbit energy that the *jj*-coupling is no longer an adequate approximation.

Figure 35,*b* shows the calculated XMCD spectra in the LSDA and LSDA + U approximations for UGe_2 together with the corresponding experimental data [191]. The overall shapes of the calculated and experimental uranium $N_{4,5}$ XMCD spectra correspond well to each other. The major discrepancy between the calculated and experimental XMCD spectra is the size of the N_4 XMCD peak. The LSDA theory produces much smaller intensity

for the XMCD spectrum at the N_4 edge in comparison with the experiment. It also can't produce the correct shape of the N_5 XMCD spectrum. On the other hand, the LSDA + U approximation with U = 2 eV produces excellent agreement in the shape and intensity of XMCD spectra at the $N_{4,5}$ edges.

Now we focus on values of moments of the 5f shell. The orbital magnetic moment can be estimated from the XMCD sum rules [74,194]. By integrating the experimentally measured XAS and XMCD spectra at the $M_{4,5}$ edges we obtained μ_L = 1.91 and 1.75 μ_B for the hypothetical f^2 and f^3 configurations, respectively [190]. A similar procedure has been used by Okane et al. at the $N_{4,5}$ edges [191], they obtained μ_L = 1.89 and 2.35 μ_B for the f^2 and f^3 configurations, respectively. Although the values for the f^2 configuration are very close, the values for the f^3 configuration differ more than 30 %. One of the possible reasons for such disagreement might be connected with the fact that the application of the sum rule is valid only when the spin orbit splitting of the core level is sufficiently large compared with other interactions including the core-valence Coulomb and exchange interaction. The condition may not be so clear at the U $N_{4,5}$ edges because the spin-orbit splitting is considerably smaller than that at the U $M_{4,5}$ edges [191]. One should mention also that XMCD sum rules are derived within an ionic model using a number of approximations [43,195]. The largest mistake comes from the ignorance of the energy dependence of the radial matrix elements in sum rules, sometimes it can produce an error up to 100 % [196].

From our LSDA + U band structure calculations with U = 2 eV we obtain a larger 5f orbital magnetic moment: M_l = 3.46 μ_B, which may indicate that the LSDA + U is producing too much localization for the 5f orbitals [73].

The analysis of the orbital projected DOS provided in our previous paper shows that for U = 2 eV the two most populated 5f orbitals become almost completely occupied and corresponding peaks of orbital resolved DOS are found below the Fermi energy, E_F (see Fig. 3 in [190]). The third most occupied orbital remains only partially occupied. Whereas the main peak of DOS projected onto this orbital is situated below E_F, an additional narrow peak can be seen just above the Fermi level. Even for U = 4 eV the third peak remains partially occupied. We can conclude that the U atom in UGe_2 possesses a valency somewhat in between U^{4+} (f^2) and U^{3+} (f^3).

One should mention that the ratio $R = -\mu_L/\mu_S$ of the orbital to spin moment is not in disagreement with the experiment: our LSDA + U calculations produce R = 2.25, while the experimental estimations give 2.24 and 2.51 for f^3 configurations by integrating the spectra at the $M_{4,5}$ and $N_{4,5}$ edges, respectively [190,191].

2. U $N_{2,3}$ and Ge $L_{2,3}$ XMCD spectra. In order to investigate the contribution of the U 6d electrons to the magnetization, Okane et al. [191] have measured XMCD at the U $N_{2,3}$ edges, too. Figure 36 shows the calculated XAS and XMCD spectra in the LSDA + U approximations for UGe_2 at the N_3 edge together with the corresponding experimental data [191]. The experimentally measured XAS spectrum has quite large background intensity. One can see that no appreciable XMCD signals are observed at the U N_3 edge.

The theoretical LSDA + U calculations also produce a XMCD spectrum of very small intensity Fig. 36,*b*. It might be connected with quite a small U 6d spin and orbital magnetic moments equal to 0.075 and –0.041 μ_B, respectively.

Okane et al. also measured XAS and XMCD spectra in the region of the Ge $L_{2,3}$ absorption edges [191]. The spectra have quite complicated line shapes and it is hard to separate the Ge $L_{2,3}$ signal from U N_2 and Gd M_4 XMCD signals. The later arises from the sample holder. Figure 37 presents the calculated XMCD spectra of the UGe_2 at the Ge $L_{2,3}$ edges compared with the experimental data [191]. The authors of [191] consider a positive peak B at 1215 eV, a negative peak C at 1228 and another

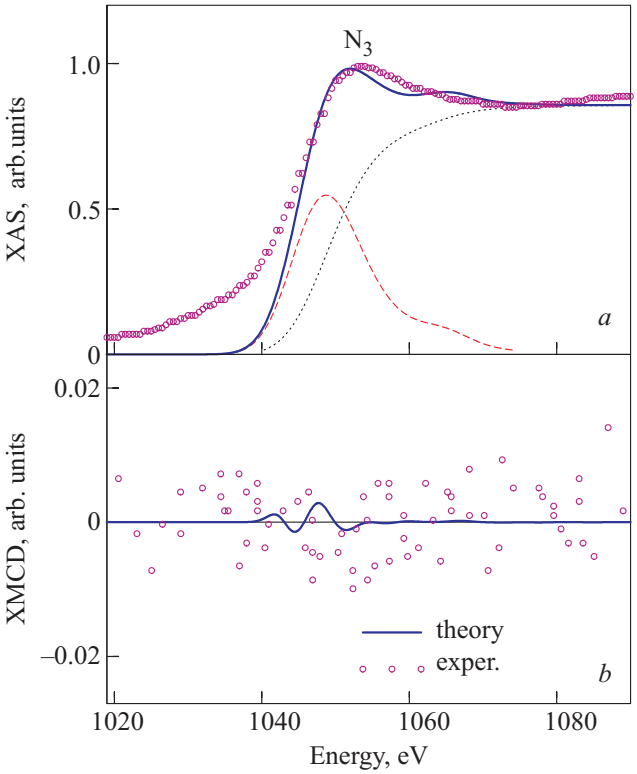

Fig. 36. (*a*) Theoretically calculated [193] (dashed line) and experimental [191] (circles) isotropic absorption spectra of UGe_2 at the U N_3 edge. Dotted lines show the theoretically calculated background spectrum, full thick line is sum of the theoretical XAS and background spectrum. (*b*) Experimental [191] (circles) XMCD spectrum of UGe_2 at the U N_3 edge in comparison with theoretically calculated ones using the LSDA + U approximations (full line).

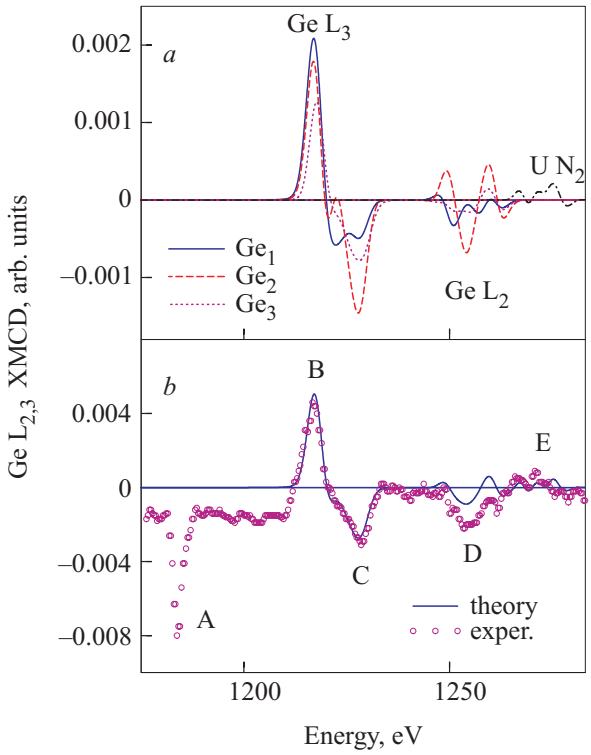

Fig. 37. (*a*) Theoretically calculated [193] XMCD spectra of UGe_2 at the U N_2 and Ge $L_{2,3}$ edges at different Ge sites; (*b*) experimental [191] (circles) XMCD spectra of UGe_2 at the Ge $L_{2,3}$ and U N_2 edges in comparison with theoretically calculated ones using the LSDA + U approximations (full line).

negative peak D at 1255 eV as the XMCD spectra of the Ge $L_{2,3}$ edges, since the energy separation between those structures is close to the spin orbit splitting of the Ge $L_{2,3}$ core level 30 eV. A strong negative peak at around 1183 eV (peak A) apparently comes from the Gd M_5 spectrum of the sample holder. A positive XMCD peak at 1215 eV may include probably not only the Ge L_3 contribution but also a contribution from Gd M_4, and the broad hump at around 1270 eV may arise from U N_2 contributions [191].

Our band structure calculations perfectly describe the peaks B and C as the L_3 XMCD spectrum, while the L_2 XMCD spectrum well reproduces the fine structure D. Due to larger U $4p_{1/2}$ electron energy binding in comparison with the Ge $2p_{1/2}$ one, U N_2 XMCD spectrum is situated at the higher energy side of the Ge L_2 spectrum (peak E). The values of Gd $5d$ orbital (spin) magnetic moments are equal to 0.018 (0.019), 0.022 (0.013) and 0.010 (0.011) μ_B at the Ge_1, Ge_2, and Ge_3 sites, respectively. The main contribution to the intensity of XMCD $L_{2,3}$ spectra come from Ge_1 and Ge_2 sites because they have larger magnitude for their spin and orbital polarizations (Fig. 37,*a*).

Through turning the SOI off separately on the Ge $4d$ and the U $5f$ states we found that the negative peak C originates from the spin polarization in the Ge $4d$ symmetric states through the SOI while the Ge $4d$ and U $5f$ hybridization is responsible for large positive XMCD at around 1215 eV (peak B).

One should mention that XMCD spectra at the U $N_{2,3}$ and Ge $L_{2,3}$ edges are mostly determined by the strength of the SO coupling of the initial U $4p$ and Ge $2p$ core states and spin-polarization of the final empty $d_{3/2,5/2}$ states while the exchange splitting of the U $4p$ and Ge $2p$ core states as well as the SO coupling of the d valence states are of minor importance for the XMCD at the U $N_{2,3}$ and Ge $L_{2,3}$ edges of UGe_2.

3. Ge K XMCD spectrum. The $4p$ states in transition metals usually attract only minor interest because they are not the states responsible for magnetic or orbital orders. Recently, however, understanding $4p$ states has become important since XMCD spectroscopy using K edges of transition metals became popular, in which the $1s$ core electrons are excited to the $4p$ states through the dipolar transition. The K edge XMCD is sensitive to electronic states at neighboring sites, because of delocalized nature of the $4p$ states. It is expected that the ligand site XMCD is a candidate for one of the effective probes which can detect the mixing between p and f states in uranium compounds.

Figure 38,*b* shows the calculated XMCD spectra in the LSDA + U approximations for UGe_2 at the K edge together with the corresponding experimental data [192]. The experimental XMCD spectrum shows a main negative peak near 11100 eV and a small positive peak at about 7 eV higher. One might expect only tiny signals of XMCD from the $4p$ band, because it does not possess a large magnetic moment. However, the intensity of the negative peak of UGe_2 K XMCD spectrum reaches about 3% of the intensity of the fluorescence (or absorption) from K edge [192]. This value is large. Even the iron K edge XMCD is only on the order of 0.3% [197].

The K XMCD spectra come from the orbital polarization in the empty p states, which may be induced by (i) the spin polarization in the p states through the spin-orbit interaction (SOI), and (ii) the orbital polarization at neighboring sites through hybridization.

We calculated the XMCD spectra at Ge site with turning the SOI off separately on the Ge $4p$ and the U $5f$ states, respectively. We found that the prominent negative peak is reduced in intensity more than one order of magnitude when the SOI on the U $5f$ states is turned off, while the small positive lobe almost does not change. When the SOI on the Ge $4p$ orbital is turned off the negative prominent peak is slightly changed and the positive lobe is diminished. We can conclude that the positive lobe originates from the spin polarization in the Ge $4p$ symmetric states through the SOI. The Ge $4p$ and U $5f$ hybridization is responsible for large negative XMCD near the Ge K edge. This indicates that the Ge $4p$ orbital polarization originates mainly from the large $5f$ orbital polarizations

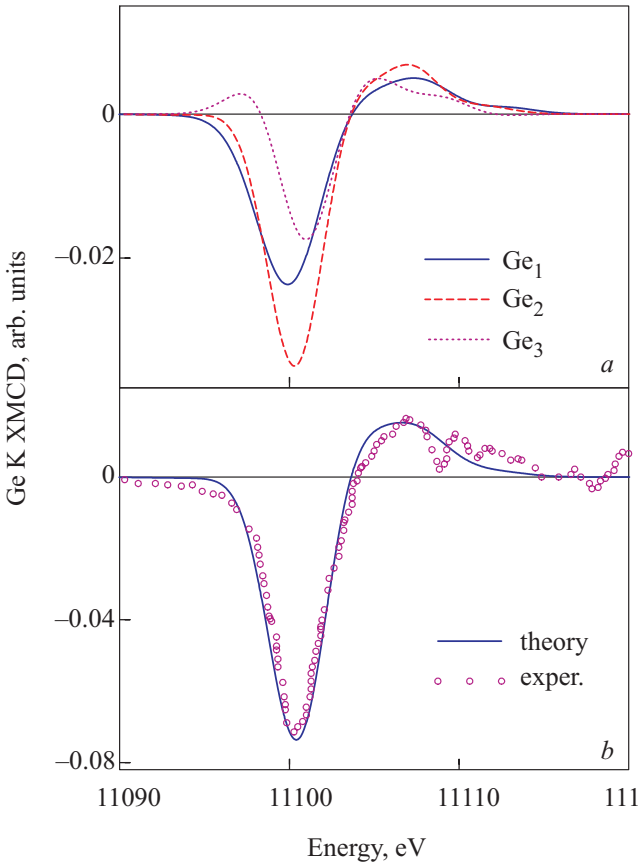

Fig. 38. (*a*) Theoretically calculated [193] XMCD spectra of UGe_2 at the *K* edge at different Ge sites; (*b*) theoretically calculated XMCD spectrum of UGe_2 at the Ge *K* edge using the LSDA + *U* approximations (full line) in comparison with the experimental one [192] (circles). Experimental spectrum was measured at 3 K with external magnetic field (0.5 T) applied along *a* axis.

at neighboring U atoms through Ge 4*p*–U 5*f* hybridization. This mechanism seems different from the XMCD in transition metal compounds in which the 4*p* orbital polarization is induced mostly by the 4*p* spin polarization at the atom itself through the SOI [43].

Similar results have been obtained by Usuda et al. [198] for the magnetic resonant x-ray scattering (MRXS) spectra at Ga sites in the antiferromagnetic cubic phase of UGa_3: the MRXS intensity largely decreased when the SOI on the U 5*f* states is turned off, while it was only slightly reduced when the SOI on the Ga 4*p* orbital is turned off.

From our LSDA + *U* band structure calculations the value of the orbital magnetic moment in the *p* projected bands are equal to –0.025, –0.031, and –0.006 μ_B at Ge_1, Ge_2, and Ge_3 sites, respectively. The contributions to the intensity of XMCD *K* spectrum from different Ge sites are related to the magnitude of their orbital polarizations (Fig. 38,*a*).

3. Summary

Recent progress in first-principles calculations of the x-ray magnetic dichroism illustrates that the XMCD spectra are developing into a powerful tool for tracing the electronic and magnetic structure of solids. The density-functional theory in the local-density approximation gives a fully satisfactory explanation of the XMCD spectra of transition metal compounds and alloys in most cases. Morover, theory can help to understand the nature of XMCD spectra and gives some recommendations how to create compounds with appropriate magnetic properties.

We demonstrated that XMCD *K* spectrum reflects the orbital polarization in differential form of the *p* states. Due to small exchange splitting of the initial 1*s* core states only the exchange and spin-orbit splitting of the final 4*p* states is responsible for the observed dichroism at the *K* edge. The XMCD spectra of transition metals for the $L_{2,3}$ edge are mostly determined by the strength of the SO coupling of the initial 2*p* core states and spin-polarization of the final empty $3d_{3/2,5/2}$ states while the exchange splitting of the 2*p* core states as well as SO coupling of the 3*d* valence states are of minor importance.

The recently derived sum rules for the orbital and spin magnetic moments were tested for several compounds. XMCD sum rules are derived within an ionic model using a number of approximations. For $L_{2,3}$, they are: (1) ignoring the exchange splitting of the core levels; (2) replacing the interaction operator $\boldsymbol{\alpha}\cdot\mathbf{a}_\lambda$ by $\boldsymbol{\nabla}\cdot\mathbf{a}_\lambda$; (3) ignoring the asphericity of the core states; (4) ignoring the difference of $d_{3/2}$ and $d_{5/2}$ radial wave functions; (5) ignoring $p \to s$ transitions; (6) ignoring the energy dependence of the radial matrix elements. The last point is the most important. We show that the energy dependence of the matrix elements and the presence of $p \to s$ transitions affect strongly the values of both the spin and the orbital magnetic moments derived from the sum rules.

In most of the 4*f* systems, the *f* electrons are localized and form a Hund's rule ground state. The application of plain LDA calculations to 4*f* electron systems encounters problems in most cases, because of the correlated nature of electrons in the *f* shell. To better account for strong on-site electron correlations the LSDA + *U* approach should be used, in which a model Hamiltonian explicitly including the on-site Coulomb interaction, *U*, for localized states is combined with the standard band structure calculation Hamiltonian for extended states. The LSDA + *U* method provides a rather good description of the electronic structure and the XMCD properties of some lanthanide compounds.

Actinide compounds occupy an intermediate position between itinerant 3*d* and localized 4*f* systems, and one of the fundamental questions concerning the actinide materials is whether their *f* states are localized or itinerant. This question is most frequently answered by comparison

between experimental spectroscopies and the different theoretical descriptions. X-ray absorption spectroscopy, photoelectrons spectroscopy and bremsstrahlung isochromat spectroscopy supply direct information about the energy states (both occupied and unoccupied) around the Fermi energy, and can provide a means of discrimination between the two theoretical limits. The dual character of $5f$ electrons alongside with the presence of strong SO coupling make the determination of the electronic structure of uranium compounds a challenging task because in many of them the width of $5f$ bands, their spin-orbit splitting, and the on-site Coulomb repulsion in the partially filled $5f$ shell are of the same order of magnitude and should be taken into account on the same footing.

There are some features in common for all the uranium compounds investigated up to now. First, the dichroism at the M_4 edge is much larger, sometimes of one order of magnitude, than at the M_5 one. Second, the dichroism at the M_4 edge has a single negative peak that has no distinct structure, on the other hand, two peaks, a positive and a negative one, are observed at the M_5 edge. The peculiarities of the XMCD spectra can be understood qualitatively considering the partial density of states and the electric dipole selection rules.

The overall shapes of the calculated and experimental uranium $M_{4,5}$ XMCD spectra correspond well to each other. The major discrepancy between the calculated and experimental XMCD spectra is the size of the M_4 XMCD peak. The LSDA theory produces usually much smaller intensity for the XMCD spectrum at the M_4 edge in comparison with the experiment and simultaneously gives inappropriate dichroic signal strength at the M_5 edge. It fails to produce a correct intensity of dichroic signal at the M_4 edge even in UFe_2 which is widely believed to have itinerant $5f$ electrons. As the integrated XMCD signal is proportional to the orbital moment this discrepancy could be related rather to an underestimation of the orbital moment by LSDA-based computational methods rather than to a failure in the description of the energy band structure of the itinerant $5f$ systems. The LSDA + U approximation gives much better agreement in the shape and intensity of the XMCD spectra both at the M_4 and M_5 edges in uranium compounds.

Concerning the best description of line shape and intensity of the XMCD spectra, the investigated metallic uranium compounds fall into two groups according to the type of LSDA + U method used. The LSDA + U(OP) approximation ($U_{\text{eff}} = 0$) better describes the XMCD spectra in UFe_2, UXAl (X = Co, Rh, and Pt), UPd_2Al_3, and UNi_2Al_3 compounds. But the XMCD spectra of UPt3, URu_2Si_2, and UBe_{13} are better described by the LSDA + U method with U = 2.0 eV and J = 0.5 eV. It might be concluded to some extent that the last three compounds have a larger degree of localization than the compounds from the first group.

1. C. Giorgetti, S. Pizzini, E. Dartige, A. Fontaine, F. Baudelet, C. Brouder, P. Bauer, G. Krill, S. Miraglia, D. Fruchart, and J.P. Kappler, *Phys. Rev*. **B48**, 12732 (1993).
2. S. Suga and S. Imada, *J. Electron. Spectrosc. Relat. Phenom*. **78**, 231 (1996).
3. L.M. Garcia, S. Pizzini, J.P. Rueff, J. Galera, A. Fontaine, J.P. Kappler, G. Krill, and J. Goedkoop, *J. Appl. Phys.* **79**, 6497 (1996).
4. M. Finazzi, F.M.F. de Groot, A.M. Dias, B. Kierren, F. Bertran, P. Sainctavit, J.P. Kappler, O. Schulte, W. Felsch, and G. Krill, *Phys. Rev. Lett*. **75**, 4654 (1995).
5. J.P. Schille, F. Bertran, M. Finazzi, C. Brouder, J.P. Kappler, and G. Krill, *Phys. Rev*. **B50**, 2985 (1994).
6. J. Chaboy, H. Maruama, L.M. Garcia, J. Bartolome, K. Kobayashi, N. Kawamura, A. Marcelli, and L. Bozukov, *Phys. Rev*. **B54**, R15637 (1996).
7. J.P. Raeff, R.M. Galera, C. Giorgetti, E. Dartige, C. Brouder, and M. Alouani, *Phys. Rev*. **B58**, 12271 (1998).
8. I. Yamamoto, S.N.T. Nakamura, T. Fujikawa, and S. Nanao, *J. Electron. Spectrosc. Relat. Phenom.* **125**, 89 (2002).
9. R.M. Galera and A. Rogalev, *J. Appl. Phys*. **85**, 4889 (1999).
10. F. Bartolome, J.M. Tonnerre, L. Seve, D. Raoux, J.E. Lorenzo, J. Chaboy, L.M. Garcia, J. Bartolome, M. Krisch, A. Rogalev, R. Serimaa, G.C. Kao, G. Cibin, and A. Marcelli, *J. Appl. Phys*. **83**, 7091 (1998).
11. H. Wende, Z. Li, A. Scherz, G. Ceballos, K. Babeerschke, A. Ankudinov, J.J. Rehr, F. Wilhelm, A. Rogalev, D.L. Schlagel, and T.A. Lograsso, *J. Appl. Phys.* **91**, 7361 (2002).
12. A.R.B. de Castro, G.B. Fraguas, P.T. Fonseca, R.N. Suave, S. Gama, A.A. Coelho, and L.A. Santos, *J. Electron. Spectrosc. Relat. Phenom*. **101**–**103**, 725 (1999).
13. J. Chaboy, L.M. Garcia, F. Bartolome, H. Maruyama, S. Uemura, N. Kawamura, and A.S. Markosayan, *J. Appl. Phys*. **88**, 336 (2000).
14. W. Kossel, *Z. Physik* **1**, 119 (1920).
15. C. Bonnelle, R.C. Karnatak, and J. Sugar, *Phys. Rev*. **A9**, 1920 (1967).
16. V.F. Demekhin, *Fiz. Tverd. Tela (Leningrad)* **16**, 1020 (1974) [*Sov. Phys.-Solid State* **16**, 659 (1974)].
17. J. Sugar, *Phys. Rev*. **A6**, 1764 (1972).
18. J. Sugar, *Phys. Rev.* **B5**, 1785 (1972).
19. C. Bonnelle, R.C. Karnatak, and N. Spector, *J. Phys.* **B10**, 795 (1977).
20. B.T. Thole, G. van der Laan, J.C. Fuggle, G.A. Sawatzky, R.C. Karnatak, and J.-M. Esteva, *Phys. Rev*. **B32**, 5107 (1985).
21. J.B. Goedkoop, B.T. Thole, G. van der Laan, G.A. Sawatzky, F.M.F. de Groot, and J.C. Fuggle, *Phys. Rev*. **B37**, 2086 (1988).
22. G. van der Laan and B.T. Thole, *Phys. Rev*. **B42**, 6670 (1990).
23. S. Imada and T. Jo, *J. Phys. Soc. Jpn*. **59**, 3358 (1990).
24. Z. Hu, K. Starke, G. van der Laan, E. Navas, A. Bauer, E. Weschke, C. Schüssler-Langeheime, E. Arenholz, A. Mühlig, G. Kaindl, J.B. Goodkoop, and N.B. Brookes, *Phys. Rev*. **B59**, 9737 (1999).

25. G. van der Laan, E. Arenholz, Z. Hu, E. Weschke, C. Schüssler-Langeheime, E. Navas, A. Mühlig, G. Kaindl, J.B. Goodkoop, and N.B. Brookes, *Phys. Rev*. **B59**, 8835 (1999).
26. K. Starke, E. Navas, E. Arenholz, Z. Hu, L. Baumgarten, G. van der Laan, C.T. Chen, and G. Kaindl, *Phys. Rev.* **B55**, 2672 (1997).
27. B.N. Harmon and V.N. Antonov, *J. Appl. Phys*. **93**, 4678 (2003).
28. P. Wachter and E. Kaldis, *Solid State Commun*. **34**, 241 (1980).
29. P. Wachter, in: *Handbook of the Physics and Chemistry of Rare Earths*, K.A. Gschneidner, L. Eyring, and S. Hüfner (eds.), North-Holland, Amsterdam (1994), Vol. 19, p. 177.
30. D.X. Li, Y. Haga, H. Shida, T. Suzuki, Y.S. Kwon, and G. Kido, *J. Phys.: Condens. Matter* **9**, 10777 (1997).
31. A. Hasegawa and A. Yanase, *J. Phys. Soc. Jpn*. **42**, 492 (1977).
32. A.G. Petukhov, W.R.L. Lambrecht, and B. Segall, *Phys. Rev.* **B53**, 4324 (1996).
33. W.R.L. Lambrecht, *Phys. Rev*. **B62**, 13538 (2000).
34. S.A. Wolf, D.D. Awschalom, R.A. Buhrman, J.M. Daughton, S. von Molnar, M.L. Roukes, A.Y. Chtchelkanova, and D.M. Treger, *Science* **294**, 1488 (2001).
35. F. Leuenberger, A. Parge, W. Felsch, K. Fauth, and M. Hessler, *Phys. Rev*. **B72**, 014427 (2005).
36. V. Antonov, B. Harmon, A. Yaresko, and A. Shpak, *Phys. Rev*. **B76**,184422 (2007).
37. V.N. Antonov, B.N. Harmon, and A.N. Yaresko, *Phys. Rev*. **B63**, 205112 (2001).
38. V.N. Antonov, B.N. Harmon, and A.N. Yaresko, *Phys. Rev*. **B66**, 165208 (2002).
39. W.E. Picket, A.J. Freeman, and D.D. Koelling, *Phys. Rev*. **B22**, 2695 (1980).
40. J. Lang, Y. Baer, and P. Cox, *J. Phys.* **F11**, 121 (1981).
41. Y. Baer and W.D. Schneider, in: *Handbook of the Physics and Chemistry of Rare Earths*, K.A. Gschneidner, L. Eyring, and S. Hüfner (eds.), North-Holland, Amsterdam (1987), Vol. 10, p. 1.
42. F. Leuenberger, A. Parge, W. Felsch, F. Baudelet, C. Giorgetti, E. Dartyge, and F. Wilhelm, *Phys. Rev*. **B73**, 214430 (2006).
43. V. Antonov, B. Harmon, and A. Yaresko, *Electronic structure and magneto-optical properties of solids*, Kluwer Academic Publishers, Dordrecht, Boston, London (2004).
44. A. Rogalev, J. Goulon, and C. Brouder, *J. Phys. Condens. Matter* **11**, 1115 (1999).
45. P.G. Steeneken, *Ph.D. thesis,* University of Groningen, Groningen (2002).
46. G. Schütz, W. Wagner, W. Wilhelm, P. Kienle, R. Zeller, R. Frahm, and G. Materlik, *Phys. Rev. Lett*. **58**, 737 (1987).
47. C.M. Aerts, P. Strange, M. Horne, W.M. Temmerman, Z. Szotek, and A. Svane, *Phys. Rev*. **B69**, 045115 (2004).
48. P. Santini, R. Lemanski, and P. Erdoes, *Adv. Phys*. **48**, 537 (1999).
49. J.-M. Fournier and R. Troch, in: *Handbook on the Physics and Chemistry of the Actinides*, A.J. Freeman and G.H. Lander (eds.), North-Holland, Amsterdam (1985), Vol. 2, p. 29.
50. H.R. Ott and Z. Fisk, in: *Handbook on the Physics and Chemistry of the Actinides*, A.J. Freeman and G.H. Lander (eds.), North-Holland, Amsterdam (1987), Vol. 5.
51. V. Sechovsky and L. Havela, in: *Intermetallic Compounds of Actinides. Ferromagnetic Materials*, E.P. Wohlfarth and K.H.J. Buschow (eds.), Elsvier Amsterdam (1998), Vol. 4.
52. T. Endstra, S.A.M. Mentink, G.J. Nieuwenhuys, and J.A. Mydosh, in: *Magnetic Properties of Uranium Based 1-2-2 Intermetallics. Selected Topics in Magnetism*, L.C. Gupta and M.S. Multani (eds.), World Scienti, Singapore (1992).
53. M.R. Norman and D.D. Koelling, in: *Electronic Structure, Fermi Surfaces and Superconductivity in f Electron Metals. Handbook on the Physics and Chemistry of Rare Earths*, G.H.L.K.A. Gschneidner Jr., L. Eyring, and G.R. Choppin (eds.), Elsevier, Amsterdam (1993), Vol. 17.
54. J.M. Fournier and E. Gratz, in: *Transport Properties of Rare Earth and Actinide Intermetallics. Handbook on the Physics and Chemistry of Rare Earths*, G.H.L.K.A. Gschneidner Jr., L. Eyring, and G.R. Choppin (eds.), Elsevier, Amsterdam (1993), Vol. 17.
55. W. Potzel, G.M. Kalvius, and J. Gal, in: *Moessbauer Studies on Electronic Structure of Intermetallic Compounds. Handbook on the Physics and Chemistry of Rare Earths*, G.H.L.K.A. Gschneidner Jr., L. Eyring and G.R. Choppin (eds.), Elsevier, Amsterdam (1993), Vol. 17.
56. P. Fulde, J. Keller, and G. Zwicknagl, in: *Solid State Physics*, H. Ehrenreich and D. Turnbull (eds.), Academic Press, San Diego, CA (1988), Vol. 17.
57. A. Amato, *Rev. Mod. Phys*. **69**, 1119 (1997).
58. M.B. Maple, *J. Alloys Comp*. **303**–**304**, 1 (2000).
59. R. Joynt and L. Taillefer, *Rev. Mod. Phys*. **74**, 235 (2002).
60. M. Sigrist and K. Ueda, *Rev. Mod. Phys*. **63**, 239 (1991).
61. S.P. Collins, D. Laundy, C.C. Tang, and G. van der Laan, *J. Phys.: Condens. Matter* **7**, 9325 (1995).
62. N. Kernavanois, P.D. de Reotier, A. Yaouanc, J.P. Sanchez, V. Honkimäki, T. Tschentscher, J. McCarthy, and O. Vogt, *J. Phys.: Condens. Matter* **13**, 9677 (2001).
63. P.D. de Reotier, J.P. Sanchez, A. Yaouanc, M. Finazzi, P. Sainctavit, G. Krill, J.P. Kappler, J. Goedkoop, J. Goulon, C. Goulon-Ginet, A. Rogalev, and O. Vogt, *J. Phys.: Condens. Matter* **9**, 3291 (1997).
64. A. Bombardi, N. Kernovanois, P.D. de Reotier, G.H. Lander, J.P. Sanchez, A. Yaouanc, P. Burlet, E. Lelievre-Berna, A. Rogalev, O. Vogt, and K. Mattenberger, *Eur. Phys. J.* **B21**, 547 (2001).
65. P.D. de Reotier, A. Yaouanc, G. van der Laan, N. Kernavanois, J.P. Sanchez, J.L. Smith, A. Hiess, A. Huxley, and A. Rogalev, *Phys. Rev*. **B60**, 10606 (1999).
66. M. Finazzi, P. Sainctavit, A.M. Dias, J.P. Kappler, G. Krill, J.P. Sanchez, P.D. de Reotier, A. Yaouanc, A. Rogalev, and J. Goulon, *Phys. Rev*. **B55**, 3010 (1997).
67. P.D. de Reotier, J.P. Sanches, and A. Yaouanc, *J. Alloys Comp*. **271**–**273**, 414 (1998).
68. N. Kernavanois, J.X. Boucherle, P.D. de Reotier, F. Givord, E. Lelievre-Berna, E. Ressouche, A. Rogalev, J.P. Sanchez, N. Sato, and A. Yaouanc, *J. Phys.: Condens. Matter* **12**, 7857 (2000).

69. A. Yaouanc, P.D. de Reotier, G. van der Laan, A. Hiess, J. Goulon, C. Neumann, P. Lejay, and N. Sato, *Phys. Rev*. **B58**, 8793 (1998).
70. W. Grange, M. Finazzi, J.P. Kappler, A. Dellobe, G. Krill, P. Sainctavit, J.P. Sanchez, A. Rogalev, and J. Goulon, *J. Alloys Comp.* **275**–**277**, 583 (1998).
71. M. Kucera, J. Kunes, A. Kolomiets, M. Divis, A.V. Andreev, V. Sechovsky, J.P. Kappler, and A. Rogalev, *Phys. Rev*. **B66**, 144405 (2002).
72. V.N. Antonov, B.N. Harmon, and A.N. Yaresko, *Phys. Rev*. **B68**, 214425 (2003).
73. A.N. Yaresko, V.N. Antonov, and P. Fulde, *Phys. Rev*. **B67**, 155103 (2003).
74. B.T. Thole, P. Carra, F. Sette, and G. van der Laan, *Phys. Rev. Lett*. **68**, 1943 (1992).
75. J.C. Fuggle and J.E. Inglesfield, *Unoccupied Electronic States. Topics in Applied Physics*, Springer, New York (1992), Vol. 69.
76. V. Sechovsky and L. Havela, in: *Handbook of Magnetic Materials*, K.H.J. Buschow (eds.), Elsevier, Amsterdam (1998), Vol. 11, p. 1.
77. N.V. Mushnikov, T. Goto, K. Kamishima, H. Yamada, A.V. Andreev, Y. Shiokawa, A. Iwao, and V. Sechovsky, *Phys. Rev*. **B59**, 6877 (1999).
78. M. Wulff, J.M. Fournier, A. Delapalme, B. Gillon, V. Sechovsky, L. Havela, and A.V. Andreev, *Physica* **B163**, 331 (1990).
79. J.A. Paixäo, G.H. Lander, P.J. Brown, H. Nakotte, F.R. de Boer, and E. Brück, *J. Phys.: Condens. Matter* **4**, 829 (1992).
80. A. Hiess, L. Havela, K. Prokevs, R.S. Eccleston, and G.H. Lander, *Physica* **B230**–**232**, 89 (1997).
81. A.V. Andreev, Y. Shiokawa, M. Tomida, Y. Homma, V. Sechovsky, and N.V. Mushnikov, *J. Phys. Soc. Jpn*. **68**, 1999 (1999).
82. K.A. McEwen, U. Steigenberger, and J.L. Martinez, *Physica* **B186**–**188**, 670 (1993).
83. P.M. Oppeneer, A.Y. Perlov, V.N. Antonov, A.N. Yaresko, T. Kraft, and M.S. Brooks, *J. Alloys Comp*. **271**–**273**, 831 (1998).
84. T. Gascher, M.S.S. Brooks, and B. Johansson, *J. Phys.: Condens. Matter* **7**, 9511 (1995).
85. J. Kunes, P. Novak, M. Divis, and P.M. Oppeneer, *Phys. Rev*. **B63**, 205111 (2001).
86. V.N. Antonov, B.N. Harmon, O. Andryushchenko, L. Bekenev, and A.N. Yaresko, *Phys. Rev*. **B68**, 214425 (2003).
87. G.H. Lande, M.S.S. Brooks, and B. Johansson, *Phys. Rev*. **B43**, 13672 (1991).
88. P. Carra, B.T. Thole, M. Altarelli, and X. Wang, *Phys. Rev. Lett*. **70**, 694 (1993).
89. F.K. Richtmyer, S.W. Barnes, and E. Ramberg, *Phys. Rev.* **46**, 843 (1934).
90. D.L. Tillwick and P. de V. du Plessis, *J. Magn. Magn. Mater.* **3**, 329 (1976).
91. G. Busch, O. Vogt, A. Delpalme, and G.H. Lander, *J. Phys.* **C12**, 1391 (1979).
92. G.H. Lander, M.S.S. Brooks, B. Lebech, P.J. Brown, O. Vogt, and K. Mattenberger, *J. Appl. Phys*. **69**, 4803 (1991).
93. M.S.S. Brooks and P.J. Kelly, *Phys. Rev. Lett*. **51**, 1708 (1983).
94. G.H. Lander, *Physica* **B186–188**, 664 (1993).
95. M.S.S. Brooks, *Physica* **B130**, 6 (1985).
96. F.A. Wedgwood, *J. Phys*. **C5**, 2427 (1972).
97. B. Reihl, *J. Less-Common Met*. **128**, 331 (1987).
98. J. Schoenes, B. Frick, and O. Vogt, *Phys. Rev*. **B30**, 6578 (1984).
99. J. Schoenes, B. Frick, and O. Vogt, *Phys. Rev*. **B30**, 6578 (1984).
100. C.Y. Huang, R.J. Laskowski, C.E. Olsen, and J.L. Smith, *J. Phys*. **C40**, 26 (1979).
101. E.F. Westrum, R.R. Walters, H.E. Flotow, and D.W. Osborne, *J. Chem. Phys*. **48**, 155 (1968).
102. P. Erdoes and J. Robinson, *The Physics of Actinide Compounds*, Plenum Press, New York, London (1983).
103. J. Neuenschwander, O. Vogt, E. Vogt, and P. Wachter, *Physica* **B144**, 66 (1986).
104. H. Bilz, G. Guentherodt, W. Kleppmann, and W. Kress, *Phys. Rev. Lett*. **43**, 1998 (1979).
105. A.L. Cornelius, J.S. Schilling, O. Vogt, K. Mattenberger, and U. Benedict, *J. Magn. Magn. Mater*. **161**, 169 (1996).
106. O.G. Sheng and B.R. Cooper, *J. Magn. Magn. Mater*. **164**, 335 (1996).
107. S.V. Halilov and E.T. Kulatov, *J. Phys.: Condens. Matter* **3**, 6363 (1991).
108. T. Gasche, *Ph.D. thesis*, Uppsala (1993).
109. B.R. Cooper, Q.G. Sheng, S.P. Lim, C. Sanchez-Castro, N. Kioussis, and J.M. Wills, *J. Magn. Magn. Mater*. **108**, 10 (1992).
110. T. Kraft, P.M. Oppeneer, V.N. Antonov, and H. Eschrig, *Phys. Rev*. **B52**, 3561 (1995).
111. J. Trygg, J.M. Wills, and M.S.S. Brooks, *Phys. Rev*. **B52**, 2496 (1995).
112. P.M. Oppeneer, V.N. Antonov, A.Y. Perlov, A.N. Yaresko, T. Kraft, and H. Eschrig, *Physica* **B230–232**, 544 (1997).
113. H. Yamagami, *J. Phys. Soc. Jpn*. **67**, 3176 (1999).
114. T. Shishidou, T. Oguchi, and T. Jo, *Phys. Rev*. **B59**, 6813 (1999).
115. T. Shishidou and T. Oguchi, *Phys. Rev*. **B62**, 11747 (2000).
116. V.N. Antonov, B.N. Harmon, O. Andryushchenko, L. Bekenev, and A.N. Yaresko, *Fiz. Nizk. Temp*. **30**, 411 (2004) [*Low Temp. Phys*. **30**, 305 (2004)].
117. L. Severin, M.S.S. Brooks, and B. Johansson, *Phys. Rev. Lett.* **71**, 3214 (1993).
118. H. Sakurai, H. Hashimoto, A. Ochiai, T. Suzuki, M. Ito, and F. Itoh, *J. Phys.: Condens. Matter* **7**, L599 (1995).
119. M.S.S. Brooks and B. Johansson, in: Handbook of Magnetic Materials, K.H.J. Buschow (eds.), North-Holland, Amsterdam (1993), Vol. 7, p. 139.
120. O. Eriksson, M.S.S. Brooks, and B. Johansson, *Phys. Rev*. **B41**, 7311 (1990).
121. A. Mavromaras, L. Sandratskii, and J. Kübler, *Solid State Commun*. **106**, 115 (1998).
122. I.V. Solovyev, A.I. Liechtenstein, and K. Terakura, *Phys. Rev. Lett.* **80**, 5758 (1998).
123. M.S.S. Brooks, T. Gasche, and B. Johansson, *J. Phys. Chem. Solids* **56**, 1491 (1995).
124. B. Reihl, N. Martensson, and O. Vogt, *J. Appl. Phys*. **53**, 2008 (1982).

125. G.R. Stewart, Z. Fisk, J.O. Willis, and J.L. Smith, *Phys. Rev. Lett*. **52**, 679 (1984).
126. G. Stewart, *Rev. Mod. Phys*. **56**, 755 (1984).
127. R. Albers, A.M. Boring, and N.E. Christensen, *Phys. Rev*. **B33**, 8116 (1986).
128. M.R. Norman, R.C. Albers, A.M. Boring, and N.E. Christensen, *Solid State Commun*. **68**, 245 (1988).
129. N. Kimura, R. Settai, Y. Onuki, H. Toshima, E. Yamamoto, K. Maezawa, H. Aoki, and H. Harima, *J. Phys. Soc. Jpn*. **64**, 3883 (1995).
130. S.R. Julian, G.J. Teunissen, N. Dorion-Leyraund, A.D. Huxley, M.P. Ray, M.R. Norman, J. Floquet, and G.G. Lonzarich, *The Fermi Surface of* UPt_3, University of Cambridge, Cambridge (2000).
131. G. Zwicknagl, A.N. Yaresko, and P. Fulde, *Phys. Rev*. **B65**, R081103 (2002).
132. L. Taillefer and G.G. Lonzarich, *Phys. Rev. Lett.* **60**, 1570 (1988).
133. L. Taillefer, R. Newbury, G.G. Lonzarich, Z. Fisk, and J.L. Smith, *J. Magn. Magn. Mater.* **63–64**, 372 (1987).
134. N. Kimura, T. Komatsubara, D. Aoki, Y. Onuki, Y. Haga, E. Yamamoto, H. Aoki, and H. Harima, *J. Phys. Soc. Jpn*. **67**, 2185 (1998).
135. R.H. Heffner, D.W. Cooke, A.L. Giorgi, R.L. Hutson, M.E. Schillaci, H.D. Rempp, J.L. Smith, J.O. Willis, D.E. MacLaughlin, C. Boekema, R.L. Lichti, J. Oostens, and A.B. Denison, *Phys. Rev.* **B39**, 11345 (1989).
136. G. Aeppli, E. Bucher, A.I. Goldman, G. Shirane, C. Broholm, and J.K. Kjems, *J. Magn. Magn. Mater*. **76–77**, 385 (1988).
137. S.M. Hayden, L. Taillefer, C. Vettier, and J. Flouquet, *Phys. Rev.* **B46**, 8675 (1992).
138. B. Lussier, B. Ellman, and L. Taillefer, *Phys. Rev.* **B53**, 5145 (1996).
139. E.D. Isaacs, P. Zschack, C.L. Broholm, C. Burns, G. Aeppli, A.P. Ramirez, T.T.M. Palstra, R.W. Erwin, N. Stucheli1, and E. Bucher, *Phys. Rev. Lett.* **75**, 1178 (1995).
140. A.N. Yaresko, V.N. Antonov, and B.N. Harmon, *Phys. Rev.* **B68**, 214426 (2003).
141. J.W. Allen, J.D. Denlinger, Y.X. Zhang, G.-H. Gweon, S.-H. Yang, S.-J. Oh, E.-J. Cho, W.P. Ellis, D.A. Gajewski, R. Chau, and M.B. Maple, *Physica* **B281–282**, 725 (2000).
142. T. Ito, H. Kumigashira, S. Souma, T. Takahashi, Y. Tokiwa, Y. Haga, and Y. Onuki, *Physica* **B312–313**, 653 (2002).
143. Y. Tokiwa, K. Sugiyama, T. Takeuchi, M. Nakashima, R. Settai, Y. Inada, Y. Haga, E. Yamamoto, K. Kindo, H. Harima, and Y. Onuki, *J. Phys. Soc. Jpn*. **70**, 1731 (2001).
144. W.J.L. Buyers, A.F. Murray, T.M. Holden, and E.C. Svensson, *Physica* **B+C102**, 291 (1980).
145. H. Harima, *J. Magn. Magn. Mater*. **226–230**, 83 (2001).
146. T.T.M. Palstra, A.A. Menovsky, J. van der Berg, J. Dirkmaat, P.H. Kes, G.J. Nieuwenhuys, and J.A. Mydosh, *Phys. Rev. Lett*. **55**, 2727 (1985).
147. W. Schlabitz, J. Baumann, B. Pollit, U. Rauchschwalbe, H.M. Mayer, U. Ahlheim, and C.D. Bredl, *Z. Physik* **62**, 171 (1986).
148. A. de Visser, F.E. Kayzel, A.A. Menovsky, J.J.M. Franse, J. van der Berg, and G.J. Nieuwenhuys, *Phys. Rev*. **B34**, 8168 (1986).
149. C. Broholm, J.K. Kjems, W.J.L. Buyers, P. Matthews, T.T.M. Palstra, A.A. Menovsky, and J.A. Mydosh, *Phys. Rev. Lett.* **58**, 1467 (1987).
150. C Broholm, H. Lin, P.T. Matthews, T.E. Mason, W.J.L. Buyers, M.F. Collins, A.A. Menovsky, J.A. Mydosh, and J.K. Kjems, *Phys. Rev.* **B43**, 12809 (1991).
151. Y. Kohori, K. Matsuda, and T. Kohara, *J. Phys. Soc. Jpn*. **65**, 1083 (1996).
152. S.A.M. Mentink, T.E. Mason, S. Suüllow, G.J. Nieuwenhuys, A.A. Menovsky, and J.A.A.J. Peerenboom, *Phys. Rev*. **B53**, R6014 (1996).
153. K. Hasselbach, J.R. Kirtley, and P. Lejay, *Phys. Rev*. **B46**, 5826 (1992).
154. A. de Visser, F.R. de Boer, A.A. Menovsky, and J.J.M. Franse, *Solid State Commun.* **64**, 527 (1987).
155. K. Sugiyama, H. Fuke, K. Kindo, K. Shimohata, A.A. Menovsky, J.A. Mydosh, and M. Date, *J. Phys. Soc. Jpn*. **59**, 3331 (1990).
156. K. Bakker, A. de Visser, A.A. Menovsky, and J.J.M. Franse, *Physica* **B186–188**, 720 (1993).
157. M.R. Norman, T. Oguchi, and A.J. Freeman, *Phys. Rev*. **B38**, 11193 (1988).
158. L.M. Sandratskii and J. Kübler, *Phys. Rev*. **B50**, 9258 (1994).
159. A. Continenza and P. Johansson, *J. Magn. Magn. Mater*. **140–144**, 1401 (1995).
160. H. Yamagami and N. Hamada, Physica **B284–288**, 1295 (2000).
161. H. Ohkuni, T. Ishida, Y. Inada, Y. Haga, E. Yamamoto, Y. Onuki, and S. Takahashi, *J. Phys. Soc. Jpn.* **66**, 945 (1997).
162. T. Ito, H. Kumigashira, T. Takahashi, Y. Haga, E. Yamamoto, T. Honma, H. Ohkuni, and Y. Onuki, *Physica* **B281–282**, 727 (2000).
163. C. Geibel, C. Schank, S. Thies, H. Kitazawa, C.D. Bredl, A. Booehm, M. Rau, A. Grauel, R. Caspary, R. Helfrich, U. Ahlheim, G. Weber, and F. Steglich, *Z. Physik* **84**, 1 (1991).
164. C. Geibel, S. Thies, D. Kaczorowski, A. Mehner, A. Grauel, B. Seidel, U. Ahlheim, R. Helfrich, K. Petersen, C.D. Bredl, and F. Steglich, *Z. Physik* **83**, 305 (1991).
165. A. Krimmel, P. Fischer, B. Roessli, H. Maletta, C. Geibel, C. Schank, A. Grauel, A. Loidl, and F. Steglich, *Z. Physik* **86**, 161 (1992).
166. J. Sticht and J. Kübler, *Z. Physik* **B87**, 299 (1992).
167. L.M. Sandratskii, J. Kübler, P. Zahn, and I. Mertig, *Phys. Rev*. **B50**, 15834 (1994).
168. K. Knöpfle, A. Mavromaras, L.M. Sandratskii, and J. Kübler, *J. Phys.: Condens. Matter* **8**, 901 (1996).
169. S. Fujimori, Y. Saito, M. Seki, K. Tamura, M. Mizuta, K. Yamaki, K. Sato, T. Okane, A. Tanaka, N. Sato, T. Komatsubara, Y. Tezuka, S. Shin, S. Suzuki, and S. Sato, *J. Electron. Spectrosc. Relat. Phenom*. **101–103**, 439 (1999).
170. T. Rjima, S.Sato, S. Suzuki, S. Fujimori, M. Yamada, N. Sato, Y. Onuki, T. Komatsubara, Y. Tezuka, Shin, and T. Ishii, *J. Electron. Spectrosc. Relat. Phenom.* **78**, 147 (1996).
171. A. Amato, C. Geibel, F.N. Gygax, R.H. Hefner, E. Knetsch, D.E. MacLaughlin, C. Schank, A. Schenck, F. Steglich, and M. Weber, *Z. Physik* **86**, 159 (1992).

172. J.G. Lussier, M. Mao, A.A. Schröder, J. Garret, B.D. Gaulin, S.M. Shapiro, and W.J.L. Buyers, *Phys. Rev.* **B56**, 11749 (1997).
173. H.R. Ott, H. Rudigier, Z. Fisk, and J.L. Smith, *Phys. Rev. Lett*. **50**, 1595 (1983).
174. D.L. Cox and A. Zawadowski, *Adv. Phys*. **47**, 599 (1998).
175. M.W. McElfresh, M.B. Maple, J.O. Willis, D. Schiferl, J.L. Smith, Z. Fisk, and D.L. Cox, *Phys. Rev*. **B48**, 10395 (1993).
176. E. Miranda, V. Dobrosavljevic, and G. Kottliar, *Phys. Rev. Lett.* **78**, 290 (1997).
177. D.L. Cox, *Phys. Rev. Lett*. **59**, 1240 (1987).
178. F.B. Anders, M. Jarell, and D.L. Cox, *Phys. Rev. Lett*. **78**, 2000 (1997).
179. K. Takegahara, H. Harima, and T. Kasuya, *J. Phys*. **F16**, 1691 (1986).
180. M.R. Norman, W.E. Picket, H. Krakauer, and C.S. Wang, *Phys. Rev*. **B36**, 4058 (1987).
181. K. Takegahara and H. Harima, *Physica* **B281–282**, 764 (2000).
182. T. Maehira, A. Higashia, M. Higuchi, H. Yasuhara, and A. Hasegawa, *Physica* **B312–313**, 103 (2002).
183. V.I. Anisimov, J. Zaanen, and O.K. Andersen, *Phys. Rev*. **B44**, 943 (1991).
184. E. Wuilloud, Y. Baer, H.R. Ott, Z. Fisk, and J.L. Smith, *Phys. Rev*. **B29**, 5228 (1984).
185. V.N. Antonov, B.N. Harmon, and A.N. Yaresko, *Phys. Rev.* **B66**, 165209 (2002).
186. V.L. Ginzburg, *Sov. Phys. JETP* **4**, 153 (1957).
187. N. Aso, G. Motoyama, Y. Uwatoko, S. Ban, S. Nakamura, T. Nishioka, Y. Homma, Y. Shiokawa, K. Hirota, and N.K. Sato, *Phys. Rev*. **B73**, 054512 (2006).
188. S. Saxena, P. Agarwal, K. Ahilan, F. Grosche, R. Haselwimmer, M. Steiner, E. Pugh, I. Walker, S. Julian, P. Monthoux, G. Lonzarich, A. Huxley, I. Sheikin, D. Braithwaite, and J. Flouquet, *Nature* **406**, 587 (2000).
189. A. Huxley, I. Sheikin, E. Ressouche, N. Kernavanois, D. Braithwaite, R. Calemczuk, and J. Flouquet, *Phys. Rev.* **B63**, 144519 (2001).
190. A.N. Yaresko, P.D. de Ráotier, A. Yaouanc, N. Kernavanois, J.-P. Sanchez, A.A. Menovsky, and V.N. Antonov, *J. Phys.: Condens. Matter* **17**, 2443 (2005).
191. T. Okane, J. Okamoto, K. Mamiya, S. Fujimori, Y. Takeda, Y. Saitoh, Y. Muramatsu, A. Fujimori, Y. Haga, E. Yamamoto, A. Tanaka, T. Honda, Y. Inada, and Y. Nuki, *J. Phys. Soc. Jpn.* **75**, 024704 (2006).
192. Y. Inada, T. Honma, N. Kawamura, M. Suzuki, H. Miyagawa, E. Yamamoto, Y. Haga, T. Okane, S. Fujimori, and Y. Onuki, *Physica* **B359–361**, 1054 (2005).
193. V. Antonov, B. Harmon, and A. Yaresko, *J. Phys.: Condens. Matter* **19**, 186222 (2007).
194. G. van der Laan and B.T. Thole, *Phys. Rev*. **B53**, 14458 (1996).
195. H. Ebert, *Rep. Prog. Phys*. **59**, 1665 (1996).
196. V.N. Antonov, O. Jepsen, A.N. Yaresko, and A.P. Shpak, *J. Appl. Phys*. **100**, 043711 (2006).
197. H. Maruyama, M. Suzuki, N. Kawamura, M. Ito, E. Arakawa, J. Kokubun, K. Hirano, K. Horie, S. Uemura, K. Hagiwara, M. Mizumaki, S. Goto, H. Kitamura, K. Namikawa, and T. Ishikawa, *J. Synchrotron Rad*. **6**, 1133 (1999).
198. M. Usuda, J. Igarashi, and A. Kodama, *Phys. Rev.* **B69**, 224402 (2004).